

**FATIGUE CRACKING OF NEAR-EUTECTOID STEEL
IN CORROSIVE ENVIRONMENTS**

by

KHAIRY EL-HADI HASSAN

B.Sc., Alfateh University, Tripoli, Libya, 1986

**A THESIS SUBMITTED IN PARTIAL FULFILLMENT OF
THE REQUIREMENTS FOR THE DEGREE OF
MASTER OF APPLIED SCIENCE**

in

**THE FACULTY OF GRADUATE STUDIES
(Department of Metals and Materials Engineering)**

We accept this thesis as conforming

to the required standard

THE UNIVERSITY OF BRITISH COLUMBIA

December 1996

© Khairy El-hadi Hassan, 1996

In presenting this thesis in partial fulfilment of the requirements for an advanced degree at the University of British Columbia, I agree that the Library shall make it freely available for reference and study. I further agree that permission for extensive copying of this thesis for scholarly purposes may be granted by the head of my department or by his or her representatives. It is understood that copying or publication of this thesis for financial gain shall not be allowed without my written permission.

Department of *Metals and Materials Engineering*

The University of British Columbia
Vancouver, Canada

Date *December 18, 1996*

Abstract

The fatigue crack propagation behavior of near-eutectoid steel (AISI 1070) was investigated in both pearlitic and fully spheroidized microstructures. Experiments were conducted on single edge notched specimens. Constant amplitude sinusoidal loading was applied at high frequency (~ 97 Hz) with R ratio of 0.5. Testing conditions were primarily under plane strain and good mixing between the crack tip solution and bulk solution was maintained. Experiments were conducted at ambient temperature and surface crack growth was measured optically. Attention was directed towards the effects of environment, heat treatment and cathodic protection. Environments were: desiccated air, distilled water, 3.5% $NaCl$ solution, and buffered 3.5% $NaCl$ solution (pH=10.5). Experiments in the $NaCl$ solutions were conducted with and without cathodic protection.

The results indicate that crack propagation is slower in the fully spheroidized microstructure. Formation of corrosion products in the crack caused crack growth retardation. The minimum crack propagation rate was observed in the spheroidized microstructure in 3.5% $NaCl$ solution cathodically polarized to $-1.0 V_{SCE}$. Corrosion products induced a crack closure effect, and reduced the effective crack tip cyclic stress intensity factor (ΔK_{eff}) to a lower level.

Crack fractography was examined using scanning electron microscopy (SEM). Fatigue striations were not readily visible in stage-II fatigue crack propagation. The overload region (stage-III) showed crystallographic cleavage-like facets and river lines.

Table of contents

Abstract	ii
Table of contents	iii
List of Tables	vi
List of Figures	vii
List of symbols and abbreviations	xi
Acknowledgments	xvi
1 Introduction	1
2 Literature review	3
2.1 Corrosion fatigue cracking (CFC)	4
2.1.1 Characteristics of CFC	4
2.1.2 Variables affecting CFC	4
2.1.2.1 Mechanical variables	5
2.1.2.2 Metallurgical variables	5
2.1.2.3 Environmental variables	6
2.1.3 Fracture mechanics and corrosion fatigue	7
2.1.4 Corrosion fatigue failures	9
2.1.4.1 Crack initiation	9
2.1.4.2 Crack propagation	9
2.1.5 Corrosion fatigue endurance	13
2.1.6 Corrosion fatigue mechanisms	15
2.1.6.1 Hydrogen embrittlement	15
2.1.6.2 Anodic dissolution	18
2.1.7 Crack growth retardation effects	19
2.1.8 Prevention of CFC	20
2.1.8.1 Cathodic protection (CP).....	21
2.1.8.2 Corrosion inhibitors	22

2.1.8.3 pH control	22
2.1.8.4 Surface coating and plating	22
2.1.8.5 Corrosion-resistant materials.....	23
2.1.8.6 Reduction of stresses	24
2.2 The eutectoid steel	25
2.2.1 The eutectoid reaction	25
2.2.2 Pearlitic and spheroidized microstructures	27
2.2.3 Mechanical properties of eutectoid steel	28
2.2.4 Industrial applications of eutectoid steel	31
2.2.5 Corrosion of eutectoid steel	33
2.2.6 Stress corrosion cracking of eutectoid steel	35
2.2.7 Hydrogen embrittlement of eutectoid steel	36
2.2.8 Corrosion fatigue cracking of eutectoid steel	37
3 Objective	41
4 Experimental	42
4.1 Material	42
4.1.1 Chemical composition	42
4.1.2 Heat treatment	42
4.1.3 Metallography	43
4.2 Specimen design and preparation	43
4.2.1 Tensile specimens	43
4.2.2 Electrochemical test specimens	44
4.2.2 Fatigue specimens	45
4.3 Test environment selection	47
4.4 Test setup and procedures	48
4.4.1 Tensile and hardness testing	48
4.4.2 Potentiodynamic polarization tests	49
4.4.3 Fatigue testing	52
4.4.4 Fractographic study	56

5 Results	58
5.1 Material characterization	58
5.1.1 Microstructure	58
5.1.2 Mechanical properties	58
5.2 Electrochemical behavior	61
5.3 Fatigue crack propagation behavior	66
5.3.1 As received condition	66
5.3.2 Heat treated condition	73
5.4 SEM fractography	79
5.4.1 As received condition	79
5.4.2 Heat treated condition	80
6 Discussion	93
6.1 Stress state and plastic zone	93
6.2 General crack propagation characteristics	95
6.3 Corrosion fatigue cracking model	96
6.4 Corrosion fatigue crack propagation in the pearlitic microstructure	101
6.4.1 Effect of microstructure	101
6.4.2 Role of environment	102
6.4.3 Dissolution phenomena and cracking rates	103
6.5 Corrosion fatigue crack propagation in the spheroidized microstructure	107
6.5.1 Effect of microstructure	107
6.5.2 Role of environment	107
6.5.3 Effect of hydrogen	108
6.6 Industrial applications of the reported data	110
7 Summary and Conclusions	111
8 References	113

List of Tables

Table 4.1 Chemical Composition (wt %)	42
Table 4.2 Fatigue test environments and testing conditions	48
Table 4.3 Potentiodynamic anodic polarization test parameters	50
Table 5.1 Mechanical properties	61
Table 5.2 Freely corroding potentials at ~24°C	63
Table 5.3 Threshold stress intensities for fatigue tests (AR condition)	67
Table 5.4 Threshold stress intensities for fatigue tests (HT condition)	73

List of Figures

Figure 2.1 Schema showing interaction of cracking forms under static and cyclic loads [1].....	3
Figure 2.2 Characteristics of environmentally induced cracking forms [35].....	4
Figure 2.3 Loading modes [39].....	8
Figure 2.4 Initiation of cracks in persistent slip bands (PSB's) [39].....	10
Figure 2.5 Schematic illustration of variation of fatigue-crack-growth rate, da/dN , with alternating stress intensity, ΔK , in steels, showing regions of primary crack-growth mechanisms [56]	10
Figure 2.6 Schematic diagram illustrating the model for stage-I fatigue crack propagation based on restricted slip reversal. S1, S2, S3, S4 are slip planes on which reverse slip occurs [59].....	11
Figure 2.7 An idealization of plastic blunting and re-sharpening which leads to stage-II fatigue crack growth in fully-reversed fatigue. (a) zero load, (b) small tensile load, (c) peak tensile load, (d) onset of load reversal, (e) peak compressive load, and (f) small tensile load in the subsequent tensile cycle. Arrows indicate slip direction [42].....	12
Figure 2.8 Effect of various environments on the $S-N$ curve of steel [37].	14
Figure 2.9 Various processes involved in the hydrogen embrittlement of ferrous alloys [34].	17
Figure 2.10 Schematic illustration of the principal mechanisms of fatigue crack closure [63].	20
Figure 2.11 Pourbaix diagram for iron [35].....	21
Figure 2.12 The $Fe-C$ equilibrium diagram up to 6.67%C. Solid lines indicate $Fe-Fe_3C$ diagram; dashed lines indicate Fe-graphite diagram [54].....	26
Figure 2.13 (a) Various components of a typical cord/rope; (b) helix angle [30]	32
Figure 2.14 schematic depiction of stage-I crack parallel to cementite lamellae [21].....	38
Figure 4.1 Tensile test specimen	44
Figure 4.2 The electrochemical test specimens	45

Figure 4.3 Geometry of the single edge notched (SEN) specimen.....	46
Figure 4.4 The experimental setup for the electrochemical testing.....	51
Figure 4.5 The experimental setup of fatigue testing	54
Figure 5.1 Microstructure of the as received material (lamellar). (a) at X3000 mag., (b) at X5000 mag.	59
Figure 5.2 Microstructure of the heat-treated material (fully spheroidized). (a) at X2000 mag., (b) at X6000 mag.	60
Figure 5.3 Anodic potentiodynamic polarization behavior of AISI 1070 steel starting anodic scan from E_{corr}	62
Figure 5.4 Anodic potentiodynamic polarization behavior of AISI 1070 steel (deaerated solution)	64
Figure 5.5 Anodic potentiodynamic polarization behavior of AISI 1070 steel (aerated solution)	65
Figure 5.6 Fatigue crack growth behavior in pearlitic AISI 1070 steel.....	68
Figure 5.7 Fatigue crack growth behavior in pearlitic AISI 1070 steel in 3.5% NaCl and E_{corr}	69
Figure 5.8 Effect of cathodic polarization on fatigue crack growth behavior in pearlitic AISI 1070 steel at pH = 6.0	70
Figure 5.9 Effect of cathodic polarization on fatigue crack growth behavior in pearlitic AISI 1070 steel at pH = 10.5	71
Figure 5.10 Effect of environment and ΔK on the growth of fatigue cracks in pearlitic AISI 1070 steel	72
Figure 5.11 Effect of heat treatment (microstructure) on fatigue crack growth behavior in AISI 1070 steel	74
Figure 5.12 Fatigue crack growth behavior in spheroidized AISI 1070 steel.....	75
Figure 5.13 Effect of cathodic polarization on fatigue crack growth behavior in spheroidized AISI 1070 steel at pH = 6.0	76
Figure 5.14 Effect of environment and ΔK on fatigue crack growth behavior in spheroidized AISI 1070 steel.....	77

- Figure 5.15 Fatigue crack growth behavior in AISI 1070 steel in 3.5% NaCl polarized to $-1.0 V_{SCE}$ 78
- Figure 5.16 SEM fractographs showing fatigue cracking of pearlitic AISI 1070
 (a) Desiccated air, stage-I, $\Delta K \cong 4.5 \text{ MPa.m}^{1/2}$, $da/dN \cong 4.1 \times 10^{-7} \text{ mm/cycle}$
 (b) Desiccated air, stage-II, $\Delta K \cong 8.0 \text{ MPa.m}^{1/2}$, $da/dN \cong 8.3 \times 10^{-6} \text{ mm/cycle}$ 82
- Figure 5.17 SEM fractographs showing fatigue cracking of pearlitic AISI 1070
 (a) Desiccated air, stage-II, $\Delta K \cong 16 \text{ MPa.m}^{1/2}$, $da/dN \cong 1.0 \times 10^{-4} \text{ mm/cycle}$
 (b) Desiccated air, stage-III (overload), cleavage fracture 83
- Figure 5.18 SEM fractographs showing fatigue cracking of pearlitic AISI 1070
 (a) Distilled water, stage-I, $\Delta K \cong 4.2 \text{ MPa.m}^{1/2}$, $da/dN \cong 4.0 \times 10^{-8} \text{ mm/cycle}$
 (b) Distilled water, stage-II, $\Delta K \cong 8.2 \text{ MPa.m}^{1/2}$, $da/dN \cong 3.9 \times 10^{-6} \text{ mm/cycle}$ 84
- Figure 5.19 SEM fractographs showing fatigue cracking of pearlitic AISI 1070
 (a) 3.5% NaCl, E_{corr} , stage-I, before cleaning, $\Delta K \cong 2.3 \text{ MPa.m}^{1/2}$, $da/dN \cong 6.7 \times 10^{-8} \text{ mm/cycle}$
 (b) 3.5% NaCl, E_{corr} , stage-I, after cleaning, $\Delta K \cong 2.3 \text{ MPa.m}^{1/2}$, $da/dN \cong 6.7 \times 10^{-8} \text{ mm/cycle}$
 85
- Figure 5.20 SEM fractographs showing fatigue cracking of pearlitic AISI 1070
 (a) 3.5% NaCl, $E = -1.0 V_{SCE}$, before cleaning, $\Delta K \cong 8.1 \text{ MPa.m}^{1/2}$, $da/dN \cong 2.9 \times 10^{-6} \text{ mm/cycle}$
 (b) 3.5% NaCl, $E = -1.0 V_{SCE}$, after cleaning, $\Delta K \cong 8.1 \text{ MPa.m}^{1/2}$, $da/dN \cong 2.9 \times 10^{-6} \text{ mm/cycle}$
 86
- Figure 5.21 SEM fractographs showing fatigue cracking of pearlitic AISI 1070
 (a) Buffered 3.5% NaCl, $E = -1.266 V_{SCE}$, before cleaning, $\Delta K \cong 4.6 \text{ MPa.m}^{1/2}$
 (b) Buffered 3.5% NaCl, $E = -1.266 V_{SCE}$, before cleaning, $\Delta K \cong 9.2 \text{ MPa.m}^{1/2}$ 87
- Figure 5.22 SEM fractographs showing fatigue cracking of spheroidized AISI 1070
 (a) Desiccated air, stage-I, $\Delta K \cong 4.4 \text{ MPa.m}^{1/2}$, $da/dN \cong 2.9 \times 10^{-7} \text{ mm/cycle}$
 (b) Desiccated air, stage-II, $\Delta K \cong 9.0 \text{ MPa.m}^{1/2}$, $da/dN \cong 4.6 \times 10^{-6} \text{ mm/cycle}$ 88
- Figure 5.23 SEM fractographs showing fatigue cracking of spheroidized AISI 1070
 (a) 3.5% NaCl, E_{corr} , after cleaning, $\Delta K \cong 8.0 \text{ MPa.m}^{1/2}$, $da/dN \cong 2.9 \times 10^{-7} \text{ mm/cycle}$
 (b) 3.5% NaCl, E_{corr} , after cleaning, $\Delta K \cong 14.1 \text{ MPa.m}^{1/2}$, $da/dN \cong 4.6 \times 10^{-6} \text{ mm/cycle}$
 89
- Figure 5.24 SEM fractographs showing fatigue cracking of spheroidized AISI 1070
 (a) 3.5% NaCl, $E = -1.0 V_{SCE}$, before cleaning, $\Delta K \cong 15.4 \text{ MPa.m}^{1/2}$, end of test
 (b) 3.5% NaCl, $E = -1.0 V_{SCE}$, after cleaning, $\Delta K \cong 15.4 \text{ MPa.m}^{1/2}$, end of test 90

Figure 5.25 SEM fractographs showing fatigue cracking of spheroidized AISI 1070
 (a) Buffered 3.5% NaCl, $E = -1.266 V_{SCE}$, before cleaning, $\Delta K \cong 11.5 \text{ MPa.m}^{1/2}$, end of test
 (b) Buffered 3.5% NaCl, $E = -1.266 V_{SCE}$, after cleaning, $\Delta K \cong 11.5 \text{ MPa.m}^{1/2}$, end of test
 91

Figure 5.26 SEM fractographs showing fatigue cracking of spheroidized AISI 1070
 (a) Overload region, predominately cleavage fracture
 (b) Overload region, microvoid coalescence regions..... 92

Figure 6.1 Three-dimensional plastic zone size [39]..... 94

Figure 6.2 Curve fitting of experimental data in pearlitic AISI 1070 steel 97

Figure 6.3 Curve fitting of experimental data in spheroidized AISI 1070 steel 98

Figure 6.4 Schematic illustration showing a possible model for corrosion fatigue in
 eutectoid steel, (a) spheroidized microstructure, (b) pearlitic microstructure..... 99

Figure 6.5 Schematic theoretical polarization diagram showing possible anodic
 processes at crack tip and precrack surfaces 106

List of Symbols and Abbreviations

a	crack length
A_1, A_3, A_{cm}	the temperatures of phase changes in Fe-C diagram
A_{ct}	crack tip area
A_{pc}	precrack surface area
B	specimen thickness
C	scaling constant
C_s	hydrogen concentration at crack tip surface
C_x	hydrogen concentration at distance x from surface
d	crack tip opening displacement
D	diffusion constant
da/dN	crack growth rate per cycle
da/dt	real time crack velocity
emf	electromotive force potential
E	electrochemical potential
E_m	elastic modulus
E_{corr}	free corrosion potential
E_{oc}	open circuit potential
E_{pit}	pitting potential
F	the Faraday (96500 C)
f	cyclic load frequency

i	current density
I	current
I_{ct}	current at crack tip
I_{pc}	current at precrack surface
K	crack tip stress intensity
K_I, K_{II}, K_{III}	opening, sliding, tearing mode stress intensity, respectively
K_{IC}	fracture toughness
K_{ISCC}	threshold stress intensity for stress corrosion cracking
K_{max}, K_{min}	maximum stress intensity, minimum stress intensity
K_{clo}	stress intensity for crack closure
ΔK	cyclic stress intensity range
ΔK_{eff}	effective cyclic stress intensity range
ΔK_{th}	cyclic threshold stress intensity range
m	scaling exponent in Paris law
n	scaling exponent in Forman equation
N	load cycle number
N_f	fatigue life
N_x	hydrogen trapping sites
P	load, pressure
P_{max}, P_{min}	maximum load, minimum load
r_y	crack tip plastic zone size
Δr_y	crack tip cyclic plastic zone size

R	load ratio = $P_{min}/P_{max} = K_{min}/K_{max}$
S	stress
S_e	endurance or fatigue limit
S_m	mean stress
S_p	interlamellar spacing
S_o	cementite particle separation
t	time variable
t_B	specimen thickness required for plane strain conditions
T	temperature
T_f	time to failure
W	specimen width
Y	geometry factor
α	alpha iron (ferrite)
δ	delta iron
γ	gamma iron (austenite)
x	distance
ϵ	elongation
ν	Poisson's ratio
ρ	density
σ_y	yield strength
σ_{UTS}	ultimate tensile strength
$\Delta\sigma$	cyclic stress range

AGS	austenite grain size
AISI	American iron and steel institute
AR	as received (pearlitic) condition of the material
ASTM	American standards for testing and material
BCC	body centered cubic
CF	corrosion fatigue
CFC	corrosion fatigue cracking
CP	cathodic protection
CT	compact tension
DC	direct current
EAC	environmentally assisted cracking
EIC	environmentally induced cracking
EPFM	elastic-plastic fracture mechanics
FCC	face centered cubic
FCP	fatigue crack propagation
HAZ	heat affected zone
HB	Brinell hardness numbers
HIC	hydrogen induced cracking
HR, HRC	Rockwell hardness numbers, scale C
HT	heat treated (spheroidized) condition of the material
HV	Vickers hardness numbers
LEFM	linear elastic fracture mechanics

LT	long transverse
M	molarity
PSB's	persistent slip bands
RA	reduction in area
RSR	restricted slip reversibility
S, T, L	directions with respect to rolling plane: S- short transverse, T - transverse, L - longitudinal
SCC	stress corrosion cracking
SCE	saturated calomel electrode
SEM	scanning electron microscopy
SEN	single edge notched
SHE	standard hydrogen electrode
TMT	thermomechanical treatment
V_{SCE}	potential with respect to saturated calomel electrode (volts)
V_{SHE}	potential with respect to standard hydrogen electrode (volts)

Acknowledgments

I would like to express my sincere gratitude to Professor Desmond Tromans for his guidance and encouragement throughout this project. Special thanks are extended to other faculty and staff members, and fellow graduate students for valuable discussions.

The author would like to thank all members of his family; his parents, wife and son, for their faithful support and affection. He hopes that he achieved for them what they dreamed of him to be. For them, this thesis is dedicated.

The author is grateful for the financial support provided by Waha Oil Company of Libya, and especially to the guidance of both Engineering and Training Departments.

1 Introduction

Corrosion fatigue (CF) is the combined action of fluctuating stress and a corrosive environment to produce time-dependent cracking. Fatigue and CF are known to be the most common causes of failure of industrial components. As a result, the CF behaviors of ferrous alloys have been studied extensively [1-12]. Material selection is important to ensure that adequate performance characteristics, especially life span, are obtained. Cost and availability dictate materials selection for the industrial processes. In the 1980's, about 30 percent of all carbon steel was purchased in the high carbon grades. High-carbon steel, compared to low carbon, offers superior wear resistance and higher fatigue strengths [13]. Eutectoid steel is used as tendons in prestressed concrete [14], railroad rails [15], and has several applications in marine environments as a cold-drawn wire product [13,16]. The mechanical properties may be varied by changing the morphology of the iron carbide without changing the carbide volume, i.e., moving from a lamellar (pearlitic) distribution to a spheroidal (spheroidized) distribution.

The steel wire industry stimulated the development of high strength steel by the cold drawing process. On the other hand, railroad associations were interested in the wear and fatigue resistance of the eutectoid steel. As a result, the mechanical behavior of eutectoid steels including the effect of interlamellar spacing and thermomechanical processing on strength has been widely investigated [15, 17-20]. While some studies have been conducted on the fatigue and CF behavior of eutectoid steel in the fully pearlitic microstructure [23-32], the spheroidized microstructure has not received the same attention. As a consequence, the influence of microstructure on fatigue behavior is not well established.

The present study examines the effect of carbide morphology on the CF behavior of near-eutectoid steel in aqueous environments by comparing the behavior of pearlitic and spheroidized microstructures. Particular attention was directed to the effect of cathodic protection on fatigue crack propagation because of the uncertainty regarding its usefulness for controlling fatigue cracking. For example, cathodic protection suppresses corrosion but can introduce hydrogen into the steel. The presence of hydrogen may lead to embrittlement and enhanced crack propagation.

2 Literature review

The involvement of an aggressive environment in fatigue crack growth surely depends on a complex interaction between chemical, mechanical and metallurgical factors. Many different types of CF behavior will exist, since each metal-environment combination will interact in different ways. Corrosion fatigue studies benefit greatly from an interdisciplinary approach to test design and analysis of data. A simple schematic diagram of the interaction of a material-environment-stress system is shown in figure 2.1 [1,34]. In many practical situations time-dependent cracking result from the synergistic coupling of tensile stress and corrosive environment, which is generally termed as environmentally induced cracking (EIC) [35]. EIC includes stress corrosion cracking (SCC), corrosion fatigue cracking (CFC) and hydrogen embrittlement or hydrogen induced cracking (HIC). In any given situation, more than one of the three may be operative. The most serious practical situations are in the crosshatched regions, and especially in the center, in which all three phenomena interact.

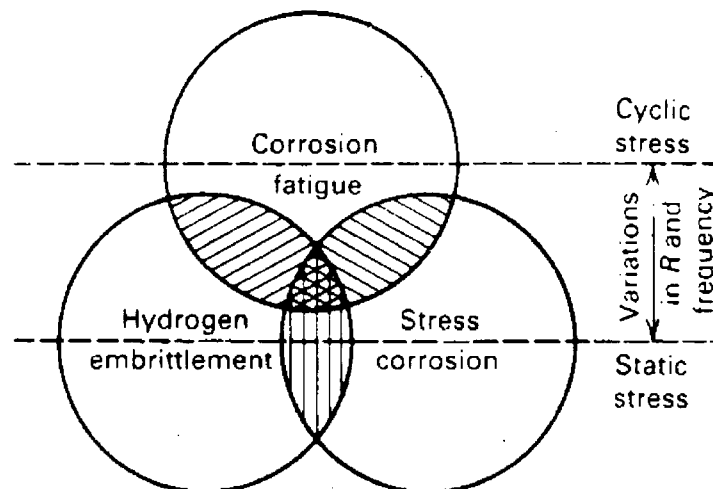


Figure 2.1 Schema showing interaction of cracking forms under static and cyclic loads [1].

2.1 Corrosion fatigue cracking (CFC)

2.1.1 Characteristics of corrosion fatigue cracking

It is difficult to make general statements that differentiate between the several forms of EIC, because of their complexity. However, some useful characteristics are summarized schematically in Figure 2.2 [35]. The result of CFC in steel is a brittle failure (i.e., no gross deformation) with one major crack, usually transgranular, where the macroscopic crack plane is normal to the applied tensile stress. The presence of corrosion products inside cracks is expected and dissolution processes may make cracks appear to be blunt. Any combination of alloy-environment may be susceptible to CFC and the resultant fracture surface appearance may show beach marks and/or striations.

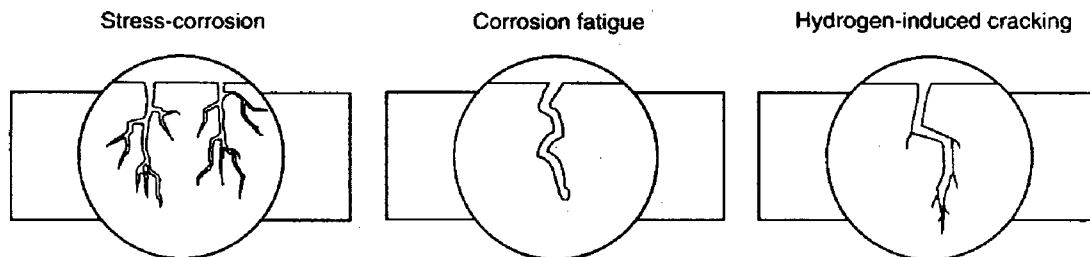


Figure 2.2 Characteristics of environmentally induced cracking forms [35].

2.1.2 Variables affecting corrosion fatigue cracking

There are a large number of variables known to affect fatigue crack growth. These may be divided into three principal groups: mechanical, metallurgical, and environmental. Some of them are inter-related [9, 36, 57].

2.1.2.1 Mechanical variables

Several mechanical variables have been found to affect CFC including:

1. Maximum stress (σ_{max}) or stress-intensity factor (K_{max}) [9, 37-42, 124].
2. Cyclic stress range ($\Delta\sigma$) or stress-intensity factor range (ΔK) [9,37-42].
3. Stress ratio or load ratio (R), ($R = \sigma_{min}/\sigma_{max} = K_{min}/K_{max}$) [9, 27, 42].
4. Cyclic load frequency (f) [9, 35, 93].
5. Loading mode (I- opening, II- sliding, and III- tearing mode) [39, 42].
6. Cyclic load waveform (for constant-amplitude loading) [65, 96].
7. Load interactions in variable-amplitude loading [38, 42, 52, 94-95, 100].
8. Thickness or component size and geometry [37-42, 124].
9. Surface finish. [34, 111].
10. Notches or crack size and shape [9, 37].
11. State of stress [37, 42].
12. Residual stress [43].

2.1.2.2 Metallurgical variables

The metallurgical variables that have been found to affect CFC are:

1. Alloy composition [2, 9, 34-35, 124, 130].
2. Distribution of alloying elements and impurities [2, 9, 21, 35, 130].
3. Microstructure and crystal structure [2-4, 9, 15, 22-23, 32-33, 124, 130].
4. Heat treatment [9, 22-23, 25, 101].
5. Mechanical working [9, 20-21].
6. Preferred orientation of grains and grain boundaries (texture) [20-21, 29, 109, 130].

7. Mechanical properties (strength, fracture toughness, etc.) [9, 27, 32-33].

8. Welding effects [9, 43, 92].

2.1.2.3 Environmental variables

The most important aspect of treatment of CF is the environment. However, other variables are also important, not only in CFC but also in SCC which is operative in some situations.

These variables include:

1. Temperature, T [7, 28, 46, 124].
2. Pressure, P [7, 9].
3. Type of environments (gaseous, liquid, liquid metal, etc.) [7, 9, 50, 66, 93].
4. Partial pressure of damaging species in gaseous environments [93, 135].
5. Concentrations of damaging species in aqueous environments [25, 46, 102].
6. Electrochemical potential or cathodic protection [9, 44, 47].
7. pH [25, 44].
8. Viscosity of environment [35].
9. Fluid flow [35].
10. Coatings, inhibitors, etc. [31, 122].
11. Biological effects [9, 68].

The large number of variables listed above emphasize the complexity of corrosion fatigue behavior. Ideally, corrosion fatigue behavior of a material should be characterized in terms of all of these variables. Wei and Speidel [57] showed that the common practice is to fix some of these variables and, by limiting the study to examination of the selected variables, CF data

could be represented in terms of fatigue life, N_f , or the rate of fatigue crack growth, da/dN , as a function of the selected variables.

$$N_f = F_1(\sigma_{max}, R, f, T, p_i, C_i, \dots) \quad (2.1)$$

$$da/dN = F_2(K_{max}, R, f, T, p_i, C_i, \dots) \quad (2.2)$$

The classical fatigue design approach has involved the use of the stress-fatigue life ($S-N$) curves developed from tests on smooth specimen, where lifetime is defined as the number of cycles, N_f , to failure. Empirical diagrams developed by Wohler ($S-N$ curve) and Goodman (S_e-S_m plot) [37, 42] were used with some safety factor in different engineering fields. Moreover, the Miner [42, 100] cumulative damage law was applied in the case of variable amplitude or random loading. In this approach, crack initiation and crack propagation stages are not distinguished.

The defect-tolerant approach is currently used in design and assessment of metallic structures, which aims to define the fatigue crack propagation phenomenon based on the assumption of pre-existing cracks [6]. A greater industrial emphasis on this approach is evident since the existence of microflaws as initial cracks is inevitable.

2.1.3 Fracture mechanics and corrosion fatigue

It is not the intended purpose to present extensive information on the subject here, but simply to illustrate the power of crack stress analysis. Linear elastic fracture mechanics (LEFM) principles are used to relate the stress magnitude and distribution near the crack tip to a remotely applied stress and crack geometry. LEFM is based on the application of the theory of elasticity to bodies containing cracks or defects. At the crack tip, the material will plastically deform, and a plastic zone will form ahead of the crack. The basis of LEFM

remains valid as long as this plastic zone remains small in relation to the overall dimensions of the body. The stress fields near crack tips can be divided into three basic types, each associated with a local mode of deformation. These basic modes of crack surface displacements are: the opening mode (I), the edge-sliding mode (II), and the tearing mode (III) as illustrated in Figure 2.3.

The parameters K_I , K_{II} and K_{III} are called crack tip stress intensity factors for the corresponding three modes in Figure 2.3. They represent the strength of the stress fields surrounding the crack tip. Physically, they may be regarded as the intensity of load transmittal through the crack tip region. These intensity factors play a large role as fracture correlation parameters in current practice.

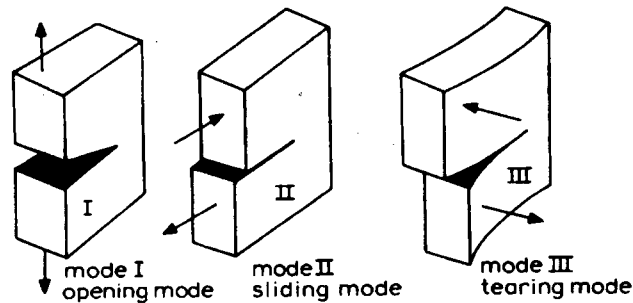


Figure 2.3 Loading modes [39].

A wide plate with an interior crack of length ($2a$), a straight crack front, and a crack plane perpendicular to a remotely applied tension stress, σ , would have a stress intensity factor, K_I , given by the following equation:

$$K_I = Y\sigma\sqrt{\pi a} \quad (2.3)$$

where Y is a geometry factor depending on the ratio of the crack length to the width of the plate.

2.1.4 Corrosion fatigue failures

Engineering components are designed to withstand numerous load or stress reversals during their service lives. Load spectra may be introduced either between fixed strain or fixed stress limits; Hence, the fatigue process in a given situation may be governed by a strain or stress controlled condition.

Generally, the fatigue life may be viewed as a three-stage process involving crack initiation, crack propagation and final failure stages. When defects, metallurgical flaws or corrosion pits are preexisting, the initiation stage is shortened drastically or completely eliminated, resulting in a reduction in the cyclic lifetime.

2.1.4.1 Crack initiation

Corrosion fatigue cracks are always initiated at a surface. This is usually the exterior surface unless there are sub-surface defects that act as stress concentration sites and promote sub-surface crack initiation. Unlike monotonic tensile deformation, there is no rotation or orientation change of the slip plane and the slip direction during fully reversed cyclic loading [42]. The evolution of persistent slip bands (PSB's) is specific to cyclic deformation. Sharp peaks and valleys, known as *extrusions* and *intrusions*, are produced at sites where the PSB's emerges at the specimen surface. Figure 2.4 shows the initiation of cracks in PSB's.

2.1.4.2 Crack propagation

Crack propagation is usually divided into three stages as schematically illustrated in Figure 2.5. Stage-I crack propagation commences at the onset of threshold cracking conditions. The

threshold (ΔK_{th}) is the stress intensity range value below which existing cracks or defects are in the non-propagating condition for a specified number of load cycles. Stage-I cracking is associated with low crack growth rate, usually $< 10^{-6}$ mm/cycle. This stage is very dependent on microstructure, mean stress, and environment [56, 64].

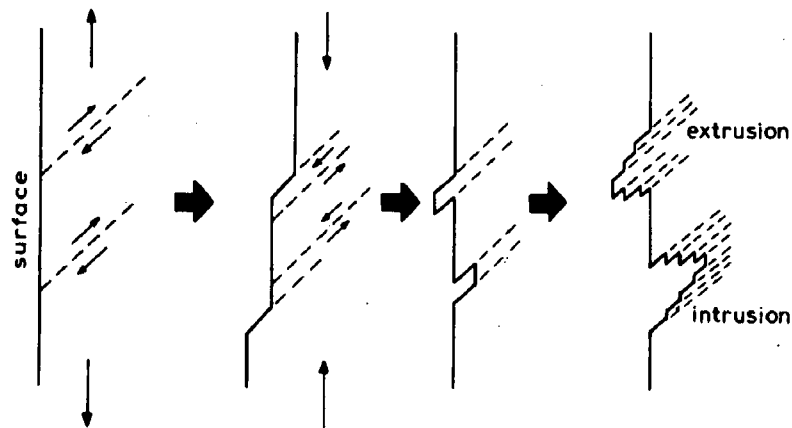


Figure 2.4 Initiation of cracks in persistent slip bands (PSB's) [39].

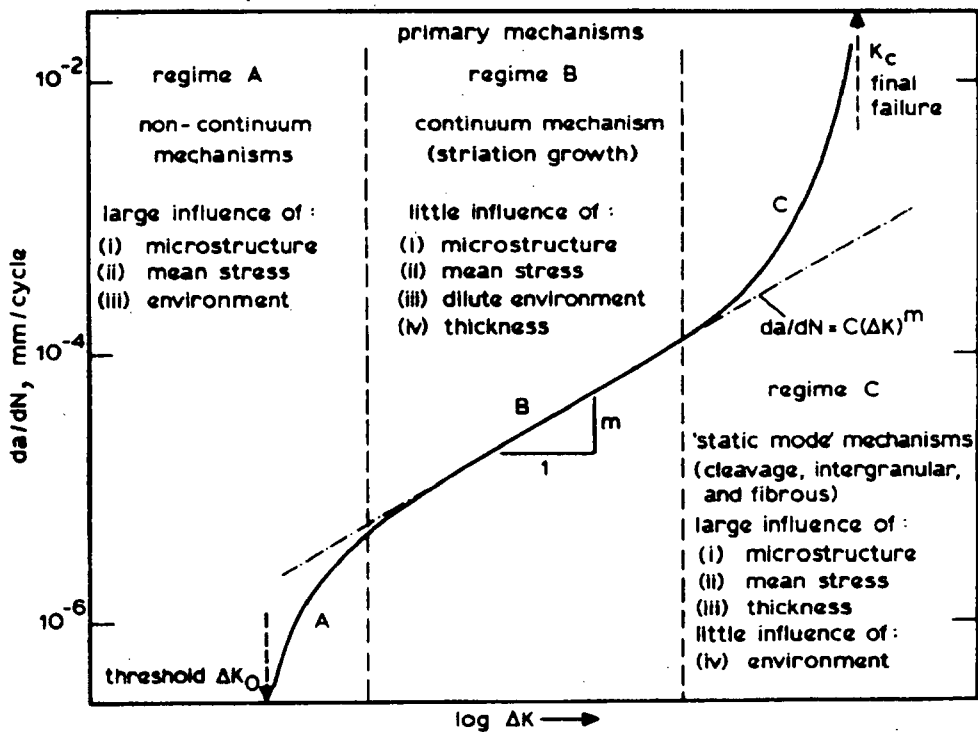


Figure 2.5 Schematic illustration of variation of fatigue-crack-growth rate, da/dN , with alternating stress intensity, ΔK , in steels, showing regions of primary crack-growth mechanisms [56].

The widely used fatigue crack propagation (FCP) expression represented by Equation (2.4) is called the Paris power law, and has been successfully fitted to test results in region II but is not applicable to regions I and III [98]. The exponent, m , is a constant that varies between 2 and 4 for most engineering materials. At extreme values of ΔK , both below and above that of the Paris regime, there is a precipitous change in crack growth rates with increasing ΔK as shown in figure 2.5.

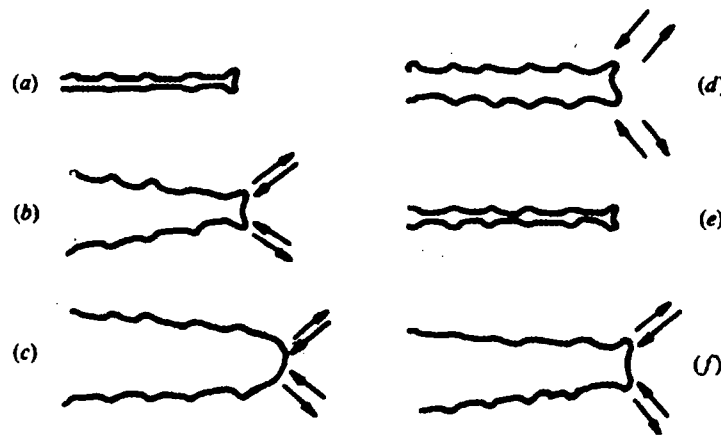


Figure 2.7 An idealization of plastic blunting and re-sharpening which leads to stage-II fatigue crack growth in fully reversed fatigue. (a) Zero load, (b) small tensile load, (c) peak tensile load, (d) onset of load reversal, (e) peak compressive load, and (f) small tensile load in the subsequent tensile cycle. Arrows indicate slip direction [42].

Smiths [92] used a modified expression for the power law and fitted the FCP test results of fillet welds to a model which includes the threshold stress intensity factor (ΔK_{th}). The model represented by Equation (2.5) was first proposed by Hartman and Schijve [93].

$$\frac{da}{dN} = C(\Delta K - \Delta K_{th})^m \quad (2.5)$$

where $(\Delta K - \Delta K_{th})$ was considered to be an effective cyclic stress intensity.

A similar expression to Equation (2.5) with $m = 2$, was proposed by Zheng [98-99], and claimed that it gave better fit to fatigue crack propagation (FCP) test results than Equation (2.4). The exponent m , the FCP coefficient, C , and ΔK_{th} were thought to be the governing factors of FCP rates of metals. Richards and Lindley [124] reported that ΔK_{th} in Eq. (2.5) was dependent on the mean stress and varied between ~ 2 and $4 \text{ MPa}\cdot\text{m}^{1/2}$ for several steels.

Considering stage II-III behavior, Forman *et al.* [97] proposed the following empirical expression,

$$\frac{da}{dN} = \frac{C(\Delta K)^n}{(1-R)K_c - \Delta K} \quad (2.6)$$

where R is the stress ratio ($R = \sigma_{min}/\sigma_{max} = K_{min}/K_{max}$), and K_c is fracture toughness of the material. Hartman and Schijve [93] confirmed that Equation (2.6) accounted for the influence of R according to their test results but it could not describe the FCP behavior in the near-threshold region.

Many attempts have been made to develop expressions describing the whole FCP curve [98, 124]. One example of these expressions is [93, 98],

$$\frac{da}{dN} = \frac{C(\Delta K - \Delta K_{th})^n}{\{(1-R)K_c - K_{max}\}} \quad (2.7)$$

Equation (2.7) may be looked at as a combination of Equations (2.5) and (2.6) and incorporates both the lower and upper limit of the FCP curve, ΔK_{th} and K_c , respectively.

2.1.5 Corrosion fatigue endurance

A corrosive environment may reduce the crack initiation time by localized attack (dissolution) to form a stress concentration. Corrosion attack is likely to be favored at newly

formed, unfiled metal surfaces formed at a PSB [44]. However, little difference between results in seawater of welded joints of steel and those obtained in air was reported by Scott [44]. This indicates that seawater corrosion is not contributing much to initiation of cracks in welded joints, which are believed to contain their own defects. Consequently, the reduction in these situations of fatigue strength is mainly attributable to the effect of the environment on stage-I of crack growth [45].

The importance of surface finish and the adverse effect of corrosion is well known. Figure 2.8 shows the serious loss in fatigue (endurance) limit of smooth specimens that is associated with a deterioration in surface quality. For most steel-environment combinations there is no true fatigue limit; given enough time, a crack will finally propagate by CF up to the critical size for final catastrophic crack propagation or overload failure.

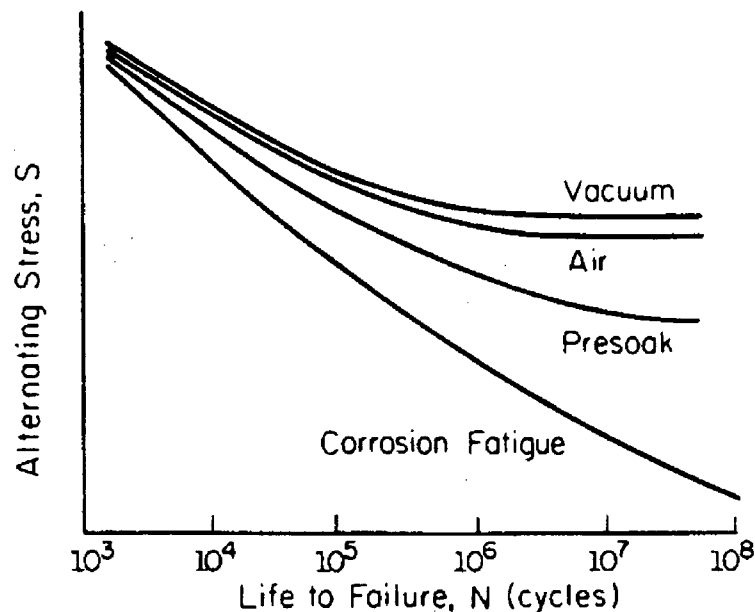


Figure 2.8 Effect of various environments on the S-N curve of steel [37].

The interaction of an aggressive environment and cyclic loading leads to premature failure of materials by cracking. The damage contribution is usually greater than the sum of the mechanical and chemical components if each was acting in isolation. It is important to notice that all observed fatigue failures in service are essentially corrosion fatigue failures, since only fatigue occurring in an absolute vacuum can be termed as pure fatigue. However, normally, dry air is considered to be a relatively *inert* environment.

2.1.6 Corrosion fatigue mechanisms

In the FCP process, both local anodic dissolution of material at the crack tip and hydrogen entrance into the crack tip plastic zone may occur simultaneously. They both contribute to the acceleration of crack propagation [65]. Depending on the concentration of hydrogen in the vicinity of the crack tip material, either one of these two factors may play a more important role on the fatigue process than the other. It is known that during CFC, the crack tip becomes anodic to the rest of the material surface [122]. Generally, anodic polarization increases the materials dissolution and decreases hydrogen generation, whereas cathodic polarization decreases the anodic dissolution and increases hydrogen generation (and possibility of hydrogen embrittlement).

2.1.6.1 Hydrogen embrittlement

One of the most significant limitations on the use of high strength steel components is hydrogen embrittlement and/or hydrogen induced cracking (HIC). HIC is a major problem in the oil and gas industry and is observed mainly at low temperatures ($<30^{\circ}\text{C}$) in ferritic steel in

environments containing hydrogen sulphide [131]. HIC is often accompanied by sonic emissions [133].

Hydrogen, in the atomic form, can enter the materials from many sources such as: interaction with H_2O during steel making, and welding, and hydrogen generation during pickling, coating, electroplating, corrosion and cathodic protection [34]. Its degrading effect on the mechanical properties of material, particularly steels, has been extensively analyzed and the related literature is voluminous. It can produce a range of deterioration resulting in reduced ductility to brittle fracture.

Hydrogen embrittlement is a time-dependent phenomenon, and diffusion and solubility of atomic hydrogen within the metal lattice are the controlling factors. The overall solubility is determined by the lattice solubility and the number of trapping sites (N_x) existing in the material [132]. Other than dislocations, the most likely contribution from other trapping sites is at interfaces. There is also a trend for N_x to increase with either increasing carbon content or strength level of the steel [132].

Embrittlement in steel is reversible if microcracks have not yet initiated, and ductility can be restored by relieving the applied stress and aging at room temperature to allow hydrogen to diffuse out of the steel [125, 128-129]. Figure 2.9 illustrates the interrelated factors associated with hydrogen embrittlement [34].

The effect of hydrogen charging is particularly severe in steels with hardness values greater than HRC 22 [35]. Griffiths *et al.* [127] studied its effect on the corrosion fatigue crack growth rates of AISI 4340 steel in aerated 3.5% $NaCl$ solution. They observed that bulk

charging for 70 and 147 days at $-1100 \text{ mV}_{\text{SCE}}$ enhanced fatigue crack rates in the Paris law region by a factor of 3 and 7, respectively, relative to the uncharged condition.

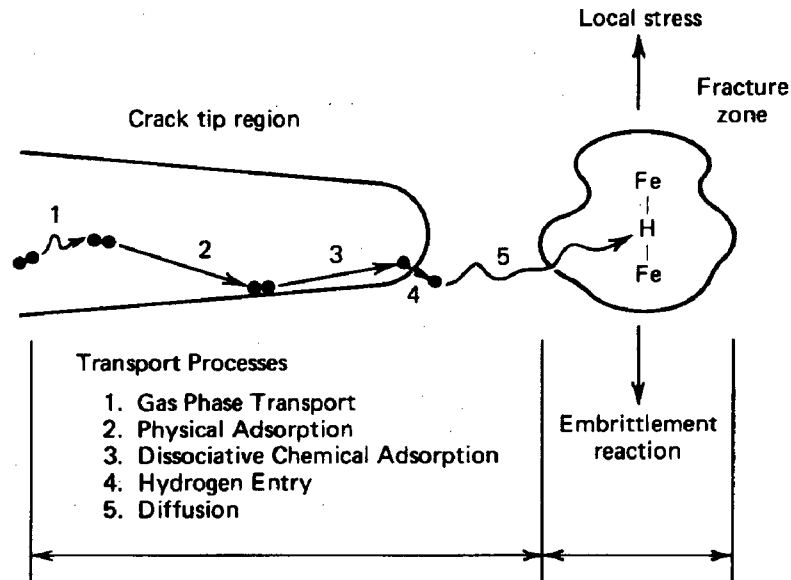


Figure 2.9 Various processes involved in the hydrogen embrittlement of ferrous alloys [34].

Different forms of hydrogen degradation exist, and the effect of hydrogen on the mechanical properties can be quite complex. Therefore, a number of models have been proposed to describe its mechanism [34-35, 90, 125, 135].

The decohesion mode involves weakening of highly strained atomic bonds at a crack tip. This is particularly attractive for the case of high strength steels with brittle failure modes [35]. Tromans [90] reviewed the hydrogen embrittlement of iron and steels and concluded that cracking is promoted by a sufficient decrease in surface energy due to hydrogen entry, and showed that high local stresses together with dissolved hydrogen, produced the required changes in surface energy. This is consistent with the requirements of the decohesion model [128].

Another perception is that hydrogen embrittlement is caused by the interaction of hydrogen with the formation and movement of dislocations, thereby reducing the ability of the material to deform plastically [128, 135]. Furthermore, hydrogen can be transported by moving dislocations, and may increase the dislocation mobility. More direct support was reported [129, 135] for the enhancement of plastic instability by hydrogen through an influence on deformation behavior.

2.1.6.2 Anodic dissolution

Metals are often subject to oxidation or electrochemical corrosion. Different metals behave quite differently when placed in metallic contact with other metals (a galvanic couple). The least noble metal becomes more anodic (oxidation enhanced) and the more noble metal tends to become more cathodic (oxidation decreased). In aqueous solutions the cathodic reaction usually involves reduction of dissolved oxygen at the metal surface or reduction of H^+ ions if pH is sufficiently low. Galvanic effect may be generated between two phases in the same alloy.

For a metal or alloy to corrode evenly, all regions of the surface must exhibit identical anodic behavior, but this is rarely the case [130]. Under appropriate metallurgical and chemical conditions, anodic dissolution may be enhanced at grain boundaries, especially if solute segregation is present, leading to an intergranular failure mode. The rupture of corrosion films at the crack tip may lead to preferential dissolution (anodic activity) of the crack tip. Jones [126] has used this as a basis to develop a unified mechanism of SCC and CFC based on vacancy injection at the corroding crack tip.

2.1.7 Crack growth retardation effects

Elber [62] first introduced the idea that the permanent tensile plastic deformation left in the wake of the propagating crack will directly result in a crack closure phenomenon. A fatigue crack, propagating under zero-to-tension loading, may be partially or completely closed at zero load. Crack closure can greatly reduce rates of fatigue crack propagation. The true or effective crack tip driving force (ΔK_{eff}) is reduced below the applied ΔK because of the reduced crack tip displacement range and is given by:

$$\Delta K_{eff} = K_{max} - K_{clo} \quad (2.8)$$

Where K_{clo} is the stress intensity factor at which the crack begins to close, i.e., the opposing crack faces come into contact. Closure phenomena are produced by a variety of mechanisms and are particularly relevant to fatigue crack propagation in the near-threshold regime. The principal crack closure mechanisms are shown schematically in Figure 2.10 [63]. These include plasticity-induced, oxide-induced, roughness-induced, viscous fluid-induced, and phase transformation-induced closure effects. Taylor [64], and Suresh and Ritchie [63] reviewed these mechanisms and critically examined the many sources of fatigue crack closure.

The oxide-induced closure effects are sometimes referred to as corrosion-product-induced closure effects [59]. Moreover, Gan and Weertman [94-95] showed experimentally that "*the crack closure stress and propagation rate are affected by the overload over a distance several times the size of the overload plastic zone.*"

Cracking at stage-II ΔK values may be retarded below growth rates observed for air or vacuum due to corrosion product formation within the crack [67]. The crack may behave as a crevice and limited mass transport inside crevices leads to localized changes in the solution

chemistry which may aggravate dissolution and corrosion product formation in the crack [59]. As a consequence of crack closure, the shape of the striations (Fig. 2.4) formed during the crack propagation process will be changed by contact of opposing surfaces which flattens the striations.

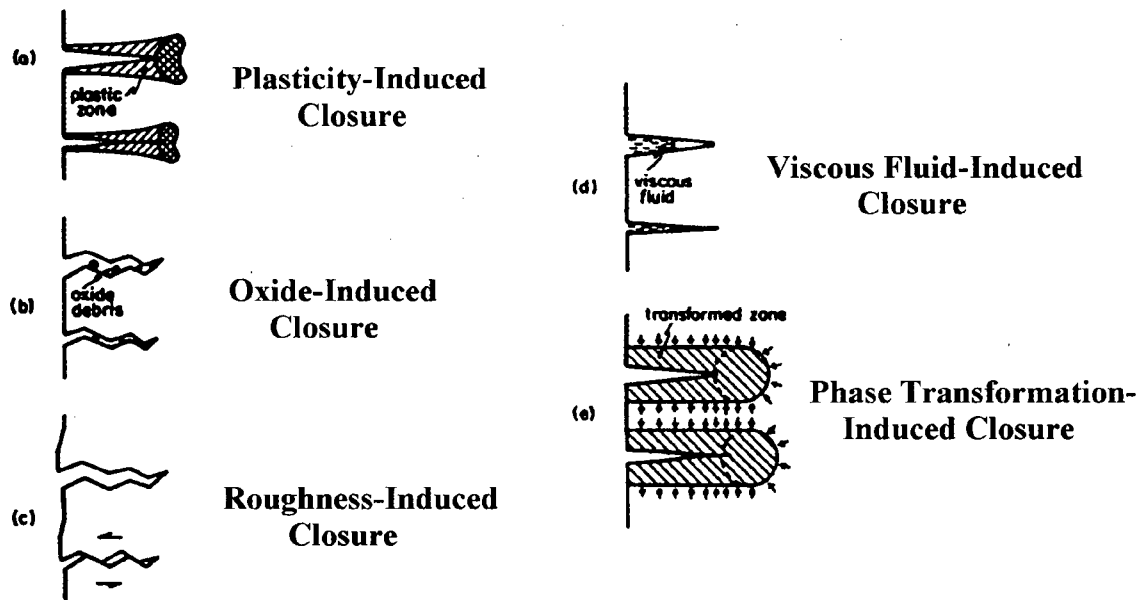


Figure 2.10 Schematic illustration of the principal mechanisms of fatigue crack closure [63].

2.1.8 Prevention of CFC

Corrosion fatigue cracking can be mitigated by any means that reduce the general corrosion rate or remove the cyclic stresses or decrease the cyclic load. Corrosion control methods maintain the structural integrity and may include: cathodic protection, corrosion inhibitors, pH control, surface coating and plating, and use of more corrosion resistance materials.

2.1.8.1 Cathodic protection (CP)

CP systems can prevent corrosion pitting in steels, thus minimizing CF crack initiation. The bases of most corrosion control methods are always referred to the Pourbaix diagram (Fig. 2.11). This is a thermodynamic diagram showing equilibria and phase stability for reactions of iron in an aqueous solution. Modest cathodic protection (electrode potential of structure maintained at ~ -0.49 V_{SHE}) is useful in mitigating corrosion fatigue of high-strength steels. Excessive CP causes increased crack growth rate in steels and lowers the fatigue strength of welded specimens [46, 47]. Evidence in support of a hydrogen embrittlement mechanism for the accelerated fatigue crack growth rates in structural steels under cathodic protection in marine environments has been accumulating rapidly in recent years [48].

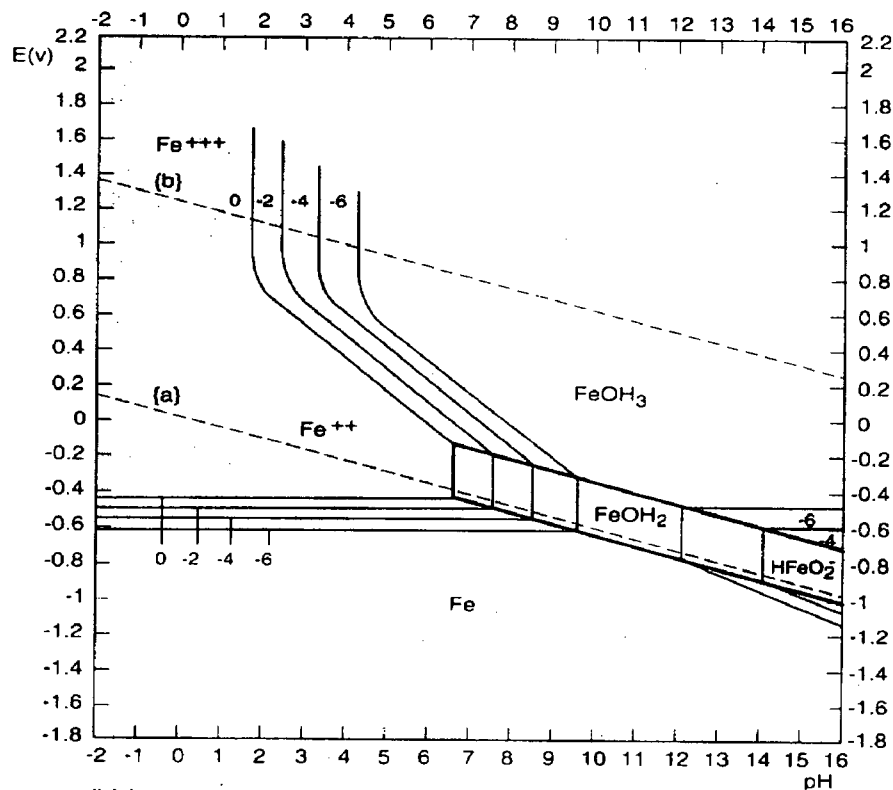


Figure 2.11 Pourbaix diagram for iron [35].

Sacrificial zinc anodes coupled to steel structures were reported to increase the fatigue life of carbon steel to that in air. Husain *et al.*[31] reported that galvanizing eliminates the effect of corrosion on CF behavior of eutectoid steel wires, due to cathodic protection of the steel.

2.1.8.2 Corrosion inhibitors

A great number of corrosion inhibitors of different types have been developed empirically [35, 104-105]. Adsorption-type inhibitors generally reduce the anodic area available for corrosion and improve the resistance to CF crack initiation.

The influence of inhibitors on fatigue crack growth rate in a corrosive environment has been discussed by Panasyuk and Ratych [122]. Various corrosion inhibitors were found to mitigate either the local anodic dissolution or hydrogen embrittlement mechanism.

2.1.8.3 pH control

Steels have lower corrosion rates at pH 9-12, where the formation of a passive layer is favored. By controlling the pH of the solution, corrosion fatigue resistance may be improved (Fig. 2.11). However, it is often difficult to change pH in industrial situations.

2.1.8.4 Surface coatings and plating

Many parts are shot peened (see 2.1.8.6) prior to chromium and nickel plating to produce residual compressive stresses at the surface and counteract the harmful effects of plating on their fatigue life. Plating can introduce residual tensile stresses and generate hydrogen that leads to hydrogen embrittlement of the underlying metal. Also, defects in the plating, such as cracks, may propagate into the base metal during fatigue. However, when the surface of the

base metal is compressively stressed by peening, the cracks cannot propagate into the base metal.

Plating improves the general corrosion resistance of the component, minimizing the rate of corrosion in fatigue. Hence, the fatigue life of the plated part is more than that without plating. It is found that *Ni-Cr* plating reduces fatigue strength in air, but sometimes it is beneficial in a corrosive environment. *Cd-Zn-Pb* plating is desirable [37], and it is possible to overcome the hydrogen embrittlement problems associated with cathodic charging by subjecting the electroplated material to a baking treatment [34, 125]. This involves heating the part to a moderate temperature for a sufficient period of time to allow hydrogen to diffuse out of the steel.

2.1.8.5 Corrosion-resistant materials

Stainless steels are generally a better choice for resistance to CFC in a range of aqueous environments. However, in a welded structure, the heat affected zone (HAZ) will be the most susceptible to corrosion fatigue [49]. The intergranular corrosion problem of stainless steels welded joints is generally attributed to formation of chromium carbides and local *Cr*-depletion of the adjacent alloy matrix. Increasing the chromium or reducing the carbon content are methods used to minimize intergranular corrosion of stainless steels. Another method is to add small amounts of titanium or niobium (stabilized grades) which have a greater affinity for carbon than *Cr* [130].

2.1.8.6 Reduction of stresses

Reducing cyclic stresses will definitely decrease the crack growth rate. Also, a small increase in the cyclic stress (overloads) followed by a decrease to the previous level may retard cracking [95]. If the overload is large enough, crack arrest can occur and the growth of fatigue stops completely [37, 52]. Overload retardation is primarily due to residual compressive stresses generated in the crack tip region and associated with crack closure effects. The FCP rate is most strongly affected by the overload within a crack propagation distance approximately equal to the overload plastic zone [94-95]. These effects are utilized during the periodic hydrostatic testing of pressure vessels.

The effective applied stress intensity should be maintained at the minimum possible level. Stress relief any tensile residual stresses of structural steels is a mandatory to reduce the mean tensile stress level and enhance the resistance to CFC. Reducing the stress concentration factors by eliminating sharp changes in section size is also beneficial [43].

Introducing compressive residual stress at the surface by shot peening and cold rolling has a very desirable effect on the fatigue life. Smiths [92] reported that needle peening of weld toes improved the fatigue life by retarding crack growth to a depth of half the diameter of the peening tool. Machining processes are also a determinant factor in fatigue life. For example, rolled threads have over 400% better endurance limit than machine cut threads.

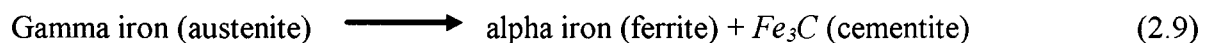
Surface treatment such as; gentle grinding, polishing, case hardening, carburizing, nitriding may impart beneficial effects on fatigue life, provided that residual compressive stresses are introduced by these operations.

2.2 The eutectoid steel

Pure iron forms different crystal structures depending on the temperature. At high temperatures (above 1394°C) iron forms a BCC structure called (δ). At a lower temperature (below 1394°C) iron transforms to the FCC structure called austenite or (γ). Below 910°C, iron transforms again to the BCC structure called ferrite or (α). In the $Fe-C$ system, there is a stoichiometric compound Fe_3C , called cementite. A eutectoid reaction occurs in the $Fe-Fe_3C$ system at 0.77% C and 727°C, resulting in a lamellar structure of α and Fe_3C plates known as pearlite. Commercial carbon steels are two phase steels composed of $\alpha-Fe$ and Fe_3C , where the proportion of Fe_3C phase is determined by the C -content. By controlling the amount, size, and morphology of Fe_3C phase, we can control the degree of dispersion strengthening by Fe_3C .

2.2.1 The eutectoid reaction

The eutectoid reaction is a solid state reaction where one solid phase transforms into two solid phases. Figure 2.12 shows the iron-carbon phase diagram. The diagram shows iron and carbon combined to form Fe_3C at 6.69% C . At lower C -contents, α and Fe_3C are present in different proportions, resulting in a range of steel alloys. Three significant regions can be made relative to the steel portion of the diagram. They are the eutectoid, that corresponds to an alloy containing 0.77% carbon, the hypoeutectoid ($< 0.77\% C$), and the hypereutectoid ($> 0.77\% C$). By heating the eutectoid alloy above 727°C and allowing it to cool slowly, the eutectoid reaction ensues. The following equation represents this transformation.



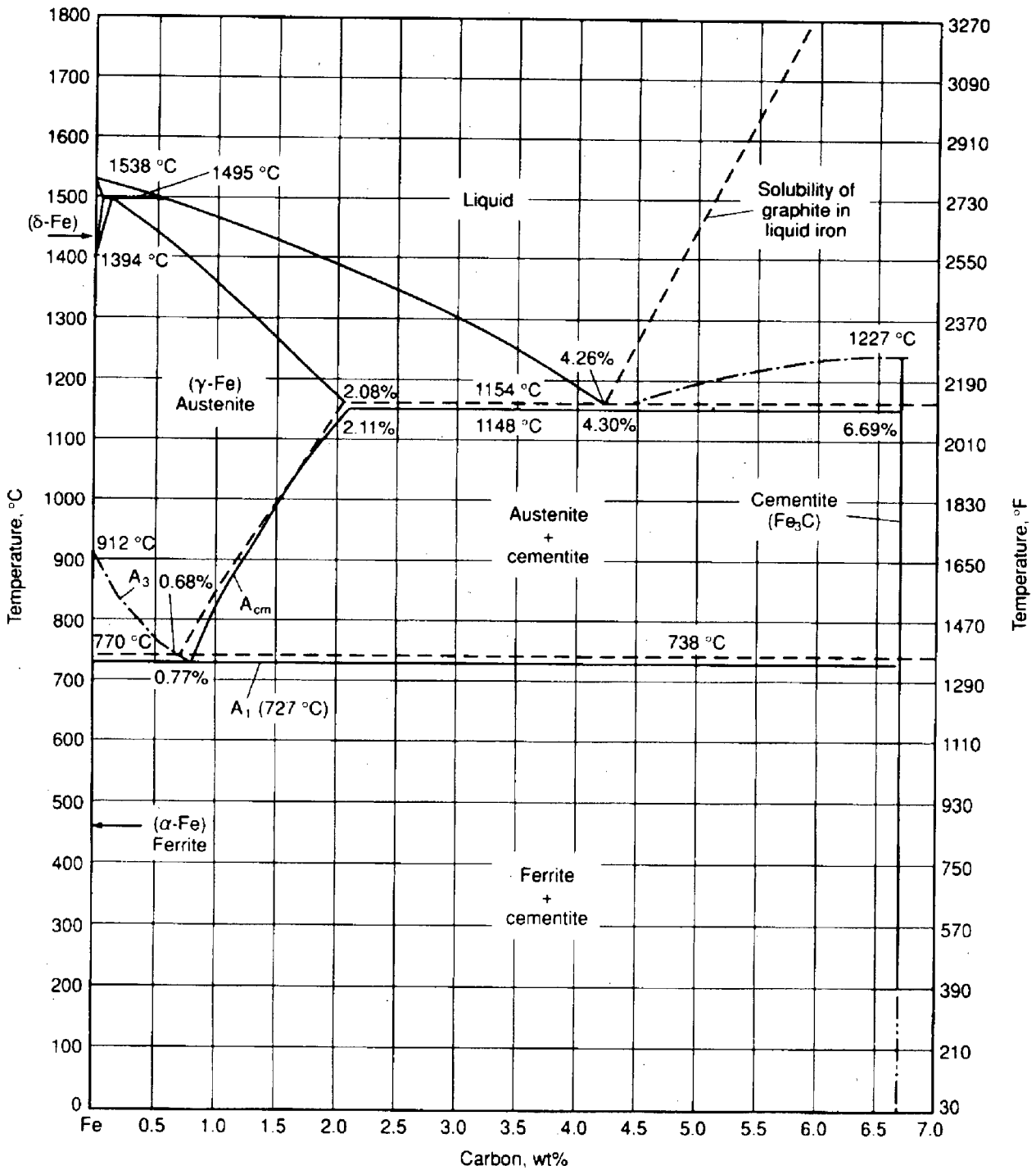


Figure 2.12 The Fe-C equilibrium diagram up to 6.69% C. Solid lines indicate Fe-Fe₃C diagram; dashed lines indicate Fe-graphite diagram [54].

The fully pearlitic microstructures are essentially composed of alternating lamellae of α -Fe and Fe_3C . In a slightly hypoeutectoid steel, the microstructure would consist of pearlite with a proeutectoid grain boundary ferrite network. The kinetics of austenite-pearlite transformation in eutectoid steel is documented elsewhere [70-74] and is not in the scope of this work.

2.2.2 Pearlitic and spheroidized microstructures

Two extreme morphologies of cementite in ferrite can easily be produced in a eutectoid steel; pearlite and the spheroidized microstructure. Spheroidizing of steel incorporate heating near the eutectoid temperature and cooling to produce a structure of globular carbides in a ferritic matrix. The heating step may be achieved by prolonged holding at a temperature just below the A_1 temperature shown in Figure 2.12 [55]. Other methods for spheroidizing include heating and cooling alternately between temperatures that are above A_{c1} and just below A_{r1} (A_{c1} and A_{r1} are the temperatures of $\gamma \leftrightarrow$ pearlite transformation during heating and cooling, respectively), or heating to a temperature above A_{c1} , and then either cooling very slowly in the furnace or holding at a temperature just below A_{r1} . Carbide spheroidization usually starts at prior austenite grain boundaries and, to a lesser extent, within the pearlite colonies [28]. Spheroidization and coarsening of carbide are diffusion controlled [117]. A detailed characterization of the extent and kinetics of these processes was not undertaken in this investigation, and has been addressed by other workers elsewhere [107]. Spheroidizing is conducted when soft annealed high-carbon steel is intended for applications requiring maximum cold forming.

2.2.3 Mechanical properties of eutectoid steel

Pearlitic eutectoid steels have reasonable strength and wear resistance but can suffer from problems of poor ductility and toughness. The microstructure controls the resultant mechanical properties. It is well established that the strength of pearlitic eutectoid steels depends on the initial interlamellar spacing [17-18, 20]. The yield strength (σ_y) increases as the lamellar spacing decreases, and the values of 690 MPa and 330 MPa for fine (0.12 μm) and coarse (0.32 μm) lamellar spacing, respectively, were reported [23]. Mathematical relationships that appear to describe the reported data [18-20, 29, 123] are of the well-known Hall-Petch equation form [34]:

$$\sigma_y = \sigma_o + k(S_p)^x \quad (2.10)$$

where σ_y is the yield stress, S_p is the interlamellar spacing and (σ_o , k , x) are constants. Although there is a general agreement on the form of Equation (2.10), discussion continues on the proper choice of the exponent (x). In addition, many researchers [20, 29] have found that the Hall-Petch relation was not obeyed since a negative intercept was obtained, which is not acceptable.

It has been shown that the interlamellar spacing of pearlitic steels is a function of cooling rate and/or heat treatment [15, 18-19, 23, 68], while the austenitization temperature controls the prior austenite grain size (AGS). The AGS was found to have no effect on the fracture stress, except through its influence on the interlamellar spacing [18]. In contrast, it was previously reported by Querales and Byrane [20] that the AGS was related to the yield strength through an equation similar to Equation (2.10). According to these authors, there was no doubt that "*the austenite grain refinement due to thermomechanical treatment (TMT)*

was an important factor in increasing the strength of pearlite." In addition, Park and Bernstein [109] reported that *"prior AGS is the dominant microstructural factor controlling the fracture toughness of pearlitic steels; the finer the grain size, the greater the toughness."*

The effect of pearlite morphology on impact toughness of eutectoid steel has been demonstrated by Garbarz and Pickering [118].

All reported research agreed that the strength of hot-rolled bars of eutectoid steel is further improved by cold working. Querales and Byrane [20] reported that 75% cold rolling reduced the interlamellar spacing of pearlitic steel to about one half. Microalloying additions such as vanadium and chromium to eutectoid high-carbon steels have also been reported to improve their mechanical properties [119].

Lewandowski and Thompson [19] reported that *"the room temperature tensile ductility, as measured by the reduction in area or fracture strain, is dependent on both the prior AGS and S_p ."* Increasing the prior AGS reduced the ductility for an equivalent S_p .

Tensile test specimens of pearlitic steel exhibit predominately cleavage fracture behavior at room temperature [15, 18, 109]. Fracture initiation sites were often associated with fractured inclusions in the material or flaws on the order of the pearlite colony size. A modified 1070 steel having a fine grained tempered martensitic microstructure with slight spheroidization of the carbides was reported by Dougherty *et al.* [26] to fail in a ductile manner by microvoid coalescence.

Dougherty *et al.* also studied the cyclic stress response, strain resistance, and low cycle fatigue life of this material. Softening and hardening behavior was observed depending on the applied cyclic strain amplitude. Sunwoo *et al.* [29] reported that *"cyclic deformation behavior*

of pearlitic eutectoid steel was strongly dependent on the interlamellar spacing and strain amplitude with cyclic softening in fine pearlite, cyclic hardening in coarse pearlite, and both cyclic softening and hardening in medium pearlite at low and high strain amplitudes, respectively”.

Due to its practical significance, the wear and friction behavior of eutectoid and near-eutectoid steels have been studied extensively [112-116]. It was found that interlamellar spacing and volume fraction of pearlite have a great effect on the wear rate and the coefficient of friction of eutectoid and hypoeutectoid steels.

Wear resistance was generally associated with high hardness. However, Kalousek et al. [113] observed that the dry wear resistance of pearlite was essentially independent of hardness. Furthermore, pearlite was found to have the highest wear resistance compared with tempered martensite and bainite microstructures of 1070 rail steel. It was proposed that lowering the sulphur content in this steel should markedly lower the dry wear rate. Wang and Lei [114] did not find obvious differences in wear volume for the various microstructures under mild wear. However, considerable difference was observed under severe wear conditions, and pearlite was also reported to have the highest resistance. It was concluded that higher hardness does not necessarily mean better wear resistance.

Lesuer *et al.* [121] proposed a fracture model for spheroidized hypereutectoid steels that treats the ferrite and carbide microstructure as a composite material. The fracture characteristics and strengths of such particulate composites depend on carbon content, carbide size and carbide strength. The absolute value of the fracture strengths of cementite ranged from 2400 to 5000 MPa. The finer the size of the coarse carbides, the higher the fracture

strength of the composite. For a given carbide size, the higher the carbide volume fraction, the higher the fracture strength of the composite. Karlsson and Linder [123] demonstrated that the yield behavior of ferrite, pearlite and spheroidite could be reconciled with the Hall-Petch equation, and showed that yielding was controlled by the free-slip distance in the ferrite phase.

Much attention has been directed to the fully pearlitic steels due to the fact that the fully pearlitic condition constitutes the major uses of this material as discussed in the next section.

2.2.4 Industrial applications of eutectoid steel

About 30% of the North American production of *C*-steel rod and drawn wire consists of high-*C* grades, such as AISI 1070, 1075 and 1080 [13, 16]. To control tensile strength levels to required specifications, a tolerance of only 0.05% in *C* content and 0.20% for *Mn* is often specified. Steel cords, cables or wire ropes are used in several high duty engineering applications, e.g., drilling and mining operations, innerspring mattress springs, shafts, elevators, arresting cables on aircraft carriers [30], and in tethered buoyant structures for offshore oil extraction [31]. Growth is also noted in the flat and shaped wire markets. The diversity of specification choices in high-*C* steel wire allows wire to be customized to the exact standards for a given application.

The AISI 1070 grade, in the hardened condition, is utilized as a bearing steel [108]. Eutectoid steel with fully pearlitic microstructure is used for both railroad rails stock and wheel material [19, 28, 29, 54, 112-115]. It was estimated that the North American railroads were spending \$600 million annually for the direct replacement costs of deteriorated rails in the early 1980's [115]. This explains the importance of wear and fatigue resistance in selecting the rail material. Pearlitic steels are also used as tendons in prestressed concrete and in cable

stayed bridges [14]. In the last decade, prestressed concrete has been utilized in large civil engineering structures, such as long span bridges or nuclear power plants [24]. High-tensile steel for prestressing usually takes one of three forms: wires, strands or bars. The properties of these cables are specified in well-known standards such as; ASTM A 416 and ASTM A 421 [75,76]. However, These standards do not specify composition limits. Other carbon steel wires, including the eutectoid steels, are covered under ASTM A 510M standard specification [89]. A typical cord is shown in Figure 2.13.

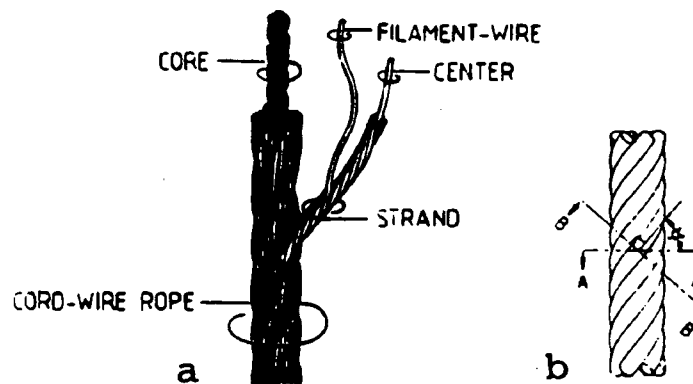


Figure 2.13 (a) Various components of a typical cord / rope; (b) helix angle [30].

High-C wire can be bent, coiled, coined, crimped, drawn, drilled, forged, grooved, punched, rolled, sheared, soldered, stamped, and straightened. Cold drawn high-C wire in AISI 1070 and 1075 grades can attain a strength of 1700-3000 MPa [30]. It is used in springs, wire brushes, tire cord wire, wire rope, aggregate screens, spokes, bobby pins, chains, fencing, flexible shafts, lock washers, screw drivers, strapping, ties for cotton baling and torque rods [16]. The general requirements for cold-rolled carbon spring steel strip are covered in ASTM A 682M standard specification [87]. Other cold-rolled strip steel may be furnished in the

pearlitic or spheroidized microstructure according to the standard specification ASTM A 684M [88].

2.2.5 Corrosion of eutectoid steel

Environmental degradation of materials is often an important performance limitation. Structure and microstructure both determine how electrochemical corrosion proceeds. At the microstructural level, the ferrite and Fe_3C lamellae in pearlite have different electromotive force potentials (*emf*) values, and so one will be attacked preferentially. The influence of heterogeneity on the dissolution behavior of engineering alloys has been well documented by Pourbiax [103], Uhlig [104], and Fontana [105]. In the same manner, this is how microstructures are etched for conventional metallographic examination.

Gilehrst and Narayan [25] studied the electrochemical behavior of eutectoid steel in different environments and heat treatment conditions. They observed no significant difference between the behavior of differently heat treated wires of eutectoid steel. Similarly, Narayan *et al.* [101] found experimentally that there was no systematic change in the anodic polarization behavior of eutectoid steel wires with changes in heat treatment.

Corn *et al.* [102] observed the morphology and relative amounts of attack of a 1045 carbon steel as a function of potential, pH, and aqueous anion. Using a scanning electron microscope (SEM), four modes of attack were distinguished and quantified. These were: carbide attack, matrix attack, general attack, and interface attack. The occurrence of these modes was correlated with the potential, pH, and anion present. For example, in *HCl* solution at pH of 4, the carbides were attacked preferentially at applied potentials of -1000, -500, and -215 mV_{SHE}. At +100 mV_{SHE}, the carbides were severely attacked while the matrix was unaffected. The

reverse was occurring at pH = 10 buffered solution. At -680, -580, and +400 mV_{SHE} the matrix attack was severe while the carbides were unaffected and no attack was observed at -1000 mV_{SHE} after 60 min exposure.

In summary, the anion present drastically changed the dissolution behavior of 1045 carbon steel and varied the mode of preferential attack at the ferrite, carbide, and the ferrite/carbide interface. It is important to note that carbon is thermodynamically unstable in aqueous solution. However, "*the strength of carbon-carbon bond makes the kinetics of the reaction very sluggish.*" This was confirmed by the observation that iron carbide reacted at potentials far below that at which iron became thermodynamically stable [102].

Generally, dissolution of the ferrite is consistent with the potential-pH diagram as shown in Figure 2.11. In the acid range iron will not dissolve significantly at potential lower than -620 mV_{SHE}, corresponding to $[\text{Fe}^{+2}] = 10^{-6}$. As the pH increases above ~9, the oxide becomes more stable and the range of potentials in which passivity occurs increases.

The dissolution of iron carbide is relatively complex, and only speculative discussion is possible. The common understanding has been that iron carbide is cathodic to the steel matrix in aqueous solutions. However, in some environments the carbide phase is attacked more rapidly than the ferrite [102]. Iron carbide was thought to be inert because of the well-known resistance of graphite anodes to attack in many aggressive environments. However, thermodynamic consideration showed that carbon is unstable in aqueous environments at all values of pH and potential [106].

Iron carbide is relatively more reactive than carbon, but the kinetic processes are greatly different. A detailed understanding and determination of these processes still await to be done.

Moreover, the interfacial attack was observed in certain environments and attributed to segregation of minor elements [102]. The rationalization of this behavior needs to be confirmed.

2.2.6 Stress corrosion cracking of eutectoid steel

Generally, steel is subject to SCC and hydrogen embrittlement (when hardened). A common SCC agent is a caustic (e.g. $NaOH$), in which case the attack is often called "caustic embrittlement". Steel also suffers SCC on exposure to nitrates [25], concentrated HNO_3 , dilute HNO_3 containing manganese dioxide, anhydrous ammonia. SCC also occurs in mixtures of CO , CO_2 , and water vapor at elevated temperatures. At high hardnesses (Rockwell C 22 and above) steel also suffers hydrogen assisted cracking in "sour" environments (i.e., media containing H_2S and related products), and in cyanide and thiocyanate solutions.

Gilehrst and Narayan [25] tested different heat treatments of eutectoid wires subjected to a static tensile stress level of $0.95 \sigma_y$ in different environments and polarized to 0.5 V anodically or cathodically with respect to E_{corr} . They recorded the time to failure and observed a wide spread of failure times. Most cathodic polarized samples failed by brittle fracture, while anodic polarization led to failure by "loss of section due to electrochemical thinning." According to their results [25], simple chloride solutions do not readily produce stress corrosion cracks in eutectoid steel, while sulphide was dangerous under all conditions.

Narayan *et al.* [101] performed time to failure (T_f) tests on eutectoid steel wires with different microstructures in 50% $Ca(NO_3)_2$ + 5% NH_4NO_3 solution at 100°C. It was concluded that quenched and tempered wires were generally more susceptible to SCC than the annealed

and isothermally transformed wires. No correlation between the anodic polarization behavior of these wires and their susceptibility to SCC was observed.

2.2.7 Hydrogen embrittlement of eutectoid steel

A critical hydrogen concentration for separation of atomic bonds at internal interfaces exists. Clearly, the threshold hydrogen concentration to break an already stressed atomic bond depends on the type of interface present in the material. Hydrogen diffusion appears to be less in a lamellar microstructure than in the spheroidized microstructure of eutectoid steel [91]. Cold-drawn pearlitic steel has a low hydrogen diffusion rate and high solubility for hydrogen due to great number of hydrogen trapping sites.

The higher interfacial areas between pearlite lamellae are thought to be the main trapping sites in this microstructure. Oriani [132] reported that for intermediate pearlite spacing, the extent of the ferrite-cementite interfacial area was about $10^4 \text{ cm}^2/\text{g}$ for a pearlitic steel of 0.8% carbon. Assuming that hydrogen occupies the octahedral interstitial positions (sites) in the α -Fe lattice. Then, the total number of such sites $N_x = 28 \times 10^{19}$ interfacial sites per cm^3 of steel. For 0.1% C-steel of the same pearlite spacing would have $N_x(\text{interface}) = 3.5 \times 10^{19} \text{ cm}^{-3}$.

The solubility for hydrogen is more likely to increase as more traps exist in the material, while the overall diffusion rate is decreased due to trapping. Typical volume densities of trapping sites in many interfaces were summarized by Hirth [135]. Carbide-matrix interfaces and grain boundaries are the only traps in the spheroidized condition. The interfacial area in the spheroidized condition is smaller than that of the pearlitic steel when the carbide dimension is equal to the thickness of the cementite lamellae [132]. Therefore, spheroidization presents hydrogen a smaller total population of trapping sites. These trapping sites should

saturate faster. Thus, hydrogen effects are more pronounced in the spheroidized steels. However, the amount of hydrogen that is actually accumulated at interfaces is difficult to calculate and still controversial [128]. Part of the controversy regarding hydrogen effects can be attributed to the different test materials studied by the various research groups.

Maier *et al.*[128] observed that hydrogen charging caused a marked reduction in the ductility of a spheroidized low alloy steel (0.89% C, 2.06% Mn, 0.32% Cr). The hydrogen effect on ductility decreased as the temperature was raised. The fracture mode was ductile for both charged and uncharged specimens, and was due to a microvoid coalescence fracture mechanism.

2.2.8 Corrosion fatigue cracking of eutectoid steel

Querales and Byrane [20] studied the effect of TMT on the mechanical properties of eutectoid steel. They found that “the fatigue life of TMT specimens increased linearly with the amount of prior cold rolling.” Cracks in pearlitic steel were found to grow through pearlite colonies, and sometimes parallel to the cementite lamellae. Stage-I fatigue crack propagation was observed at a 45° angle with respect to the surface of the specimen. Stage-II crack propagation was noncrystallographic crack growth normal to the acting stress axis.

In a subsequent work, Kao and Byrne [21] found that near the initiation threshold, the variation of the interlamellar spacing and the presence of a proeutectoid ferrite network showed little effect on the initiation threshold, but in the higher stress intensity region the presence of a proeutectoid ferrite network was definitely deleterious. Sunwoo *et al.*[29] observed that most of the cracks were initiated in the ferrite matrix near the interfaces with the carbide lamellae. They postulated that “*dislocations are generated more easily at the crack*

tip in the soft ferrite matrix than at the ferrite-cementite interfaces, and the dislocations along the interfaces are pile-ups formed during cyclic deformation.”

In a study on electropolished, hour-glass shape specimens of a fully pearlitic, hot-rolled rail steel conforming to AISI 1080, Daeubler and Thompson [22-23] observed microcracks initiating at the surface in an angular range 45° - 60° inclined to the load axis but parallel to the general lamellae orientations. The interfacial microcracks were attributed to “*plastic strain incompatibilities between the soft ferrite and the strong cementite phases due to the applied shear stress.*” As the interlamellar spacing decreased, the incompatibility is reduced which leads to higher resistance against crack initiation. Figure 2.14 shows a schematic depiction of stage I crack parallel to cementite lamellae. They concluded that a microstructure with both a fine prior austenite grain size and fine interlamellar pearlite spacing has better resistance to crack initiation and propagation than that with a coarse condition of one of these features or a coarse combination of both features.

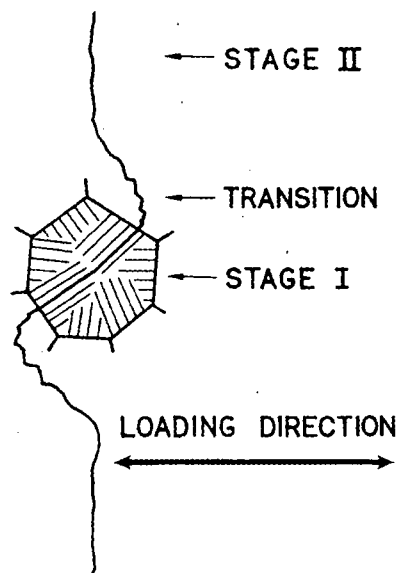


Figure 2.14 schematic depiction of stage-I crack parallel to cementite lamellae [21].

In the case of prestressed concrete wires [14], the most common aggressive environment found is salt water, which is the environment for offshore and seashore structures, and very similar to that of road bridges when de-icing salts are used. Llorca *et al.* [27] studied the effect of stress ratio on fatigue threshold in cold drawn eutectoid steel wires. The fatigue threshold (ΔK_{th}) for these wires was experimentally obtained as the cyclic stress intensity factor for which the crack growth rate was lower than 10^{-11} m/cycle. It was found that ΔK_{th} was independent of the initial defect depth and stress amplitude, and it was given by;

$$\Delta K_{th} = 5.54 (1 - 0.62 R) \quad (2.11)$$

Where ΔK_{th} is expressed in $\text{MPa}\cdot\text{m}^{1/2}$, and R is the stress or load ratio.

Martin *et al.* [24] studied the FCP behavior of prestressing steel wires in artificial seawater (pH = 8.2) at room temperature. They observed that the growth rates of short cracks propagated from surface defects were higher than those of long cracks subjected to the same cyclic stress intensity factor. Husain *et al.* [31] observed that corrosion of eutectoid steel wires in artificial ASTM seawater enhanced fatigue damage. The samples failed after only 40% of the expected life. This damage was believed to be caused by dissolution processes, rather than hydrogen embrittlement. They also reported that the most severe cracking of plain and galvanized wire was observed at a potential of $-650 \text{ mV}_{\text{SCE}}$, corresponding to free corrosion of the ungalvanized wire with no significant indication of any hydrogen embrittlement effect at low potentials.

The independent role of prior austenite grain size, pearlite colony size, and pearlite interlamellar spacing upon FCP rates in AISI 1080 steel was investigated by Gray *et al.* [32]. Testing was in laboratory air and high purity helium, at R values of 0.1 and 0.7. The high ΔK_{th}

values at $R=0.1$ were attributed to crack closure effects. Altering the R ratio to 0.7 was seen to decrease significantly the values of ΔK_{th} . Increasing the grain size produced larger deviation in crack path in a “zigzag” manner, which reduced crack growth leading to the suggestion by Gray *et al.*[32] of an increased crack length traveled per unit crack advance. Several cracks were reported to be running parallel to lamellae of pearlite colonies, and were attributed to dislocations, generated in the ferrite, advancing and piling up against the ferrite/cementite interface. The microstructurally induced variations in FCP and ΔK_{th} were attributed to roughness-induced crack closure effects.

A comparison of crack propagation rates was made between spheroidized, mixed spheroidized/pearlite and coarse pearlitic structures in a 1% C-steel by Richards and Lindley [124]. From Table 5 in their study [124], Fatigue crack growth rates were lowest in the spheroidized condition where no microcleavage mechanism operates. When the amount of microcleavage was enhanced by increasing the proportion and coarseness of lamellar pearlite, the FCP rates increased.

In the reviewed literature, the effect of spheroidization of eutectoid steel on FCP in corrosive environments was not addressed. Most of the fatigue tests reported on this material condition were done in air. Moreover, although this material was investigated under hydrogen charging in the fully pearlitic condition, there is still some uncertainty regarding its effects on the FCP behavior. Thus, it is of fundamental and practical importance to undertake further studies on the effects of spheroidization and cathodic protection on the FCP of eutectoid steels and to compare the behavior with the pearlitic condition.

3 Objective

The main objectives of the current research are as following:

1. To evaluate the corrosion fatigue crack propagation behavior of near-eutectoid steel (AISI 1070) and to investigate the effects of controlled environments on the fatigue behavior at high loading frequency (~100 Hz). Aqueous test environments were distilled water, 3.5% *NaCl* solution, and buffered 3.5% *NaCl* solution. Desiccated air was chosen as the reference testing condition.
2. To compare the fatigue crack propagation behavior of the near-eutectoid steel in the lamellar (pearlitic) microstructure with that of the spheroidized microstructure.
3. To study the effect of cathodic protection and/or hydrogen charging on fatigue cracking of this particular material.
4. To assess the fracture surface topography of specimens tested under different conditions using scanning electron microscopy (SEM).

4 Experimental

4.1 Material

4.1.1 Chemical composition

The material used for the study was commercial near-eutectoid steel bar, conforming to AISI 1070, having 55 X 55 mm cross section. The chemical composition of the material was supplied by AltaSteel [77] and is given in Table 4.1. The AISI 1070 grade has a permissible carbon content range of 0.65 to 0.75 percent, and an allowable manganese spread of from 0.60 to 0.90 percent [78]. Whereas, the AISI 1080 grade has a permissible carbon content range of 0.75 to 0.88 and the same range for the allowable manganese limits.

Table 4.1 Chemical Composition (wt. %)

C	Mn	P	S	Si	Cu	Ni	Cr	Mo	V
0.70	0.75	0.014	0.029	0.24	0.26	0.13	0.19	0.028	0.001
Cb	Ti	Al	Sn	Ca	N	Pb	Zr	Zn	Fe
0.026	0.001	0.002	0.013	0.0017	0.0070	0.001	0.001	0.001	bal.

4.1.2 Heat treatment

The steel bar was received in the hot rolled condition. Part of the investigation was conducted on the as-received material which had a $\geq 90\%$ lamellar pearlite microstructure. The material was also heat-treated to 700°C for 4 hr. to obtain a fully spheroidized microstructure. The abbreviations AR and HT shall be used to denote the as-received and

heat-treated conditions, respectively. Heat treatments of all specimens were done in stainless steel foil bags, which were sealed after purging with argon gas to prevent high temperature oxidation and scale formation.

4.1.3 Metallography

Metallographic specimens were prepared for examination according to the ASTM E 3 standard procedure [84]. Specimens were polished to a 1 μ m surface finish with diamond paste then etched with 2% HNO_3 in ethanol (Nital) to reveal the microstructure. Quantitative metallographic analyses of the microstructures were conducted on the AR and HT material using both optical and scanning electron microscopy (SEM) techniques. In the AR (lamellar) microstructure, the initial interlamellar spacing (S_p), prior austenite grain size (AGS), and pearlite colony size were measured by the linear intercept method covered under ASTM E 112 [110]. The pearlite colonies were recognized from the appearance and orientation of the cementite and ferrite lamellae. The smallest interlamellar distances were measured to represent lamellae aligned at 90° to the plane of observation. Measurement of S_p on SEM micrographs followed the practice of other researchers [17-19, 112]. The average distance between cementite particles (S_o) in the spheroidized microstructure was determined in the same way.

4.2 Specimen design and preparation

4.2.1 Tensile specimens

Substandard size, threaded-end specimens were machined from the AR material. Care was exercised in the preparation of specimens to be close to the ASTM E 8M standard procedure

[79]. The half inch diameter standard size was avoided in order to conserve material for the fatigue testing. Test specimens were oriented such that the longitudinal direction of each was parallel to the rolling direction. Figure 4.1 shows the geometry and dimensions of the tensile specimens. Three specimens were in the HT condition, as described previously (see 4.1.2), while another four were tested in the AR condition. After machining and heat treatment, a gage length of ~20 mm was marked on the specimens.

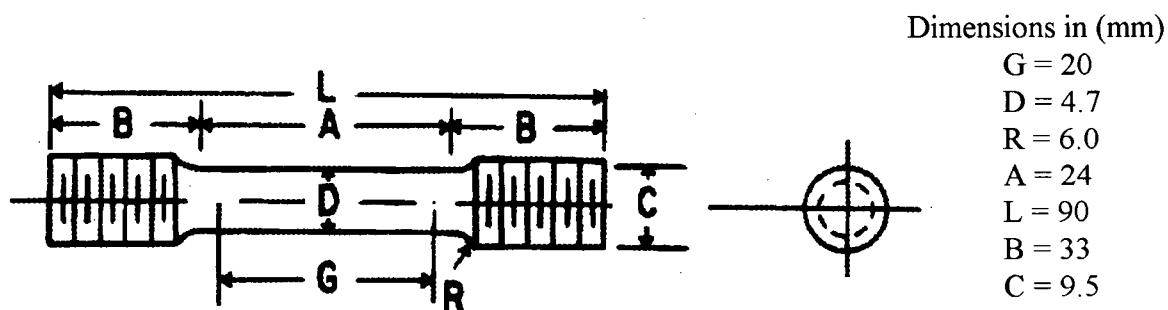


Figure 4.1 Tensile test specimen

4.2.2 Electrochemical test specimens

Corrosion specimens were sectioned as ~15 mm cubes from AR and HT material. A nickel connection wire was spot welded to the rear of each specimen, and covered with a tightly fitting transparent plastic tube. Specimens were then mounted in a cold-curing epoxy resin to expose a working electrode area of ~1.5 cm². Figure 4.2 shows a schematic diagram of the electrochemical specimens. The specimens were mechanically ground to 600 grit silicon carbide (*SiC*) paper followed by polishing on diamond (5 μ m and 1 μ m) wheels. Polishing of the specimens was carried out in order to minimize the effect of variations in surface roughness. The exposed edges between the epoxy and the steel were masked with cellulose acetate lacquer to prevent crevice corrosion effects.

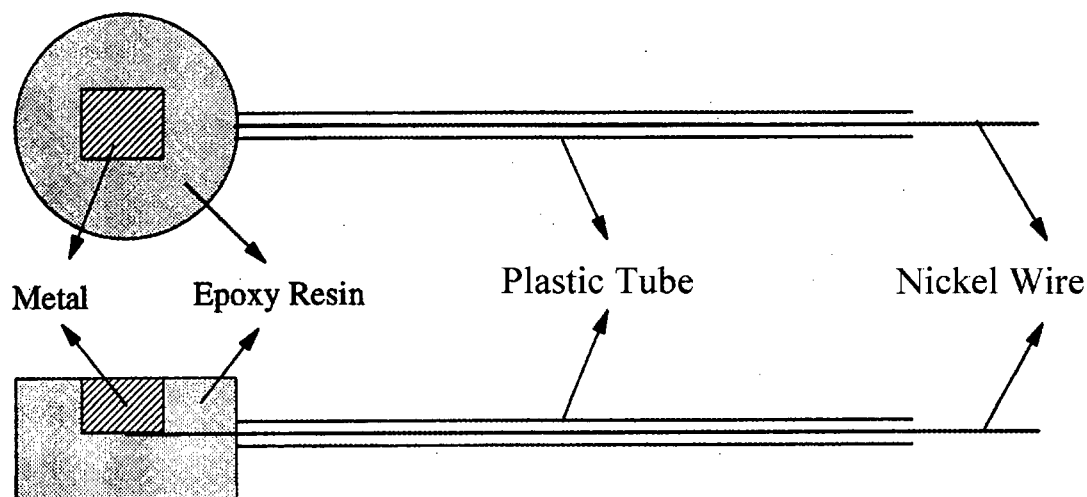
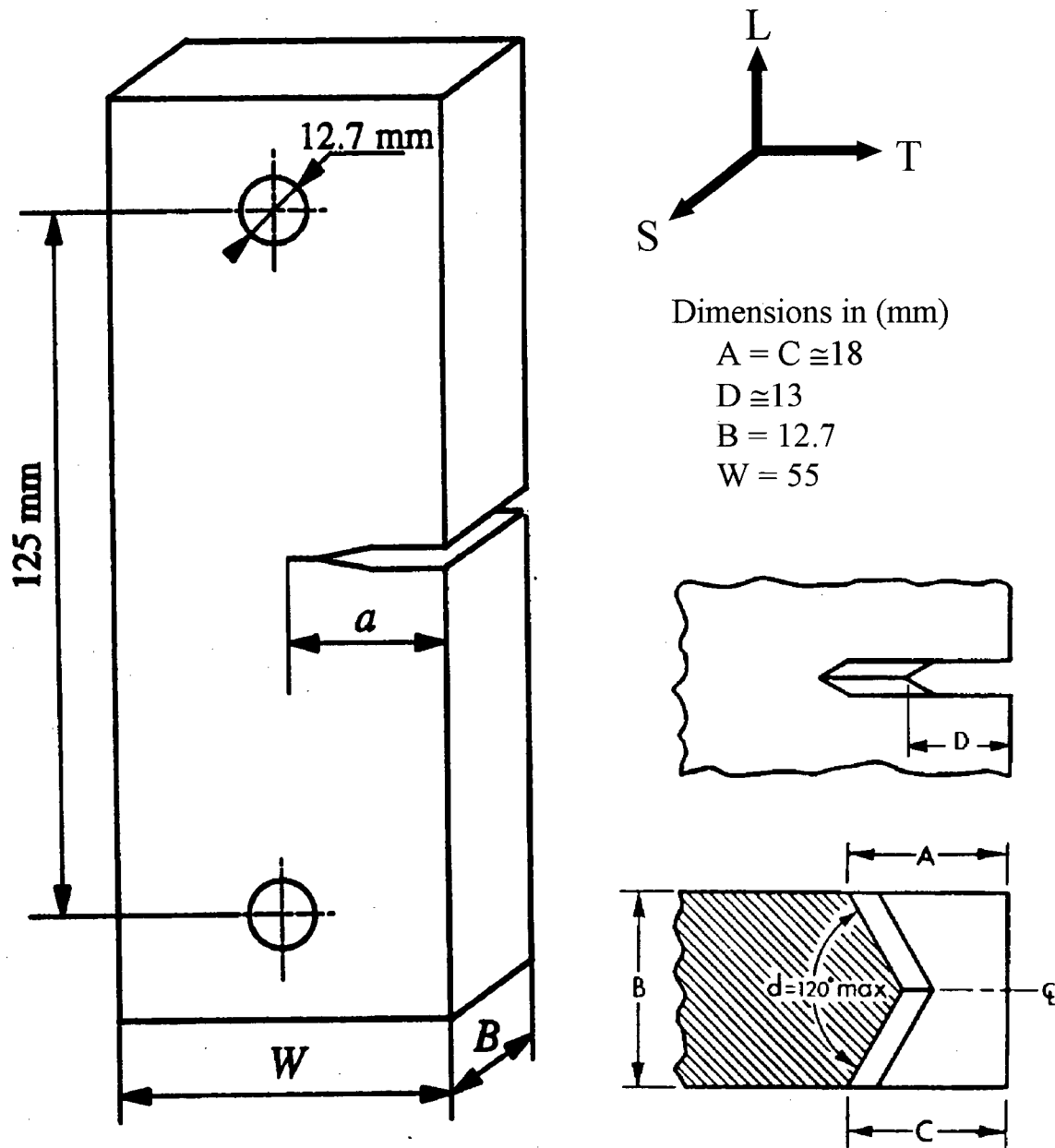


Figure 4.2 The electrochemical test specimens

4.2.3 Fatigue specimens

Pin loaded, single edge notched (SEN) specimens with a L-T orientation cracking plane and direction as defined by ASTM E399-90 [80] were used for high frequency fatigue testing at ~ 97 Hz. Figure 4.3 shows the geometry and dimensions of the SEN specimens, which are dimensionally identical to a previous specimen design in a similar work [60, 61]. The specimens were machined from the AR material and a chevron notch was introduced as illustrated in Figure 4.3b. The next step was grinding of the two side surfaces to 600-grit *SiC*, followed by mechanical polishing with diamond paste ($5\ \mu\text{m}$ and $1\ \mu\text{m}$) wheels. Afterwards, fiducial lines were scribed on the specimen surface to facilitate crack length measurements. The scribed faces were coated with a transparent nitrocellulose lacquer to prevent surface corrosion from interfering with observation of crack growth.



(a) Specimen design.

(b) Detail of chevron notch.

Figure 4.3 Geometry of the single edge notched (SEN) specimen.

Load was applied along the center line of the specimen through the pin hole. The K -calibration equations for opening mode stress intensity factor for the SEN specimen configuration are given by Equations (4.1) to (4.4) [59, 69].

$$\Delta K = K_{\max} - K_{\min} = (1 - R)K_{\max} \quad (4.1)$$

$$K = \frac{P(a\pi)^{1/2} f(a/W)}{WB} \quad (4.2)$$

$$f(a/W) = \left(\frac{\tan Q}{Q} \right)^{1/2} \frac{\{0.752 + 2.02(a/W) + 0.37(1 - \sin Q)^3\}}{\cos Q} \quad (4.3)$$

$$Q = \left(\frac{a\pi}{2W} \right) \quad (4.4)$$

where P is the load, W is the specimen width, a is the crack length and B is the specimen thickness.

4.3 Test environment selection

The reference environment was chosen to be the desiccated air. It was obtained by placing fresh silica gel desiccant in an acrylic cell mounted around the SEN specimen and closing the top of the cell with a flexible rubber membrane. Other test environments were: distilled water, 3.5% $NaCl$ solution, and buffered 3.5% $NaCl$ solution (pH = 10.5). Aqueous solutions were prepared from distilled water and reagent grade chemicals. Table 4.2 lists the test environments along with the electrochemical potential measured with respect to a saturated calomel reference electrode (SCE). Compositions of electrolytes were presented in the molar (M, mol/L) concentrations of added chemicals, together with the resulting pH. Experiments in the $NaCl$ solutions were conducted with and without cathodic protection.

Table 4.2 Fatigue test environments and testing conditions.

Material Condition	Environment	pH	Test potential (V_{SCE})*	Frequency f , (Hz)
As Received (AR)	Desiccated air	-	-	~95
	Distilled water	6.50	E_{corr} , (not measured)	~96
	0.6 M NaCl (3.5% NaCl)	6.0	E_{corr} , -0.581 _ -0.605	~96
	0.6 M NaCl (cathodically polarized)	6.0	$E = - 1.000$	~94
	0.6 M NaCl + 0.075 M $Na_2B_4O_7$ + 0.13 M NaOH (buffered 3.5% NaCl)	10.5	E_{corr} , -0.440 _ -0.504	~98
	0.6 M NaCl + 0.075 M $Na_2B_4O_7$ + 0.13 M NaOH (cathodically polarized)	10.5	$E = - 1.266$	~97
Heat Treated (HT)	Desiccated air	-	-	~97
	0.6 M NaCl (3.5% NaCl)	6.0	E_{corr} , -0.542 _ -0.641	~97
	0.6 M NaCl (cathodically polarized)	6.0	$E = - 1.000$	~97
	0.6 M NaCl + 0.075 M $Na_2B_4O_7$ + 0.13 M NaOH (cathodically polarized)	10.5	$E = - 1.266$	~98

* Potential range from beginning to end of test: E_{corr} is the freely corroding potential.

4.4 Test setup and Procedures

4.4.1 Tensile and hardness testing

Monotonic tensile tests were carried out to provide the basic information on the mechanical properties of the material in the AR and HT conditions. A universal testing machine (Instron)

was used to perform the tests with the guidance of ASTM E 8M standard procedure [79]. The load-weighing system was calibrated and 5000 lb load scale was selected. The testing crosshead speed was constant at 0.25 mm/min and chart speed of the load recorder was set at 3 cm/min. The testing was done in laboratory air at ambient temperature ($\sim 22^{\circ}\text{C}$). The yield stress (σ_y) was determined at the 0.2% strain offset.

The standard Vickers hardness test was utilized to characterize the material hardness and compare the two microstructure conditions. A micro hardness tester (MICROMET® 3) was used to obtain the Vickers hardness numbers (HV). Relevant ASTM standard procedures [84-86] were observed in preparing the samples and conducting the test. A one kilogram test load was selected and the load holding time was set at 20 sec. An average HV value of 15 measurements was obtained for each microstructure.

4.4.2 Potentiodynamic polarization tests

Potentiodynamic polarization tests were conducted in the aqueous chloride solutions. The ASTM G5 [81] standard method was adopted in these tests. The testing was conducted using an EG&G Princeton Applied Research model 350A potentiostat, a standard corrosion cell containing the working electrode, platinum mesh counter electrode and a saturated calomel reference electrode (SCE) mounted in a separate compartment. Specimens were cleaned and degreased in acetone followed by rinsing in distilled water prior to testing. About one liter of electrolyte was used for each test and solutions were prepared as mentioned earlier (see 4.3). The working electrode was centrally located in the cell facing the counter electrode. Solutions were deaerated by N_2 gas purging before and during one series of tests. Another set of tests

was also conducted in the aerated condition. Table 4.3 shows the parameters and conditions of these tests. Care was taken to make good electrical connection between the electrodes and the potentiostat. Figure 4.4 shows the experimental setup for the electrochemical testing. Electrode potentials were measured with respect to the SCE via a bridged Luggin probe terminating ~2 mm from the specimen. The bridge contained the working solution and the Luggin probe was maneuverable and allowed probe tip placement near (~2 mm) the working electrode surface. Small potential differences due to liquid junction between the reference electrode and the salt bridge were ignored.

Table 4.3 Potentiodynamic anodic polarization test parameters

Electrolyte composition	3.5% NaCl	buffered 3.5% NaCl
Potential Ranges	E_{corr} to 1.2 V _{SCE} -1.0 to 1.2 V _{SCE}	E_{corr} to 1.2 V _{SCE} -1.266 to 1.2 V _{SCE}
Temperature	24 ± 1°C	
Scan rate	1 mV/sec	
Surface finish	1 μm diamond	

As indicated in Table 4.3, potential scanning was first done starting from E_{corr} for two tests. In the other tests, the specimens were cathodically polarized before initiating the potential scan in the anodic direction. A record of the potential and current density was plotted continuously by the programmable potentiostat on semi-logarithmic scale. The potentiodynamic measurements were also transferred to a personal computer for further analysis and presentation.

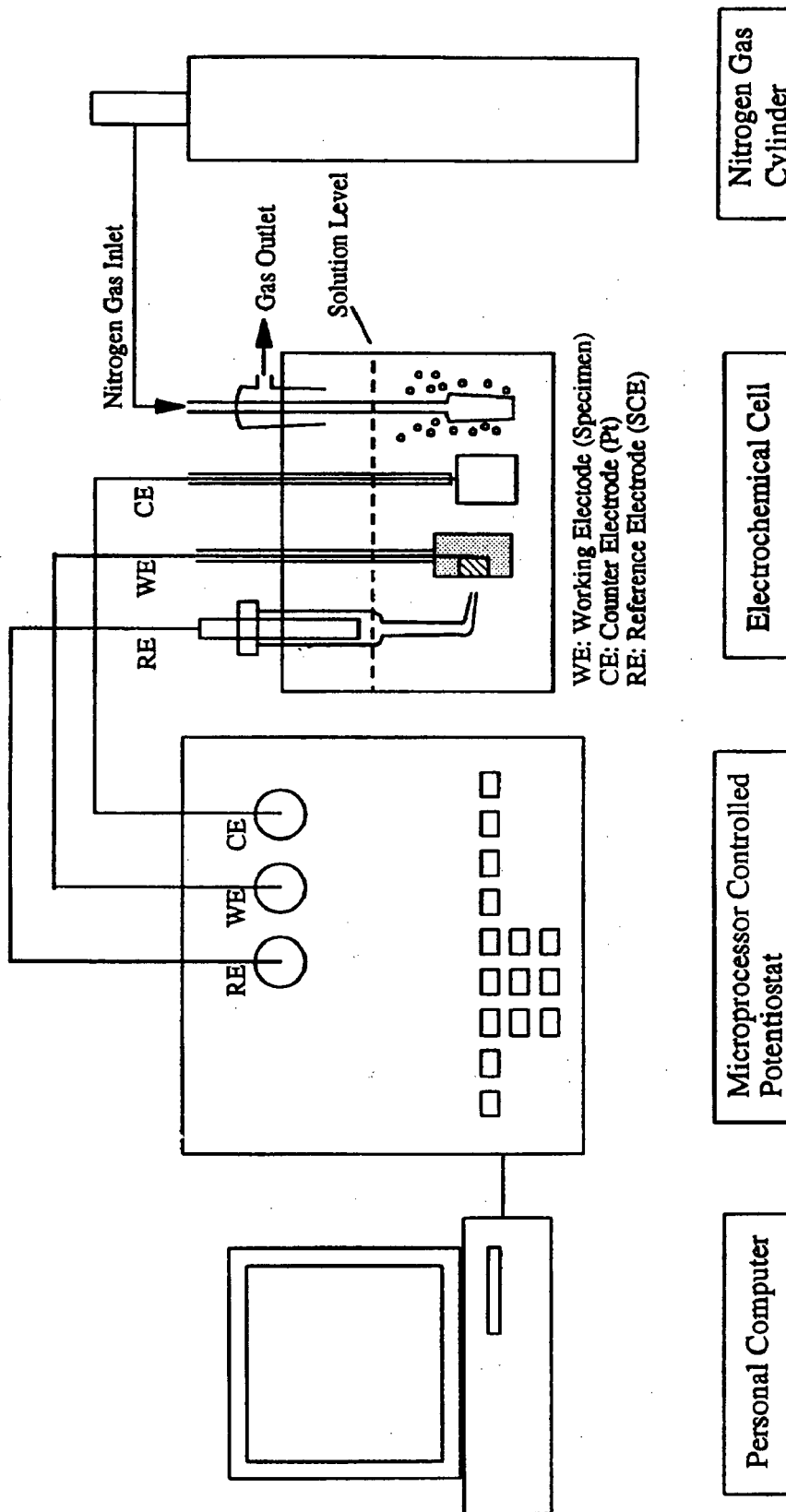


Figure 4.4 The experimental setup for the electrochemical testing.

4.4.3 Fatigue testing

Fatigue experiments were performed on an electro-magnetic resonant fatigue machine (Instron model 1603) under sine wave loading. This machine was utilized as the primary investigating tool in the current study. The applied loads were selected via a 100 KN load cell and a digital control console. The cyclic frequency varied slightly depending on the stiffness of the tested specimen and the applied cyclic load. The fatigue frequencies encountered are listed in Table 4.2, and were 96 ± 2 Hz. Such high cyclic frequency testing was found to maintain good mixing between the crack solution and bulk solution via the rapid movement and pumping action of opposing crack surfaces [58-60]. The investigation was carried out following the general provisions of standard test method ASTM E 647 [82]. Crack length was measured visually by an internally illuminated traveling microscope with a micrometer stage resolution of 10 μm . With careful observation of the crack tip, it was possible to detect early crack advancements of 10 μm . All fatigue testing was done at ambient temperature ($\sim 22^\circ\text{C}$).

The initial machined crack was sharpened by fatigue precracking in desiccated air until it was ~ 22 mm. Precracking was conducted under load shedding conditions, as following:

1. Start with initial $\Delta K \cong 10 \text{ MPa}\cdot\text{m}^{1/2}$, and R ratio of 0.1.
2. Decrease ΔK gradually and increase R from 0.1 to 0.5.
3. Fix R ratio at 0.5.
4. Continue incremental decreases of ΔK by 10%.
5. Monitor the crack propagation until no crack growth could be detected after 1×10^6 cycles.
6. Stop precracking. At this point, the crack length increase was ~ 5 mm.

The incremental load reductions were used to minimize crack closure effects due to load shedding. Subsequently, the test was resumed in the selected environment. For fatigue tests conducted in desiccated air, the test was simply continued without changing the precracking environment. Otherwise, the silica gel was removed and test solution was poured into the cell keeping the top open to the atmosphere. The environment was contained in a transparent acrylic cell around midsection of the cracked specimen without affecting loading, or crack monitoring. To prevent leakage of the test solution, the cell was sealed to the specimen by silicone rubber cement. The transparent test chamber enabled visual monitoring of the crack growth on one side of the specimen. This was deemed satisfactory since post-test examination of the fracture surfaces showed that the crack front profile was straight and unbowed and crack growth occurred equally at the mid-thickness and on both sides of the specimens. Figure 4.5 shows the experimental setup, as utilized previously for tests on Al-alloy 8090 [60, 61]. Other techniques for crack growth rate determination based upon the measurement of the compliance of the specimen yields good results at high crack growth rates ($> 10^{-6}$ mm/cycle). Compliance techniques are not appropriate for lower rates [27] and require compliant specimens (the SEN specimen is very stiff elastically).

The subsequent fatigue crack growth testing was conducted under rising ΔK conditions, which included the following steps:

1. Use a constant R ratio of 0.5 to minimize crack closure effects.
2. The initial ΔK is 10% lower than the final value at the end of precracking.
3. Monitor the crack for any detectable growth within 1×10^6 to 2×10^6 cycles.
4. Increase ΔK by small increments ($\leq 10\%$).

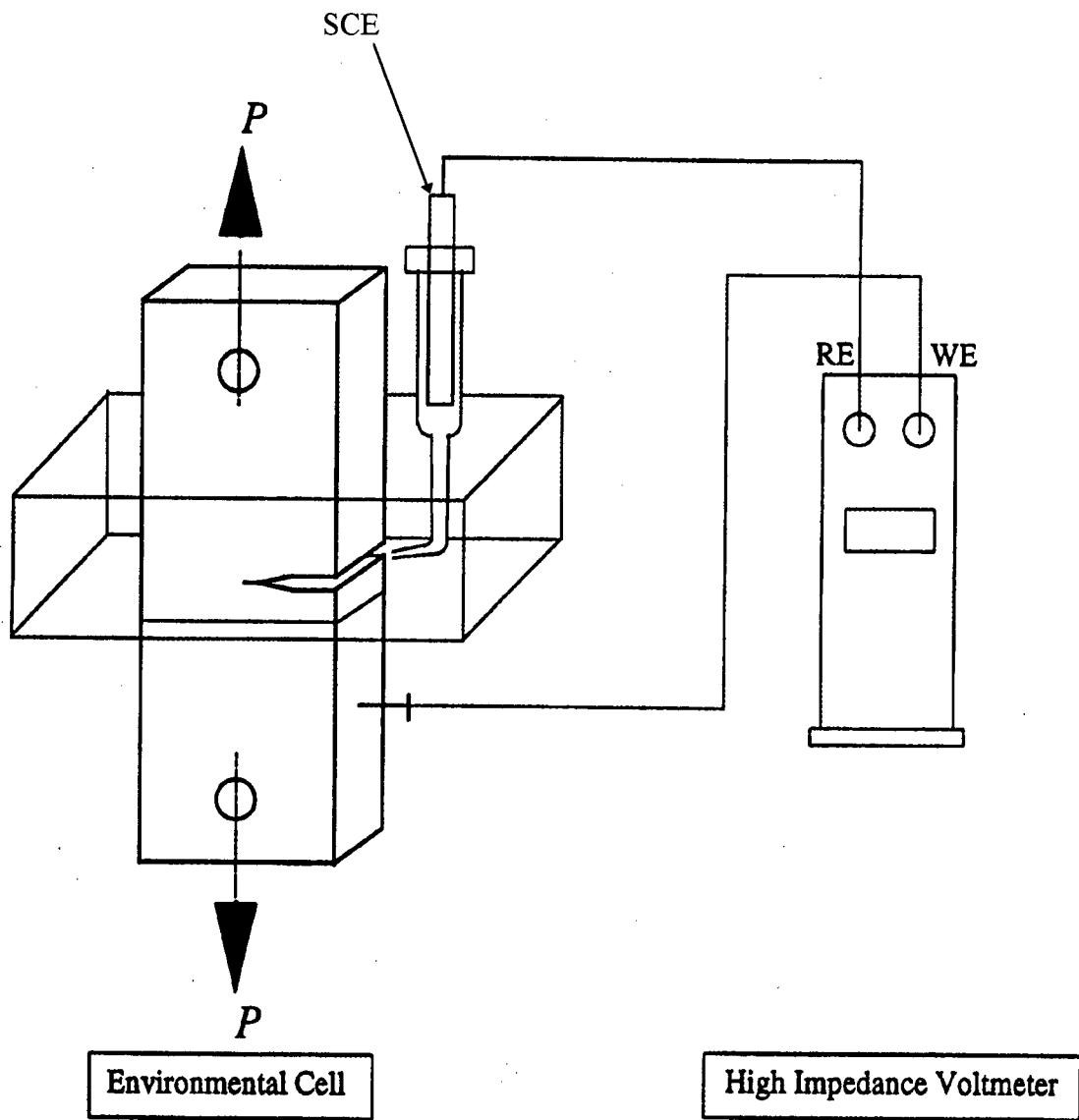


Figure 4.5 The experimental setup of fatigue testing.

5. Monitor crack propagation until growth rate of 1×10^{-8} mm/cycle is detected (i.e. $10 \mu\text{m}/1 \times 10^6$ cycles). The onset of cracking corresponds to ΔK_{th} .
6. Let P_{max} and P_{min} remain constant and allow ΔK to rise with increasing crack length.
7. If crack arrest occurred for $\geq 2 \times 10^6$ cycles, then repeat steps 4-6. If not, go to 8.
8. Record crack length (a) as a function of number of elapsed cycles (N).
9. Obtain the average crack growth rate per cycle, da/dN , by the secant method described in ASTM E 647 [82].
10. Calculate the corresponding nominal (apparent) ΔK values for each crack length via Equations (4.1) to (4.4). The average value of the crack length during monitored crack growth increments over ΔN cycles was used to calculate ΔK .

Most of the tests were terminated at final crack length ≤ 36 mm, which correspond to $\Delta K \leq 17 \text{ MPa} \cdot \text{m}^{1/2}$. The specimens were fully broken in tension to expose the fracture surfaces for the subsequent examinations.

Some fatigue experiments were conducted with polarization potentials imposed to simulate service conditions of cathodically protected components under corrosive environments. The cell was mounted vertically containing the test solution, and two platinum counter electrodes were positioned at the front and back face of the edge crack to complete the polarizing circuit. A potentiostat (ECO Model 549) was used to polarize the specimen cathodically with respect to the free corrosion potential (E_{corr}). The cathodic polarization potentials were pre-selected at $-1.0 V_{SCE}$ and $-1.266 V_{SCE}$ in 3.5% *NaCl* and buffered 3.5% *NaCl*, respectively. At both polarized potentials, the hydrogen overvoltage ($E_{applied} - E_{H^+/H_2}$) was the same (~ 403 mV).

Environment composition of the bulk solution was kept stable throughout testing by periodic replacement of the solution and mixing caused by the opening and closing crack faces during fatigue. The pH of the 3.5% *NaCl* was in the range of 5.5 to 6.0, while the pH of the buffered 3.5% *NaCl* was almost constant at 10.5. The electrochemical potential was monitored under freely corroding and cathodically polarized conditions in all saline solutions. The potential was measured against a SCE reference electrode, as shown in Figure 4.5. The SCE was immersed in the test electrolyte (*NaCl*) in a separate compartment with a bridged Luggin probe ending ~2 mm from the front face of the edge crack. Potentials may be referenced to the standard hydrogen electrode scale (SHE) via the conversion:

$$V_{\text{SHE}} = V_{\text{SCE}} + 0.242 \text{ V.} \quad (4.5)$$

4.4.4 Fractographic study

Crack fractography was examined with a Hitachi S-2300 type scanning electron microscope (SEM), using secondary imaging and 15-20 KeV excitation. A hardened cellulose acetate film, initially softened in acetone, was pressed onto the surface to protect the fracture surface during sectioning for fractographic examination. Broken fatigue specimens were sectioned at ~15 mm below and parallel to the cracking plane, and stored in a desiccator until required. The fractographic features of the fatigue specimens tested in saline solutions were improved by ultrasonic cleaning in an inhibited acid solution to remove traces of corrosion products. The solution consisted of 3 ml conc. *HCl* + 4 ml of a 35% aqueous solution of 2 butyne-1, 4 diol + 50 ml *H₂O* [137]. SEM examinations were conducted before and after the removal of the corrosion products. Each specimen was mounted on a micrometer stage in the SEM, and the chevron tip was selected as a reference point for correlation of the micrograph with crack

length. Fracture surfaces were surveyed in terms of changes in crack length, ΔK , and the corresponding da/dN . SEM stereo images were also obtained [137].

5 Results

5.1 Material characterization

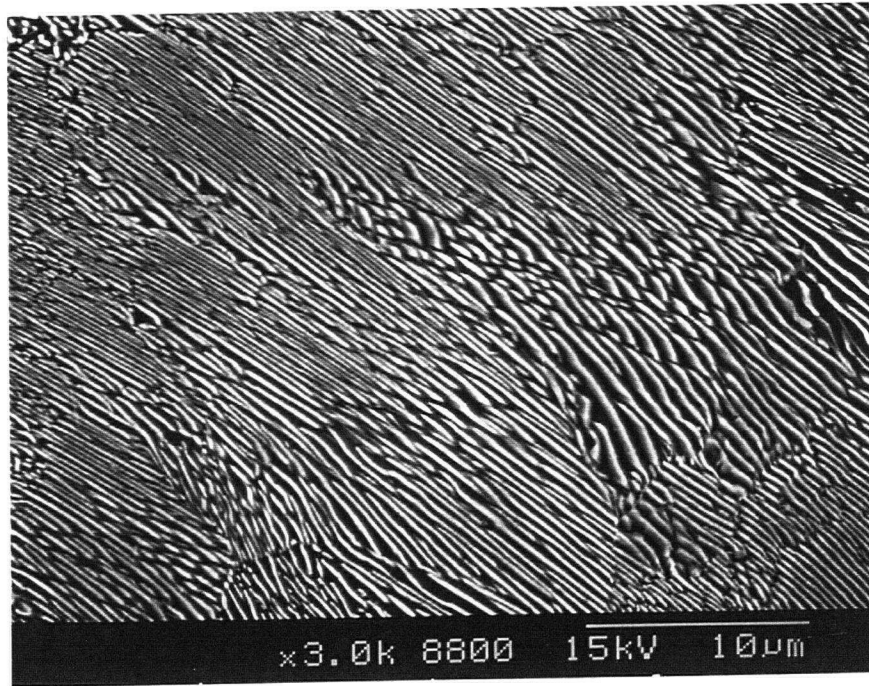
5.1.1 Microstructure

The microstructures of the AR and HT conditions are illustrated in Figures 5.1 and 5.2, respectively. The average value of the minimum interlamellar distances (S_p) observed in several locations was around 0.18 μm and the pearlite colony size was ~ 20 μm in diameter. The proeutectoid grain boundary ferrite network was visible, but very small compared to the pearlite colonies.

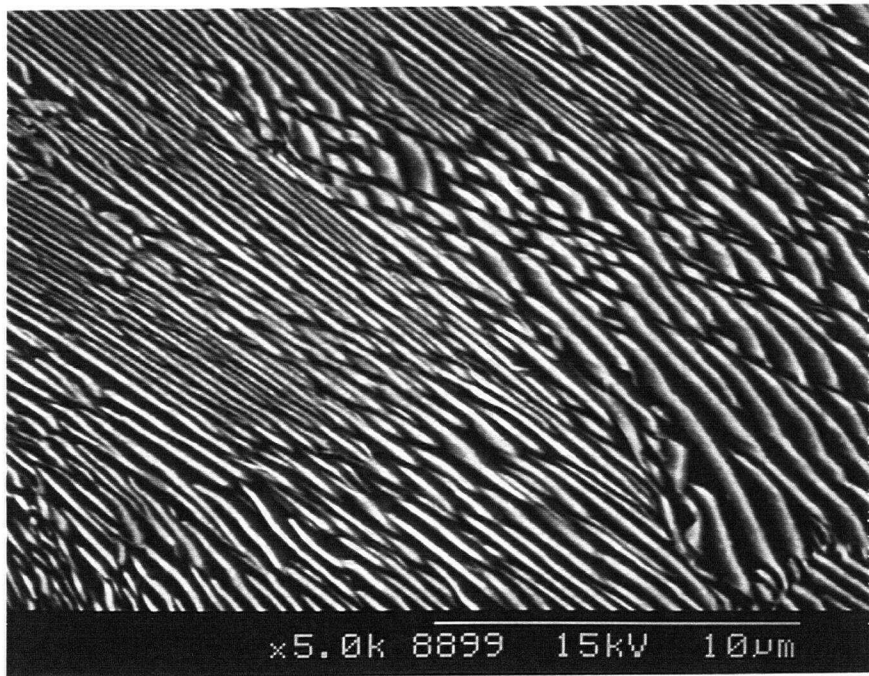
Spheroidization produced a microstructure consists of finely distributed spheroidal cementite particles in a ferrite matrix. During the initial stages of spheroidization, lamellar pearlite degenerates into cylindrical carbide particles, which subsequently shorten and become more spherical. Because of the random dispersion of the carbide particles, inter-particle separation (S_o) was only an approximate measure and it was in the order of 1.6 μm . The cementite particle diameters were ~ 0.5 μm or finer in size. In both conditions, the prior austenite grain size was approximately 55 μm .

5.1.2 Mechanical properties

The actual and nominal mechanical properties [78] of the material are summarized in Table 5.1. The actual properties of the material were experimentally determined as described previously. Standard hardness conversion tables [83] were used to obtain comparable values of different hardness scales.

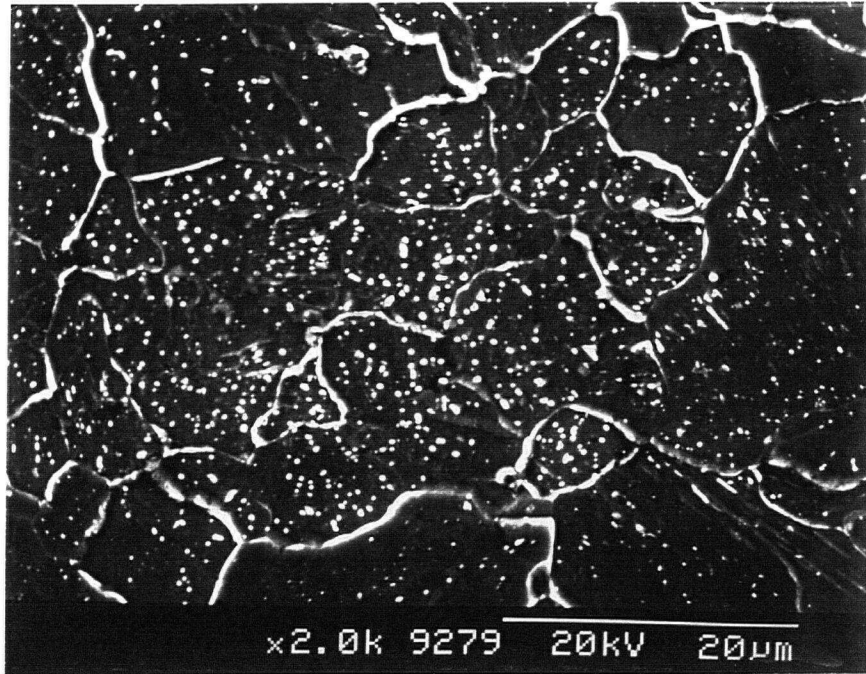


(a)

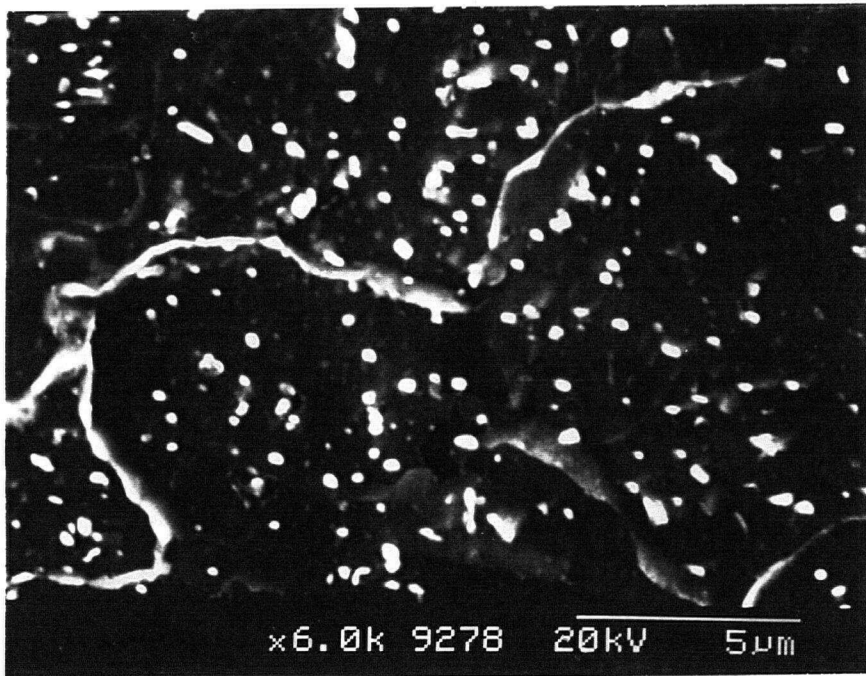


(b)

Figure 5.1 Microstructure of the as received material (lamellar). (a) at X3000 mag., (b) at X5000 mag.



(a)



(b)

Figure 5.2 Microstructure of the heat-treated material (fully spheroidized). (a) at X2000 mag., (b) at X6000 mag.

The measured properties are in agreement with the reported data in the literature [18-20]. Long-time exposure to temperatures below A_1 was expected to cause carbide lamellae to spheroidize and coarsen, resulting in a weaker structure [28]. However, the higher ductility of this microstructure renders it to have higher toughness. An approximate K_{IC} value was determined from two specimens of the fatigue tests in each condition by noting the load at which catastrophic crack propagation occurred in the SEN specimen.

Table 5.1 Mechanical properties

Condition	$\sigma_{y(0.2\%)}$ MPa	σ_{UTS} MPa	ϵ %	RA %	Hardness			K_{IC} MPa.m ^{1/2}
					HB	HV	HR	
Nominal (hot rolled)*	534.4	889.5	15	—	267	~279	~27 C	~48.9
As received (actual)	~541	~948	~17	26.6	~253	~266	~25 C	~44
Heat-treated (actual)	~440	~756	~22	44.5	~159	~159	~83 B	~57

* Data adapted from Metals Handbook [78].

5.2 Electrochemical behavior

The anodic potentiodynamic polarization behaviours of the lamellar (AR) and spheroidized (HT) microstructures in buffered (pH=10.5) and unbuffered (pH=6.0) chloride solutions are shown in Figures 5.3 to 5.5. Passivity and active corrosion were observed in the buffered and unbuffered solutions, respectively. The figures will now be discussed separately.

Figure 5.3 is concerned with the buffered 3.5% NaCl solution, and shows the effect of heat treatment compared to the AR material, starting the scan with E_{corr} . Passivation behavior (low i) was observed over a range of potential due to the formation of protective oxide films. The

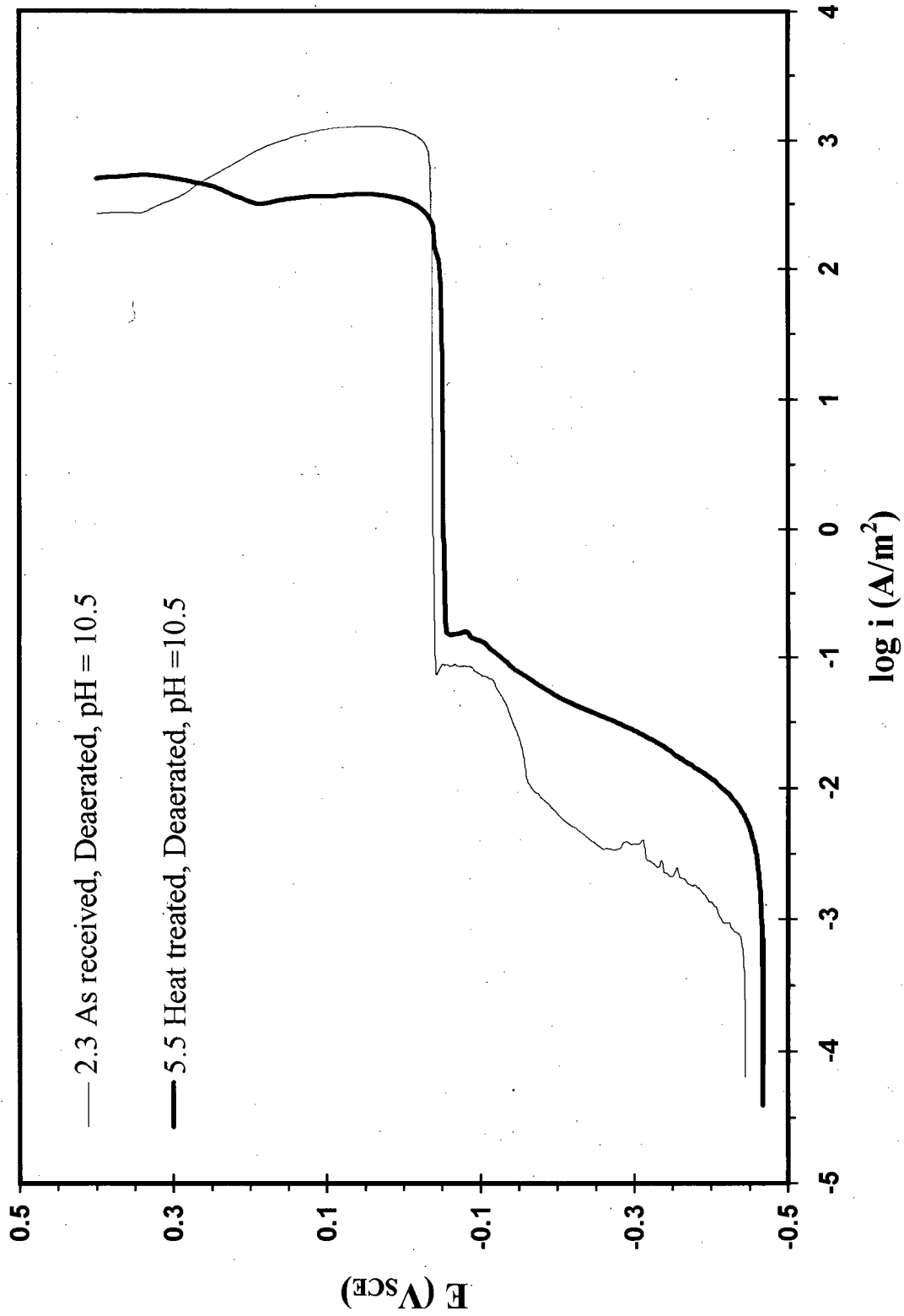


Figure 5.3 Anodic potentiodynamic polarization behavior of AISI 1070 steel starting anodic scan from E_{corr} .

breakdown of passivation (pronounced increase in i) was similar in both conditions and occurred by pitting at a potential (E_{pit}) of ~ 0.05 V_{SCE}. The shape of the polarization curve was not significantly altered by the heat treatment.

The anodic polarization behavior of the AR and HT material in the deaerated, buffered and unbuffered solutions is shown in Figure 5.4, when the scan commences from a relatively negative potential below E_{corr} . The differences in the behavior of the material in the buffered and unbuffered 3.5% NaCl are obvious, i.e., passivation was not observed in the unbuffered solution.

Figure 5.5 shows the behavior of the AR and HT material in the aerated condition which simulates the actual fatigue testing conditions. Again, the dramatic effect of the solution pH on passivity is evident. The freely corroding potentials of both AR and HT condition of the material in buffered and unbuffered saline solutions are listed in Table 5.2.

Table 5.2 Freely corroding potentials at $\sim 24^\circ\text{C}$.

Test condition	E_{corr} (V _{SCE})			
	As received (AR)		Heat treated (HT)	
	pH = 6.0	pH = 10.5	pH = 6.0	pH = 10.5
Starting with E_{corr} *		-0.444		-0.467
Deaerated **	-0.741	-0.920	-0.701	-0.975
Aerated **	-0.501	-0.508	-0.582	-0.484

* Test under deaerated conditions. ** E_{corr} \equiv more correctly the open circuit potential.

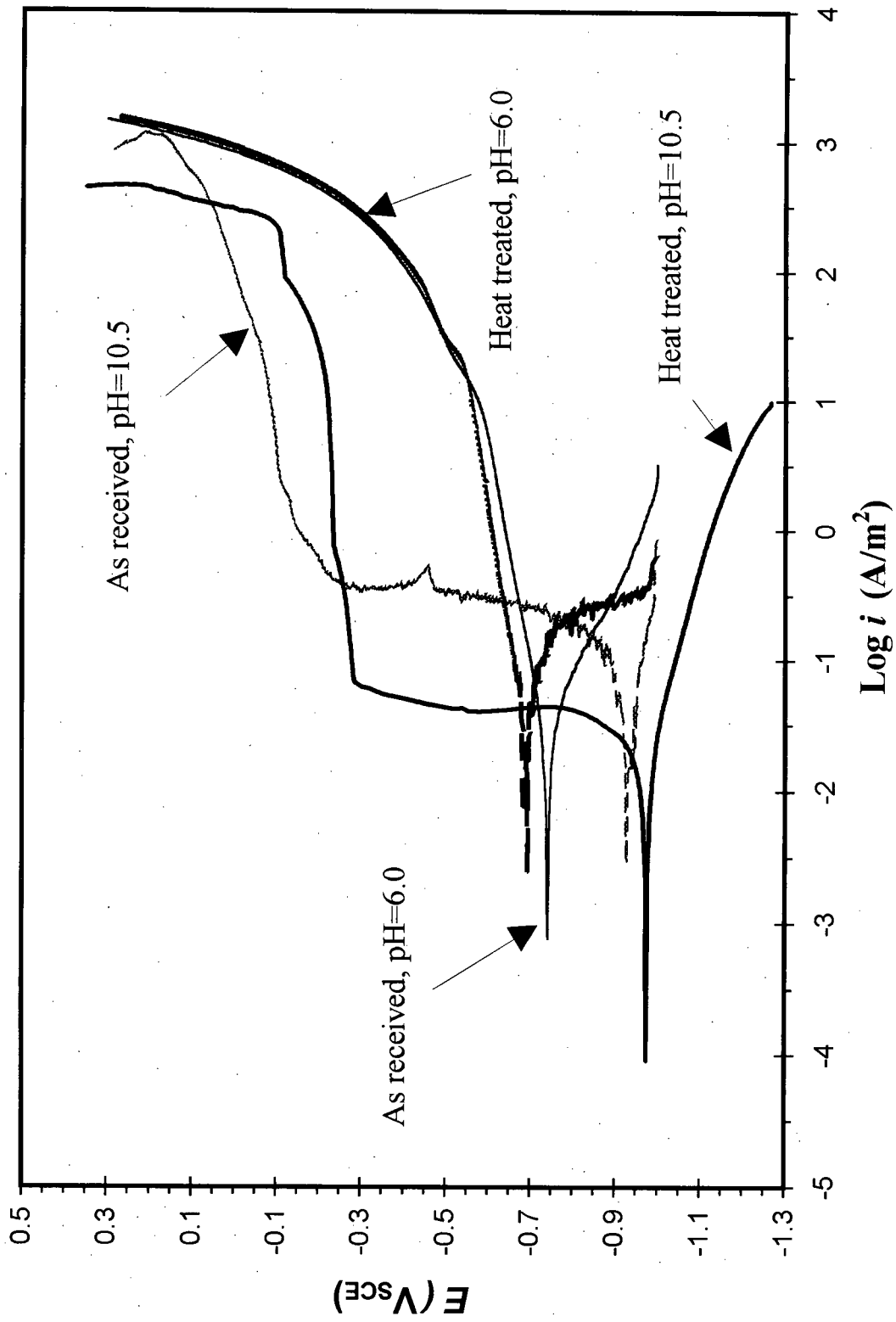


Figure 5.4 Anodic potentiodynamic polarization behavior of AISI 1070 steel (Deaerated condition).

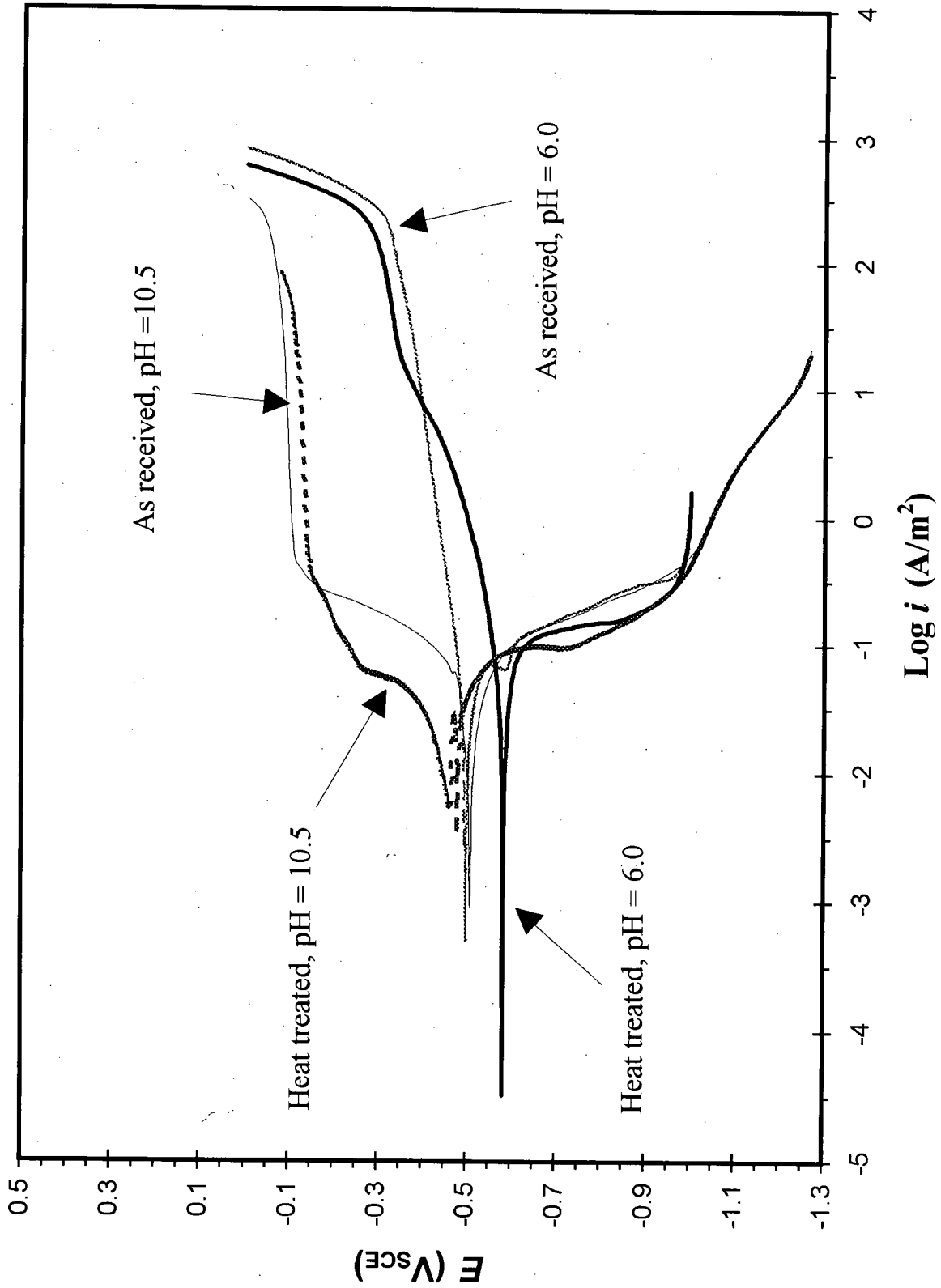


Figure 5.5 Anodic potentiodynamic Polarization behavior of AISI 1070 steel (aerated condition).

5.3 Fatigue crack propagation behavior

5.3.1 As received condition

Crack propagation behaviours of the as-received steel in the chloride solutions, distilled water and desiccated air at ~ 95 Hz loading frequency are shown in Figures 5.6 to 5.10. The fatigue data for related environments are plotted together as linear (ΔK) vs. $\log(da/dN)$ curves to emphasize the effect of these environments on the crack propagation rate. Then, for comparison purposes, all testing environments are presented in a conventional manner as $\log(\Delta K)$ vs. $\log(da/dN)$ in Figure 5.10. Behavior in desiccated air is included in all the figures for reference. Cyclic crack growth rates (da/dN) increased with rising ΔK in all environments. The threshold of cyclic stress intensity (ΔK_{th}) decreased as the corrosiveness of the environment increased. All fatigue cracks propagated in the original crack plane and retained a straight crack front. The typical stage-II fatigue behavior was reproducible in most of the tests and obeyed a power law relationship, $da/dN \propto (\Delta K)^m$, with $m \cong 3$ (see Figure 5.10). Some specimens exhibited large crack retardation over a range of ΔK , as in Figures 5.8 and 5.9. Crack propagation rates were lower in the aqueous environments relative to desiccated air due to corrosion product-induced crack closure. It should be noted that corrosion products were produced inside the crack even under cathodically applied potential, because ohmic resistance effects (iR) inside cracks prevent uniform potential distribution over the crack surfaces [136].

As can be seen from Figure 5.7, fatigue crack growth rates measured from two specimens tested under the same conditions (Test 1 and Test 2) showed good reproducibility. In Figure 5.8, retardation was observed at $da/dN \leq 1 \times 10^{-6}$ mm/cycle and $\Delta K \approx 7$ MPa.m^{1/2} in the near

neutral *NaCl* solution polarized to $-1.0 V_{SCE}$. A similar effect was observed in Figure 5.9 at $\Delta K \approx 5 \text{ MPa}\cdot\text{m}^{1/2}$ in the buffered solution without cathodic protection. However, the freely corroding fatigue test in the near neutral solution exhibited the lowest ΔK_{th} and was the most difficult test to completion, because of a combination of low crack propagation rates and difficulty in monitoring the crack tip position due to corrosion product formation on the surface and in the solution.

Cyclic threshold intensities (ΔK_{th}) for different testing conditions were obtained from the data used to plot Figures 5.6 to 5.9 and are listed in Table 5.3 with the corresponding da/dN values. All the experimental ΔK_{th} values corresponded with crack growth rates of $< 6 \times 10^{-8}$ mm/cycle.

Table 5.3 Threshold stress intensities for fatigue tests (AR condition).

Environment	Test potential (V_{SCE})*	ΔK_{th} $\text{MPa}\cdot\text{m}^{1/2}$	da/dN mm/cycle
Desiccated air	—	~4.3	3.9×10^{-8}
Distilled water	E_{corr} , (not measured)	~4.2	5.8×10^{-8}
3.5% <i>NaCl</i>	E_{corr} , -0.581 _ -0.605	~2.1	1.4×10^{-8}
3.5% <i>NaCl</i>	$E = -1.000$	~3.3	1.0×10^{-8}
Buffered 3.5% <i>NaCl</i>	E_{corr} , -0.440 _ -0.504	~3.1	8.9×10^{-9}
Buffered 3.5% <i>NaCl</i>	$E = -1.266$	~3.9	9.0×10^{-9}

* Potential range from beginning to end of test.

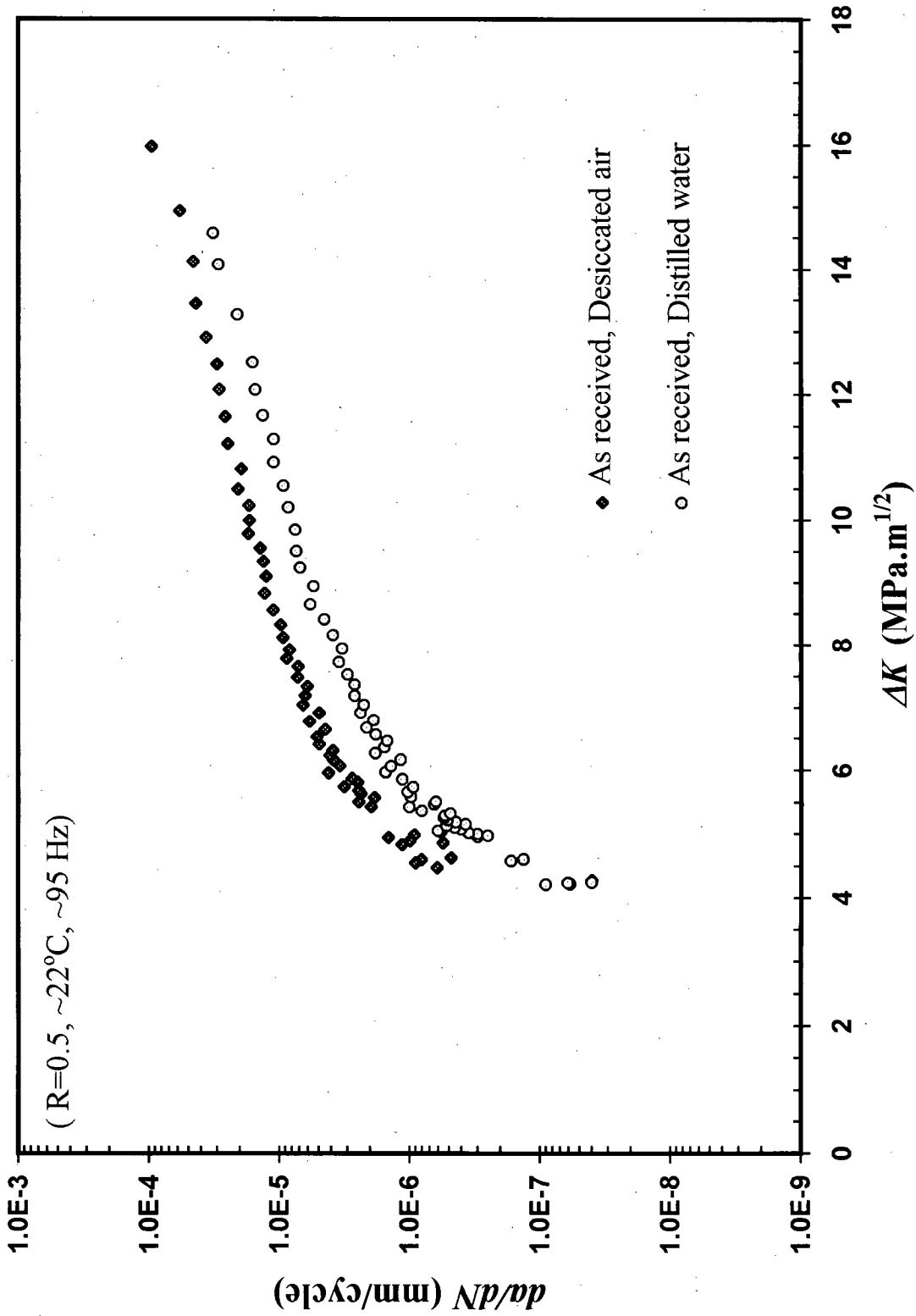


Figure 5.6 Fatigue crack growth behavior in pearlitic AISI 1070 steel.

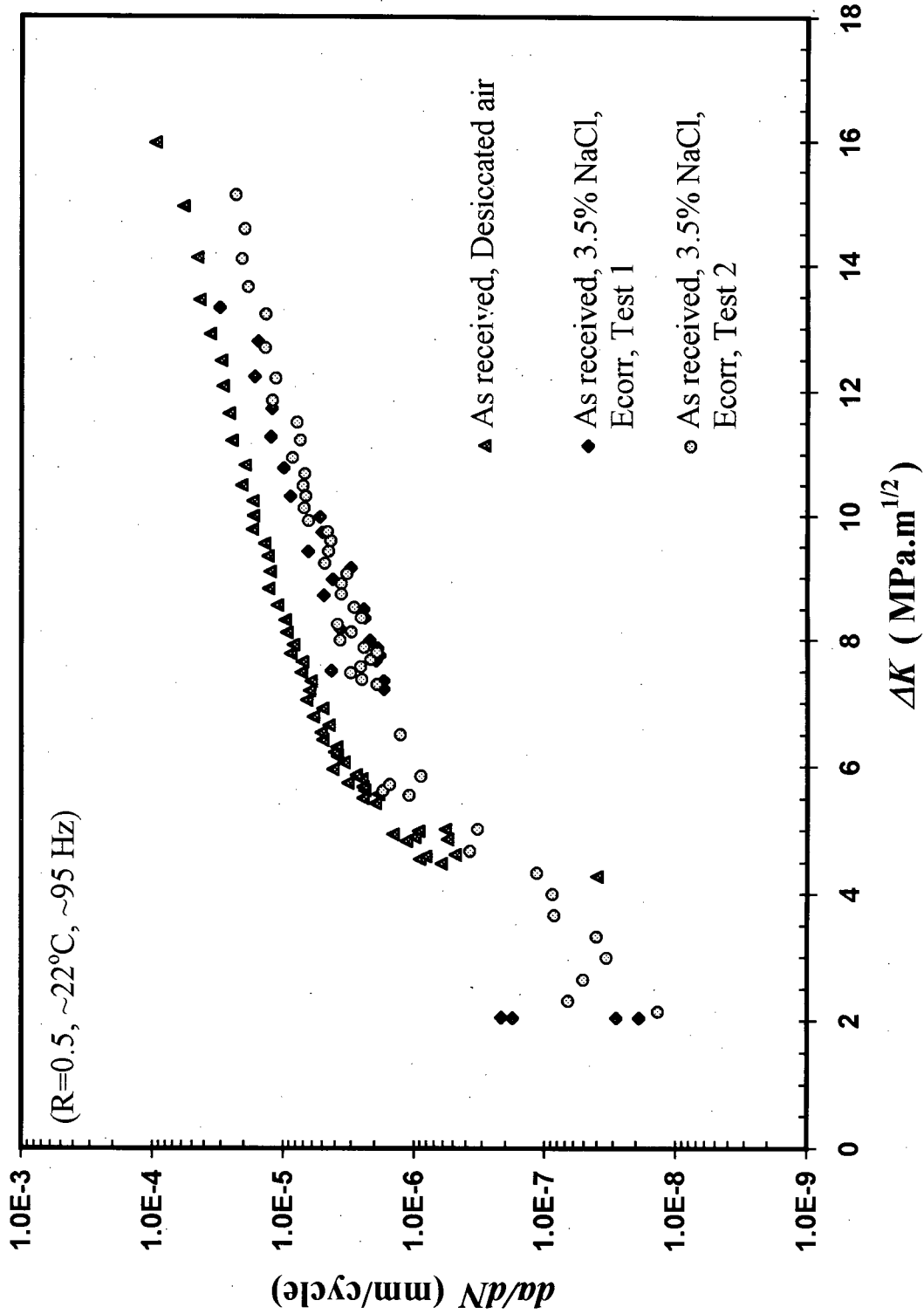


Figure 5.7 Fatigue crack growth behavior in pearlitic AISI 1070 steel in 3.5% NaCl and E_{corr}.

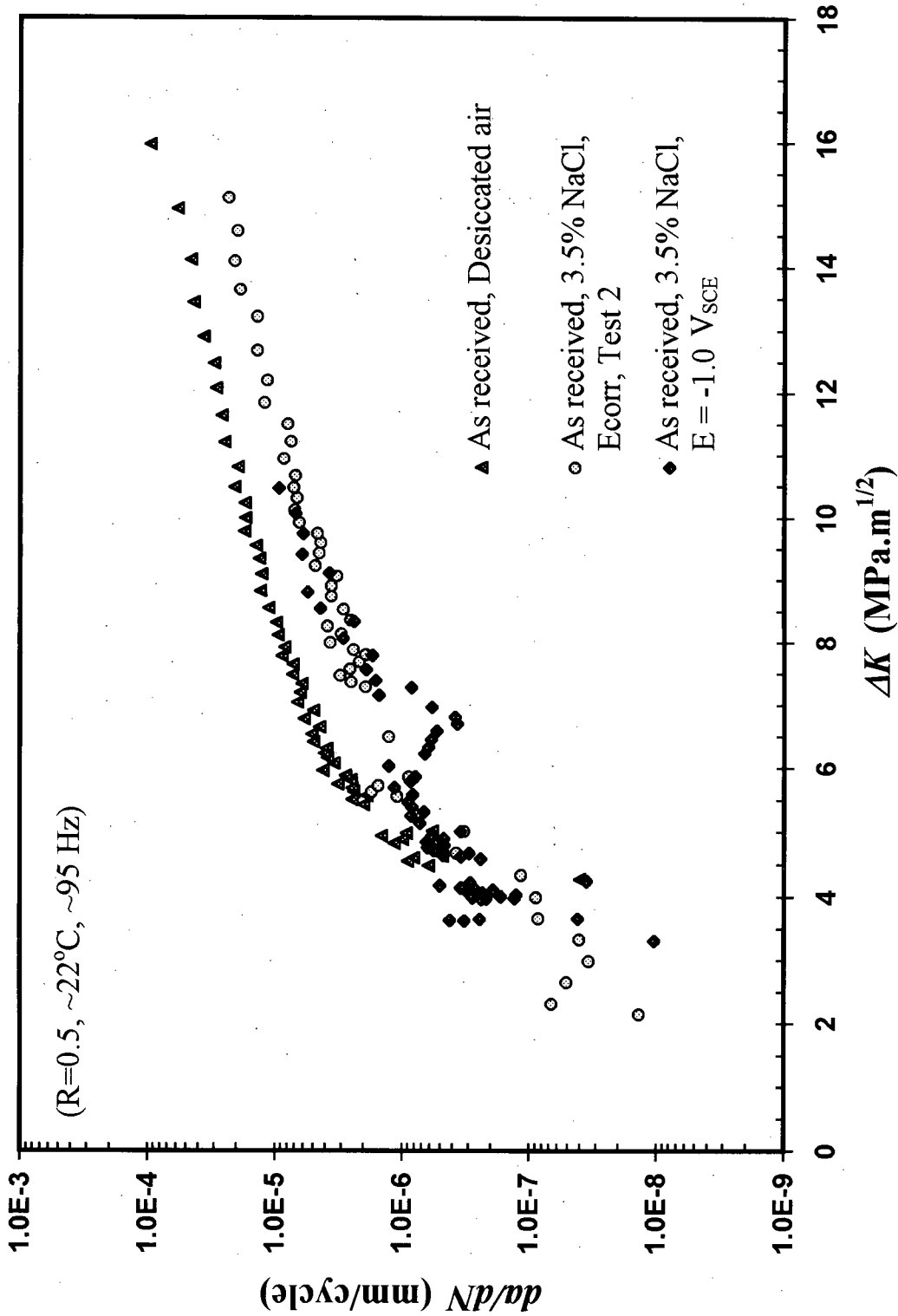


Figure 5.8 Effect of cathodic polarization on fatigue crack growth behavior in pearlitic AISI 1070 steel at pH = 6.0.

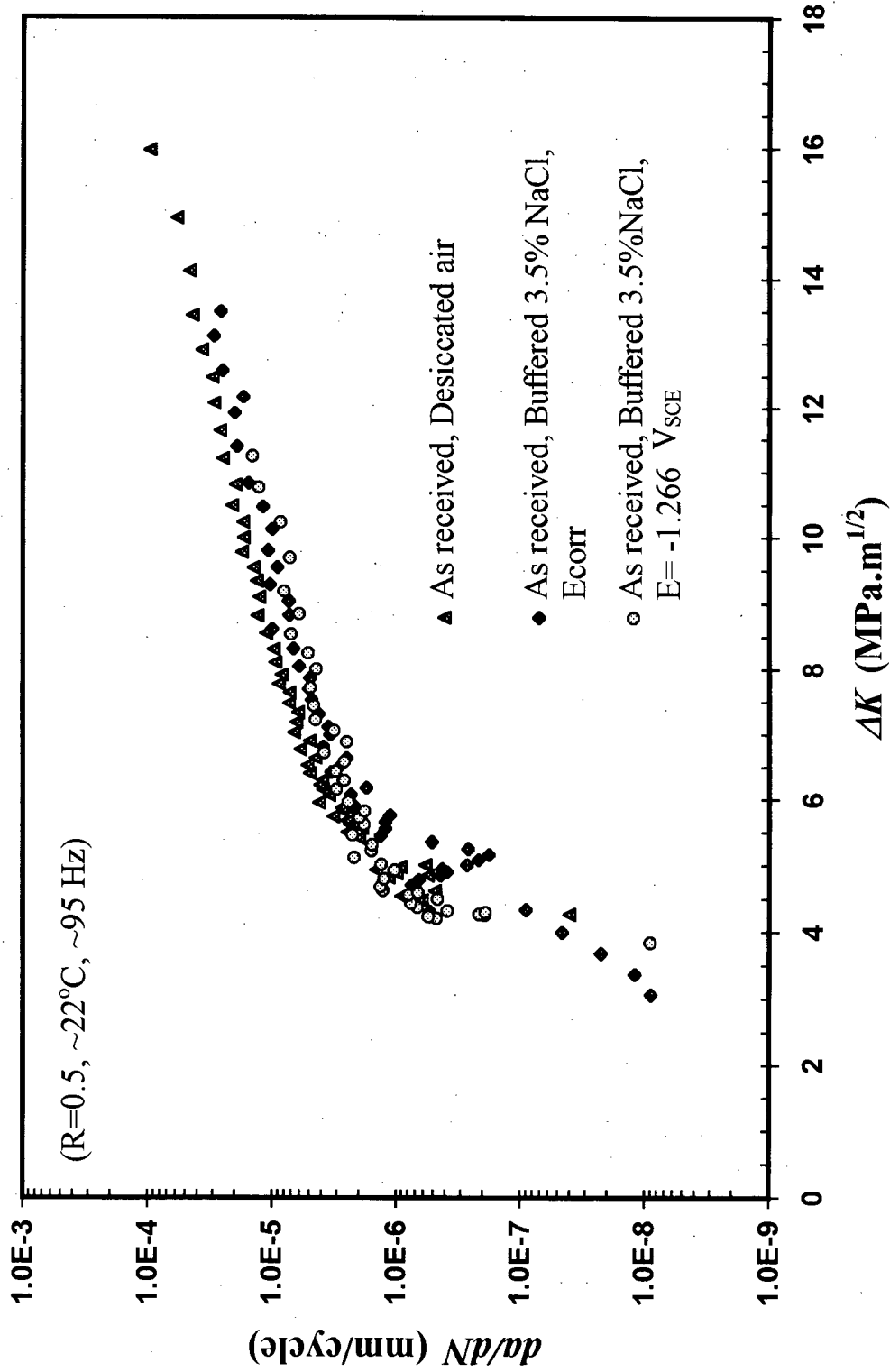


Figure 5.9 Effect of cathodic polarization on fatigue crack growth behavior in pearlitic AISI 1070 steel at pH = 10.5.

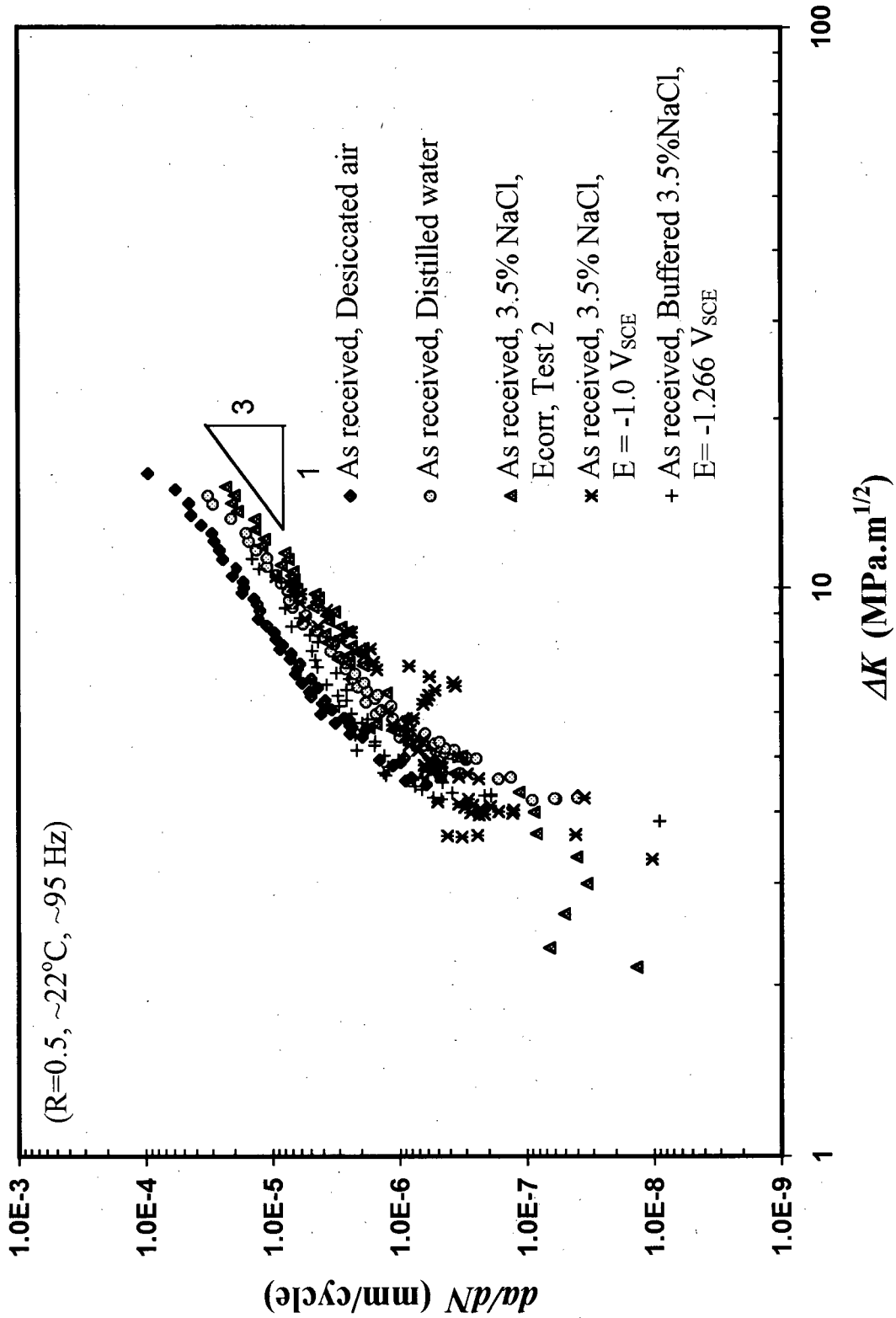


Figure 5.10 Effect of environment and ΔK on the growth of fatigue cracks in pearlitic AISI 1070 steel

5.3.2 Heat treated condition

The corrosion fatigue crack propagation behaviors of the fully spheroidized microstructure are shown in Figures 5.11 to 5.14. The results indicate that the fully spheroidized microstructure is more resistant to corrosion fatigue than the lamellar microstructure when tested in desiccated air (Figure 5.11). The spheroidizing treatment decreased the fatigue crack growth rates by a factor of ~ 4 at low ΔK values. However, the HT curve is similar in shape to the AR condition, and followed the Paris power law with $m \cong 3$ (see Figure 5.14). This result is in agreement with the exponent of ~ 2.9 for spheroidized 1% C-steel [124]. Figure 5.12 indicates that FCP rates in HT condition were enhanced under cathodic polarization, implying a hydrogen embrittlement mechanism. The slowest crack propagation rate was obtained in the fully spheroidized microstructure under cathodic protection conditions in 3.5% NaCl (Figure 5.13). Figure 5.15 compares the effect of heat treatment on the corrosion fatigue cracking behavior under cathodic conditions in 3.5% NaCl, where the AR material exhibits a lower ΔK_{th} and higher crack growth rates than the HT condition.

Cyclic threshold intensities (ΔK_{th}) for different testing condition were obtained from the data in Figures 5.11 to 5.13 and are listed in Table 5.4 with the corresponding da/dN .

Table 5.4 Threshold stress intensities for fatigue tests (HT condition).

Environment	Test potential (V _{SCE})*	ΔK_{th} MPa.m ^{1/2}	da/dN mm/cycle
Desiccated air	—	~ 4.1	1.0×10^{-8}
3.5% NaCl	$E_{corr}, -0.542 \text{ _ } -0.641$	~ 3.9	1.8×10^{-8}
3.5% NaCl	$E = -1.000$	~ 3.8	8.1×10^{-9}
Buffered 3.5% NaCl	$E = -1.266$	~ 4.0	9.4×10^{-9}

* Potential range from beginning to end of test.

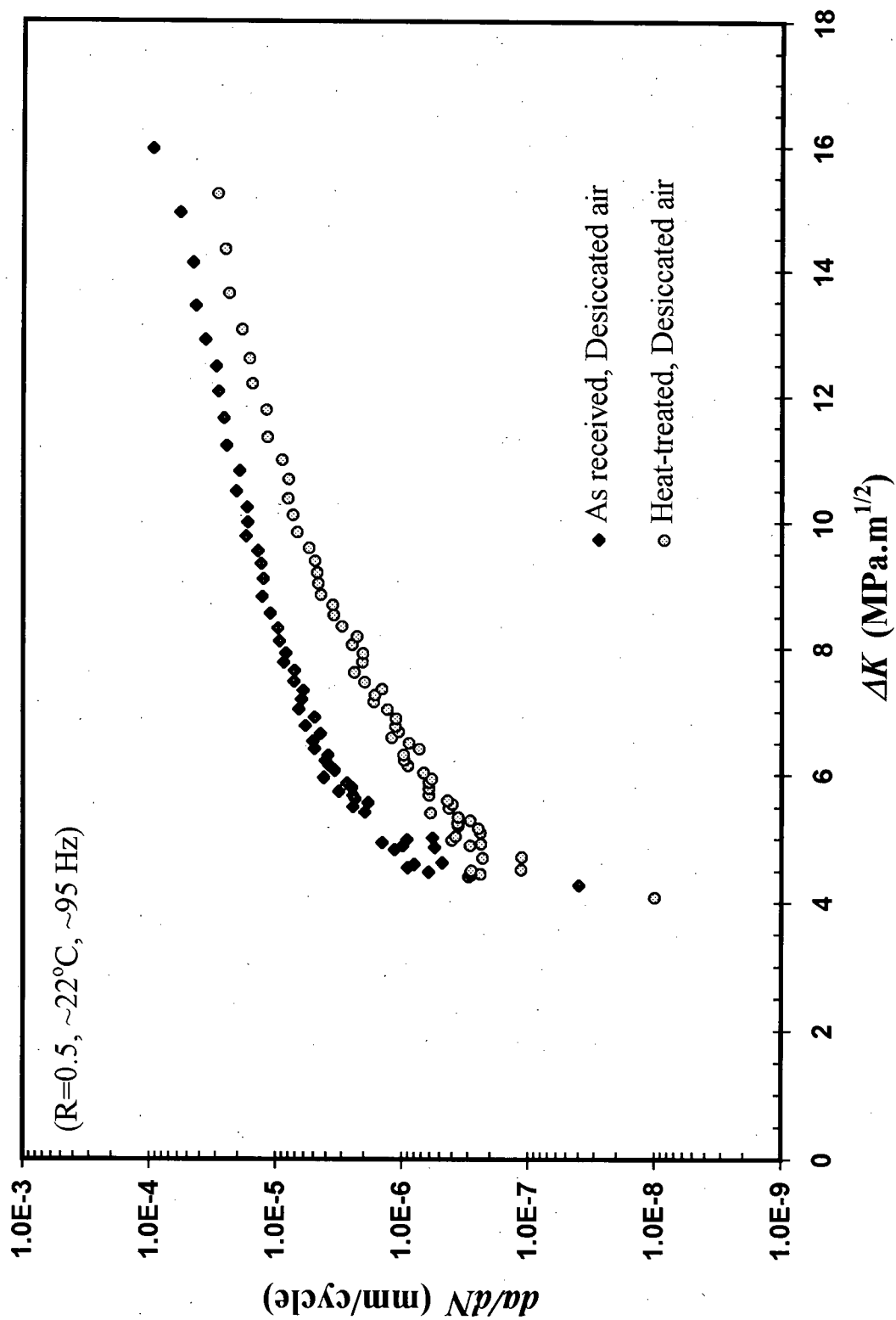


Figure 5.11 Effect of heat treatment (microstructure) on fatigue crack growth behavior in AISI 1070 steel.

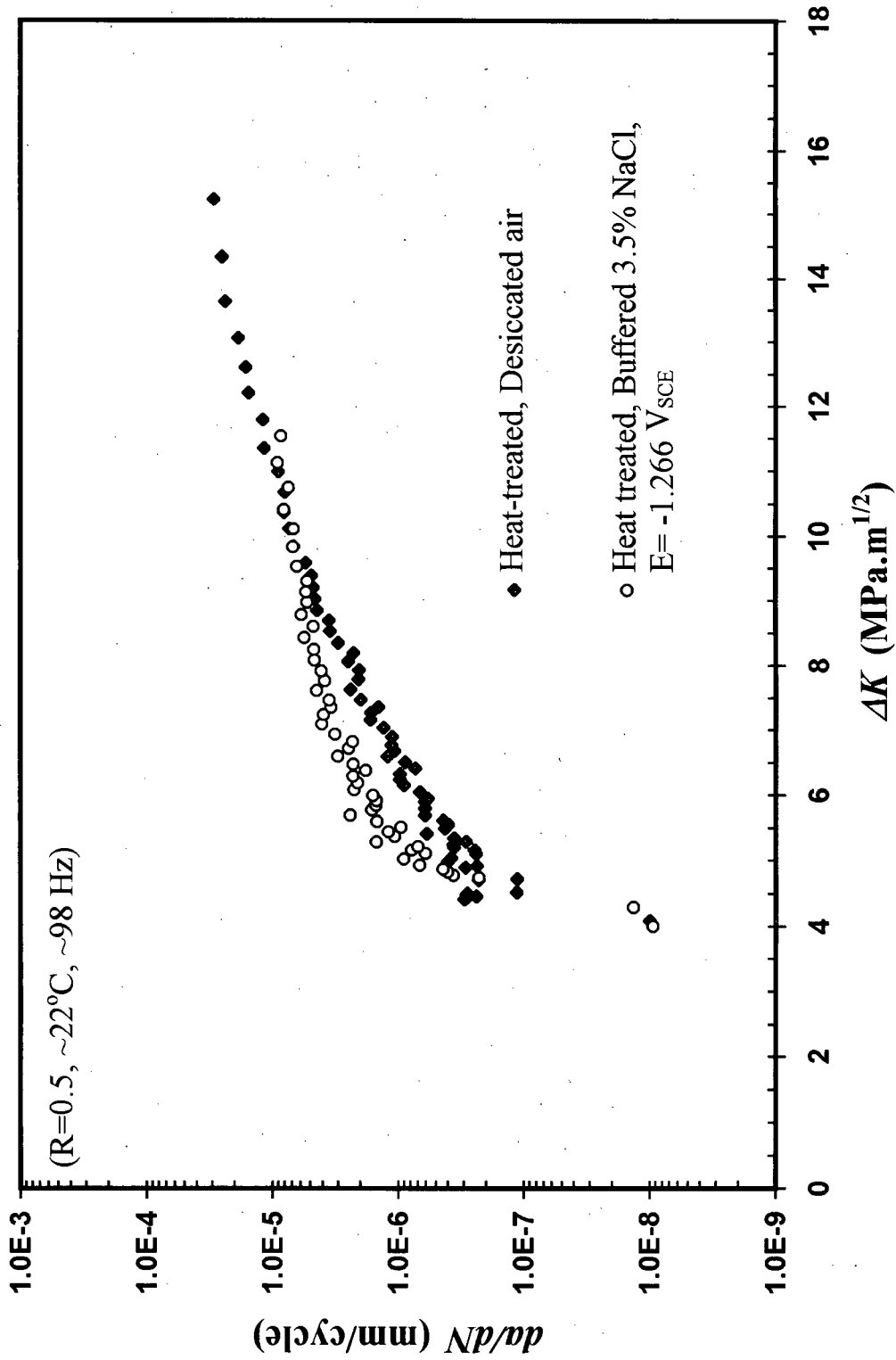


Figure 5.12 Fatigue crack growth behavior in spheroidized AISI 1070 steel.

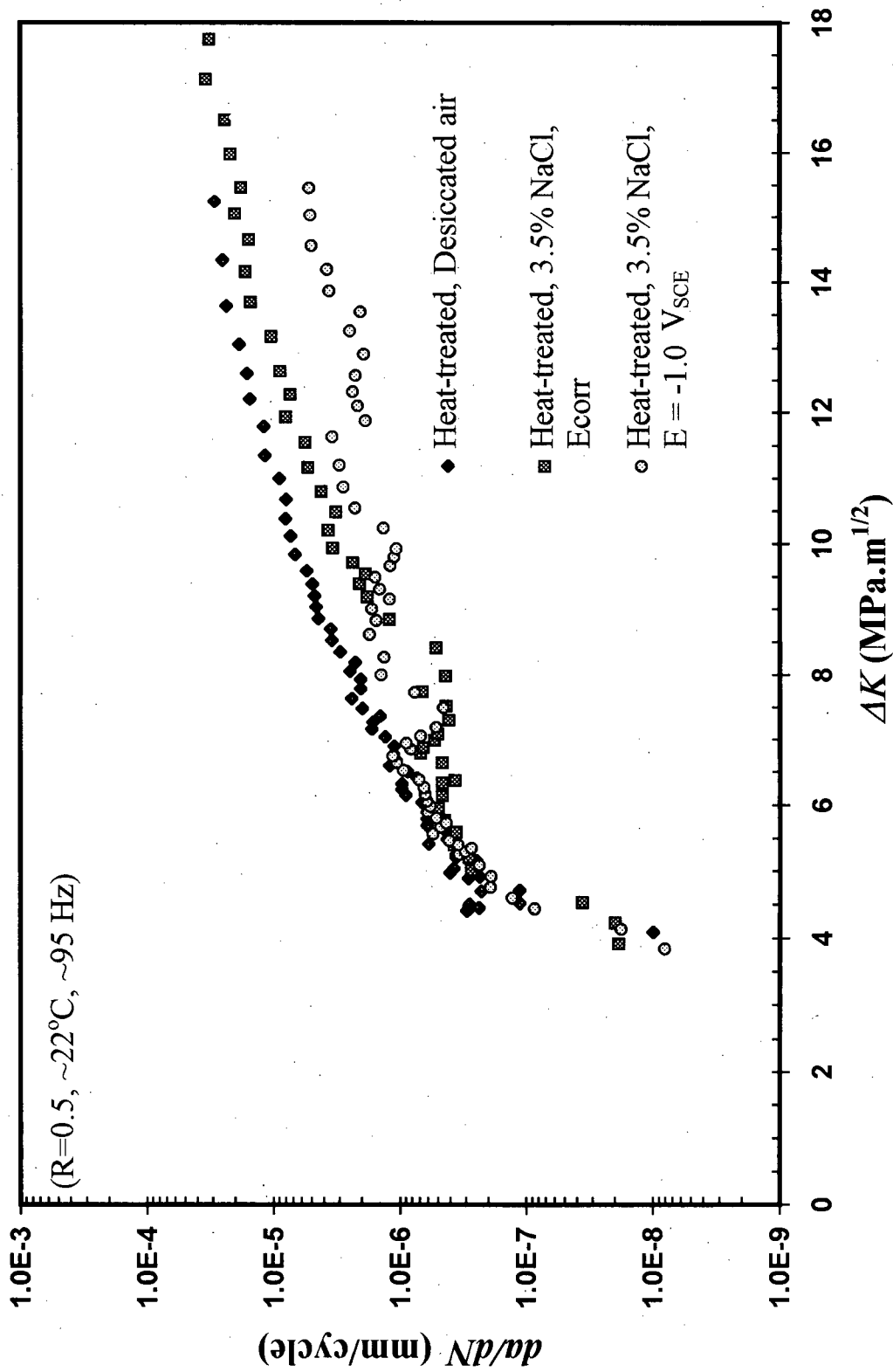


Figure 5.13 Effect of cathodic polarization on fatigue crack growth behavior in spheroidized AISI 1070 steel at pH = 6.0.

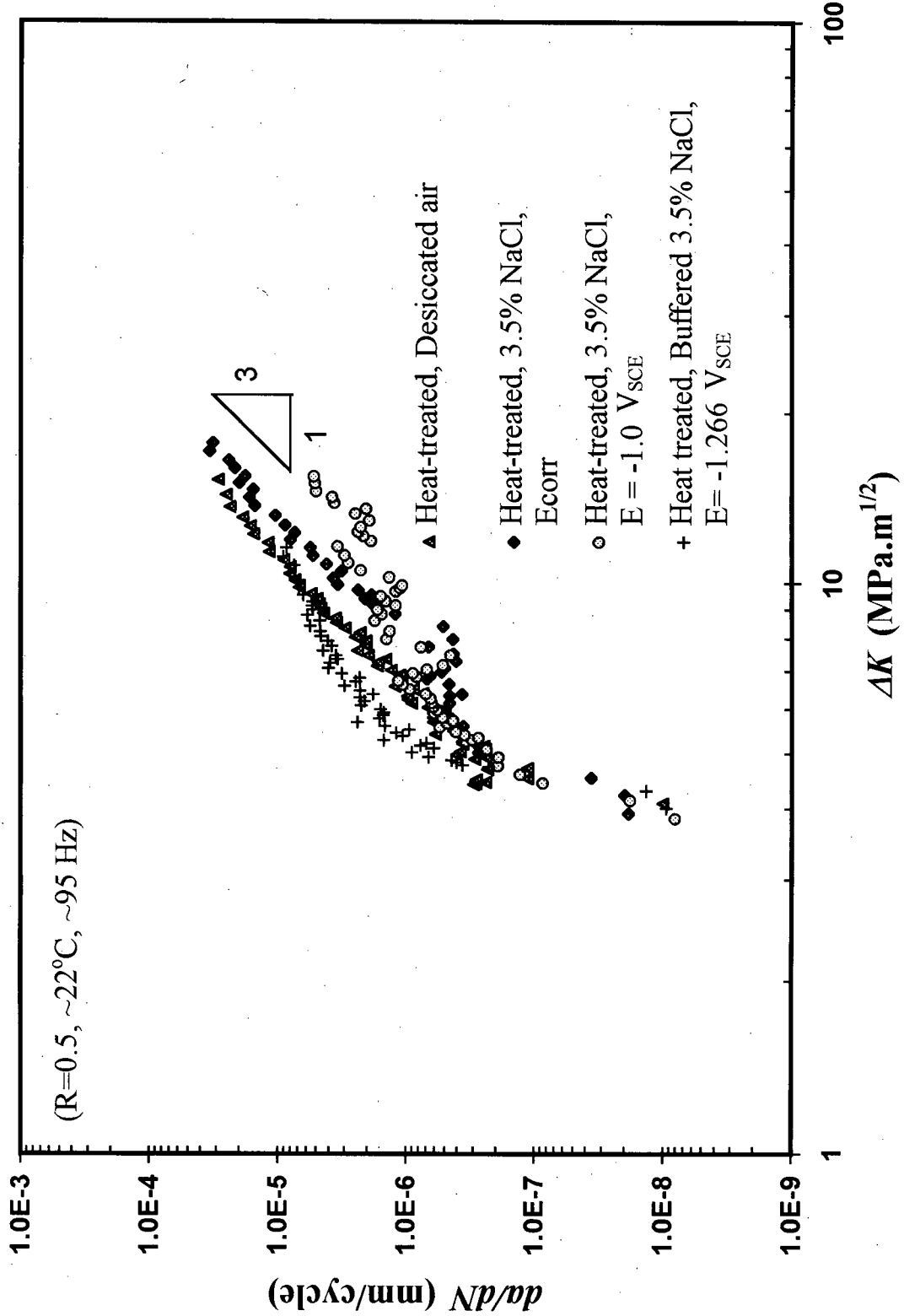


Figure 5.14 Effect of environment and ΔK on fatigue crack growth behavior in spheroidized AISI 1070 steel.

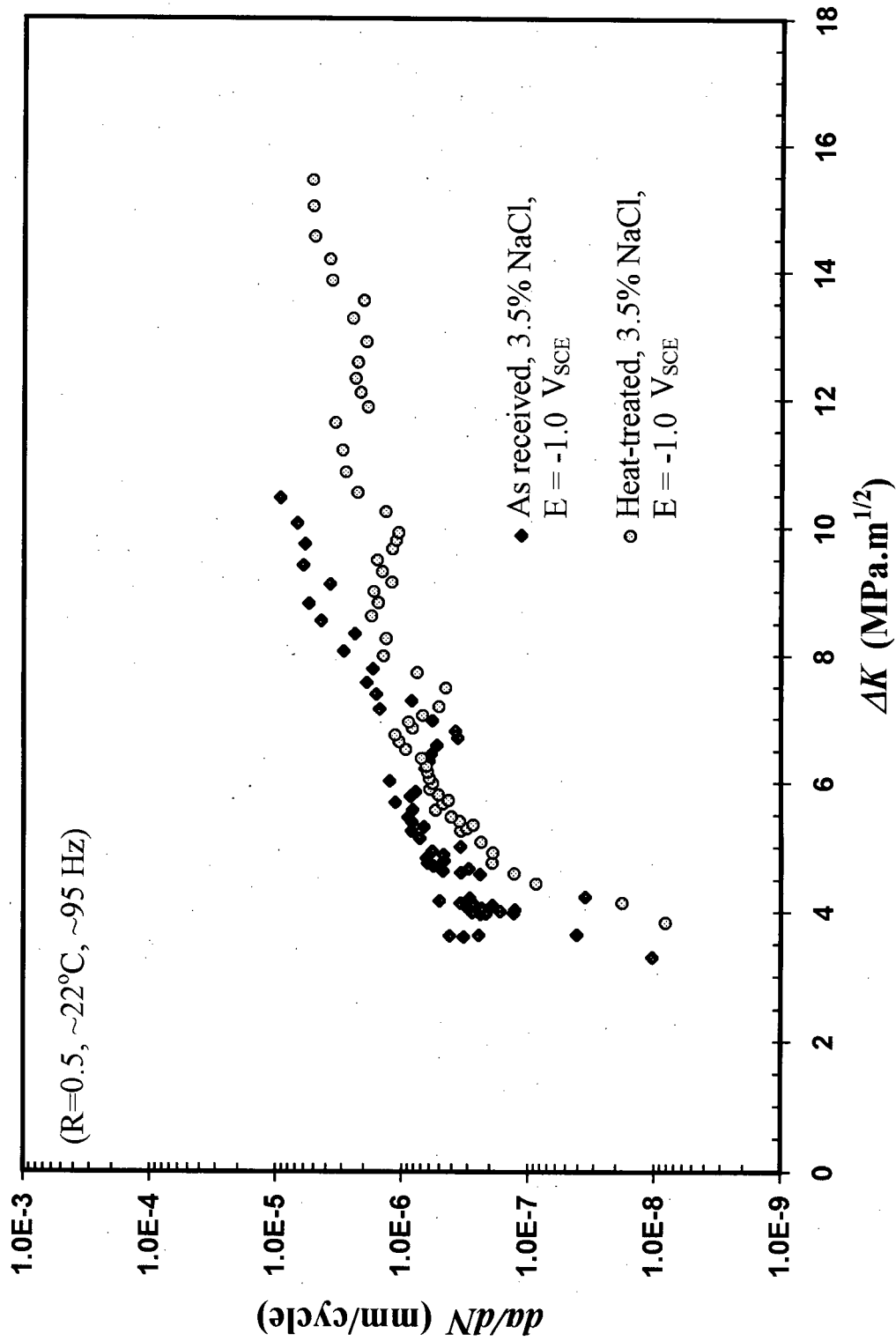


Figure 5.15 Fatigue crack growth behavior in AISI 1070 steel in 3.5% NaCl polarized to -1.0 V_{SCE}.

5.4 SEM fractography

All fracture surfaces were examined by scanning electron microscopy (SEM). Many micrographs were obtained but are not shown due to their great similarity. Representative micrographs were chosen for presentation and discussion. Visual examination of the macroscopic fracture surfaces showed that the crack was well behaved. The crack front profile was straight and unbowed and crack growth occurred equally at the mid-thickness and on both sides of the specimens. The macroscopic plane of the fatigue crack remained in the original crack plane. Fracture surface morphologies obtained from various test conditions revealed that fatigue failures occurred exclusively by transgranular cracking with respect to prior austenite grain boundaries.

SEM observation of the tensile test fracture surfaces revealed that the fracture occurred by a characteristic cleavage-like failure. Fracture was predominantly brittle and the surface topography was found to consist of crystalline facets. The fractographic features in the tensile specimens (not shown) were similar to fatigue specimens fractured in the overload region.

5.4.1 As received condition

The principal fractographic features of the AR condition are illustrated in the SEM fractographs of Figures 5.16 to 5.21, where the macroscopic direction of crack propagation is from top to bottom of the micrograph. The low and intermediate ΔK cracking region showed fracture topography that correlated directly with the lamellar microstructure. The transition between stage-I and stage-II crack propagation was not well-defined and fatigue striations

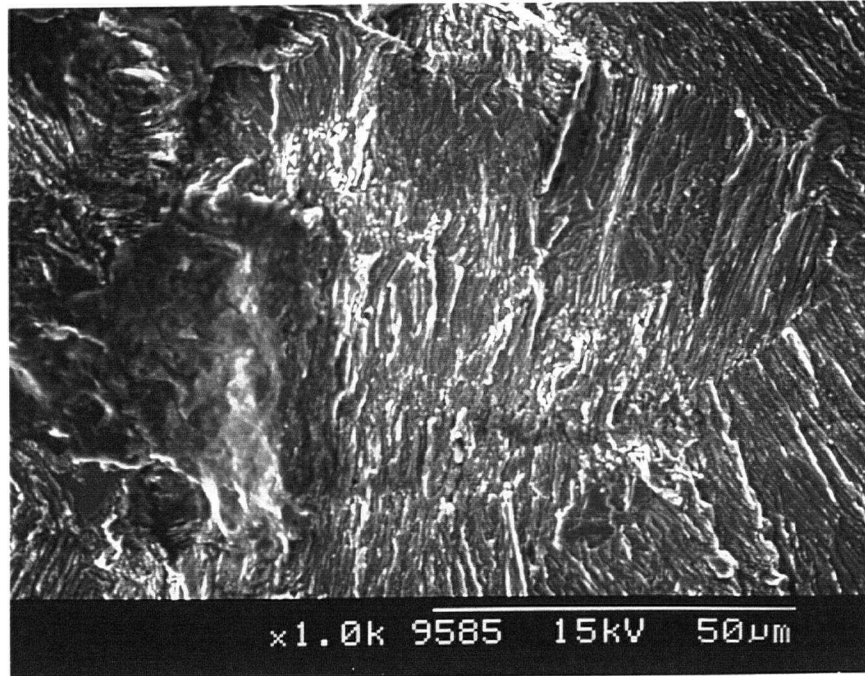
were not visible (Figure 5.16). The overload region showed crystallographic cleavage-like facets and river lines (Figure 5.17), and was identical in all testing conditions.

For samples tested in aqueous environments, very similar fractography was observed near ΔK_{th} on all specimens, irrespective of the test environment or electrochemical potential. Dark corrosion bands were visible in the near-threshold regions of all specimens tested in the saline environments. Corrosion products on fracture surfaces increased with the corrosiveness of the environment, with a minimum in distilled water and a maximum in 3.5% *NaCl* solution (Figures 5.18 to 5.21). The cathodically polarized specimens were protected against corrosion only at the surface while crack interior exhibited severe corrosion (Figure 5.20). This was attributed to the uneven distribution of applied currents that occurs in shielded sites such as cracks [136]. The specimen tested in desiccated air had a dull gray appearance and a corrosion-free surface.

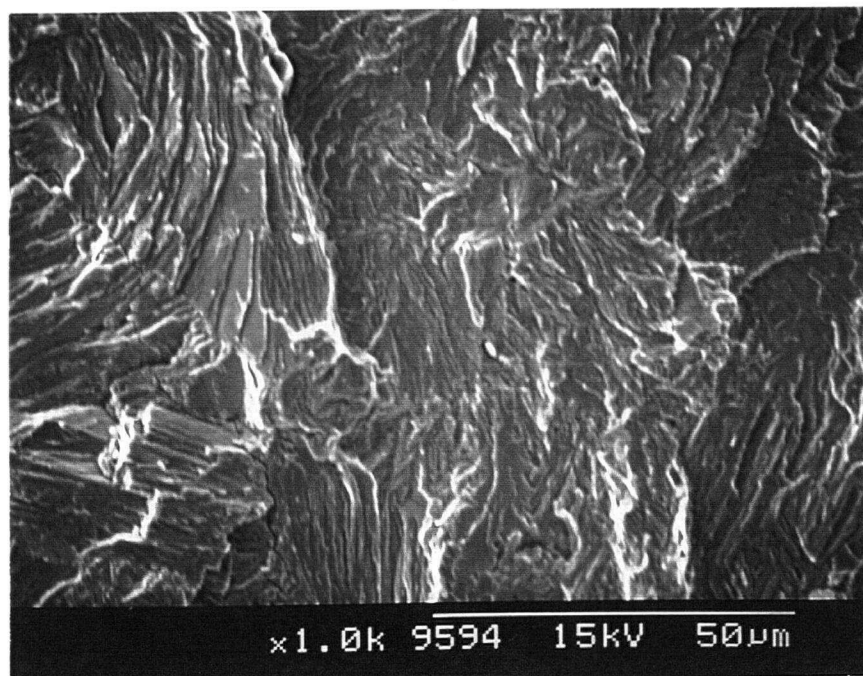
5.4.2 Heat treated condition

Figures 5.22 to 5.26 show the main fractographic features in the spheroidized microstructure. In all these fractographs, crack propagation is from top to bottom. Fracture surface morphology of the desiccated air test (Figure 5.22) shows more tear ridges than the corresponding test in the AR condition. This was most readily seen by the examination of SEM stereo pairs using a mirror stereoscope [137]. At higher ΔK values where the surfaces are less damaged by contact of opposing fracture surfaces, cementite particles appear unfractured (Figures 5.23b and 5.24b). Figure 5.25 shows that the fracture surface exhibits a major secondary cracking which correlates with the possibility of hydrogen charging effects

under cathodic polarization condition. These secondary cracks could be attributed to the branching caused by HIC as shown in Figure 2.2. The overload region (Figure 5.26) failed predominately by cleavage. However, some regions exhibited tear ridges with microvoid coalescence, indicating ductile tearing.

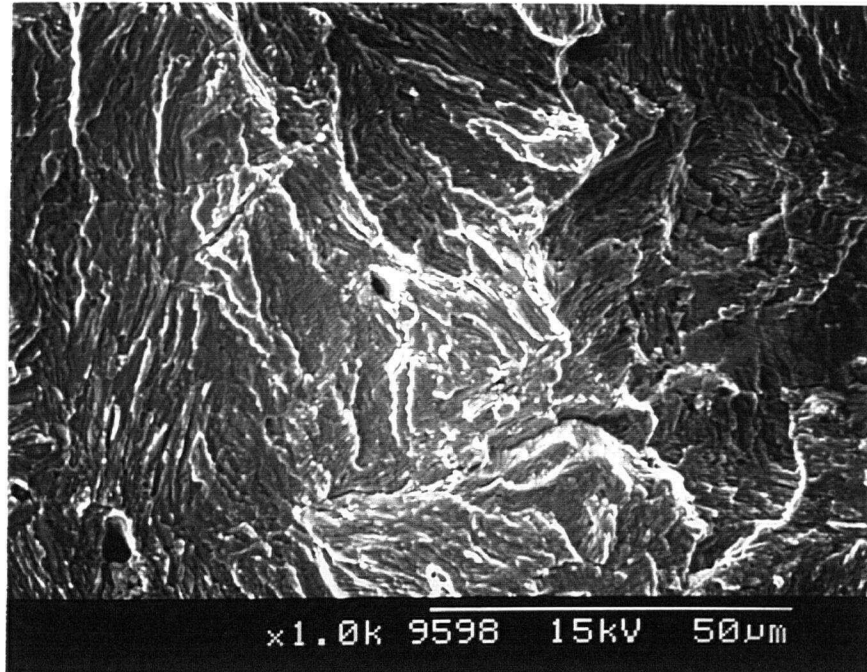


(a)

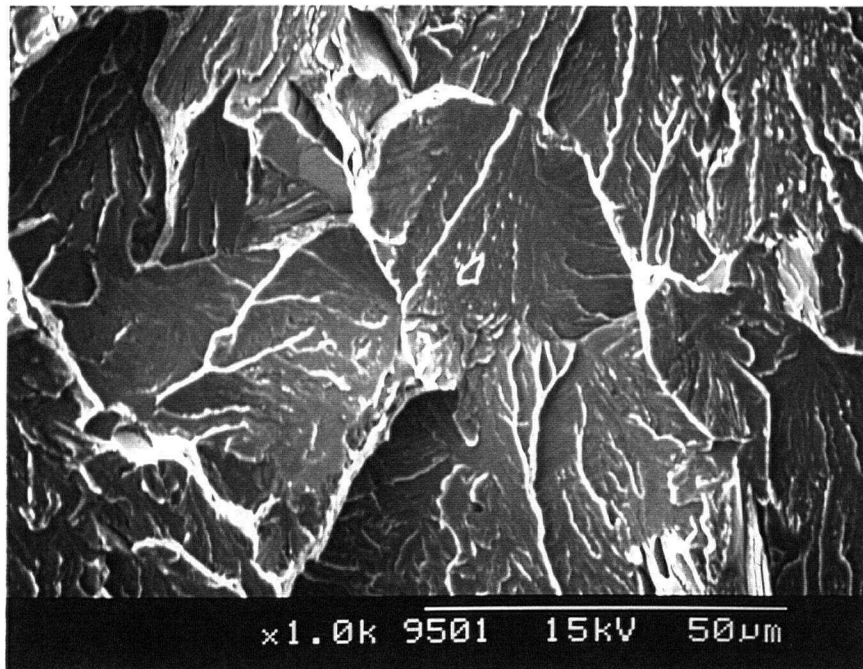


(b)

Figure 5.16 SEM fractograph showing fatigue cracking of pearlitic AISI 1070
(a) Desiccated air, stage-I, $\Delta K \cong 4.5 \text{ MPa}\cdot\text{m}^{1/2}$, $da/dN \cong 4.1 \times 10^{-7} \text{ mm/cycle}$
(b) Desiccated air, stage-II, $\Delta K \cong 8.0 \text{ MPa}\cdot\text{m}^{1/2}$, $da/dN \cong 8.3 \times 10^{-6} \text{ mm/cycle}$

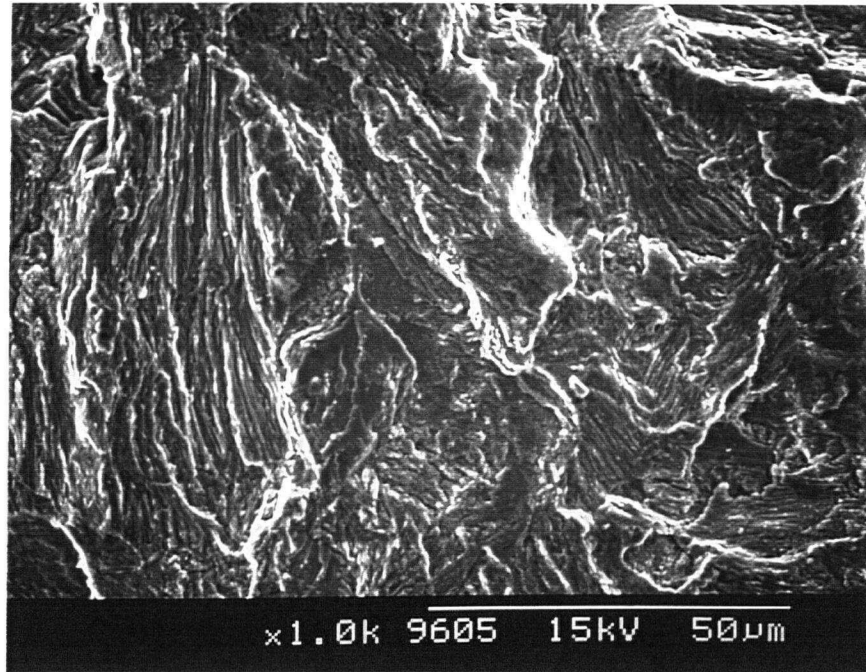


(a)

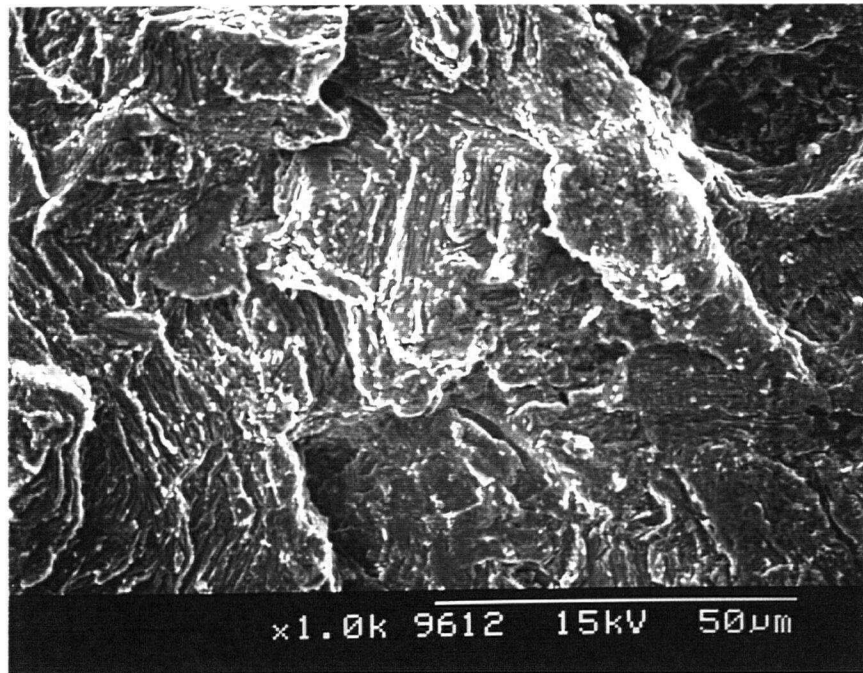


(b)

Figure 5.17 SEM fractograph showing fatigue cracking of pearlitic AISI 1070
(a) Desiccated air, stage-II, $\Delta K \cong 16 \text{ MPa}\cdot\text{m}^{1/2}$, $da/dN \cong 1.0 \times 10^{-4} \text{ mm/cycle}$
(b) Desiccated air, stage-III (overload), cleavage fracture.

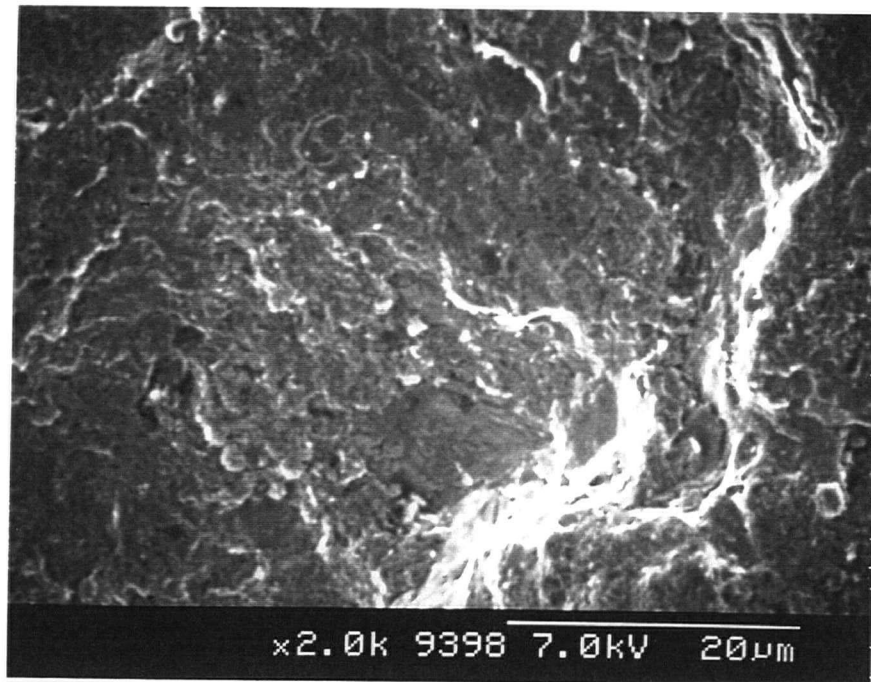


(a)

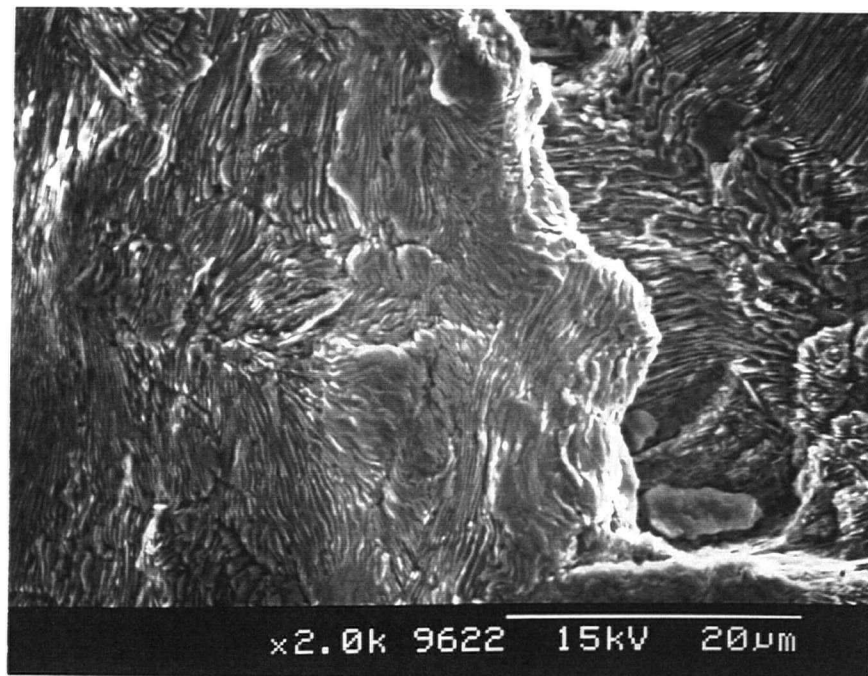


(b)

Figure 5.18 SEM fractograph showing fatigue cracking of pearlitic AISI 1070
(a) Distilled water, stage-I, $\Delta K \cong 4.2 \text{ MPa}\cdot\text{m}^{1/2}$, $da/dN \cong 4.0 \times 10^{-8} \text{ mm/cycle}$
(b) Distilled water, stage-II, $\Delta K \cong 8.2 \text{ MPa}\cdot\text{m}^{1/2}$, $da/dN \cong 3.9 \times 10^{-6} \text{ mm/cycle}$

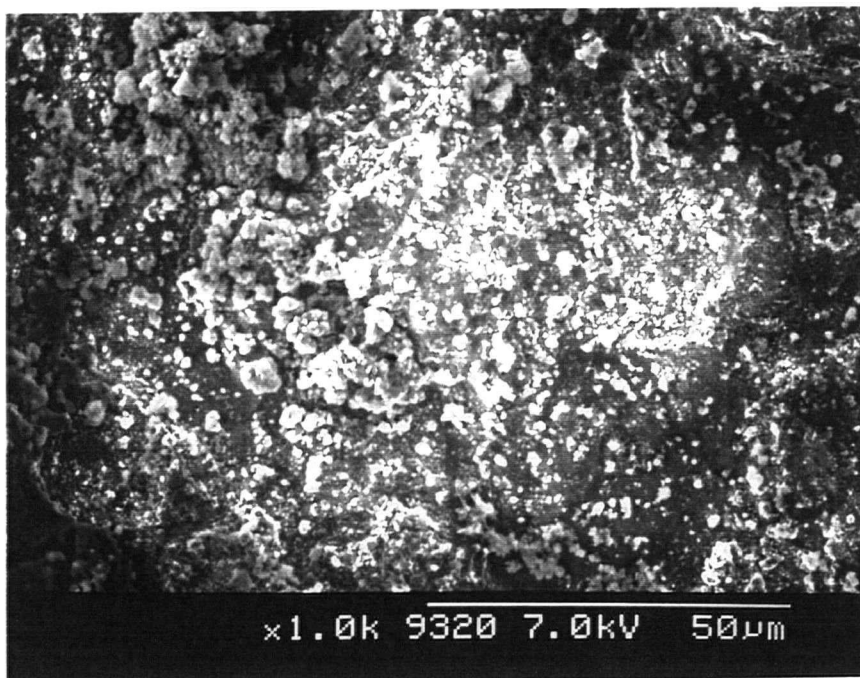


(a)

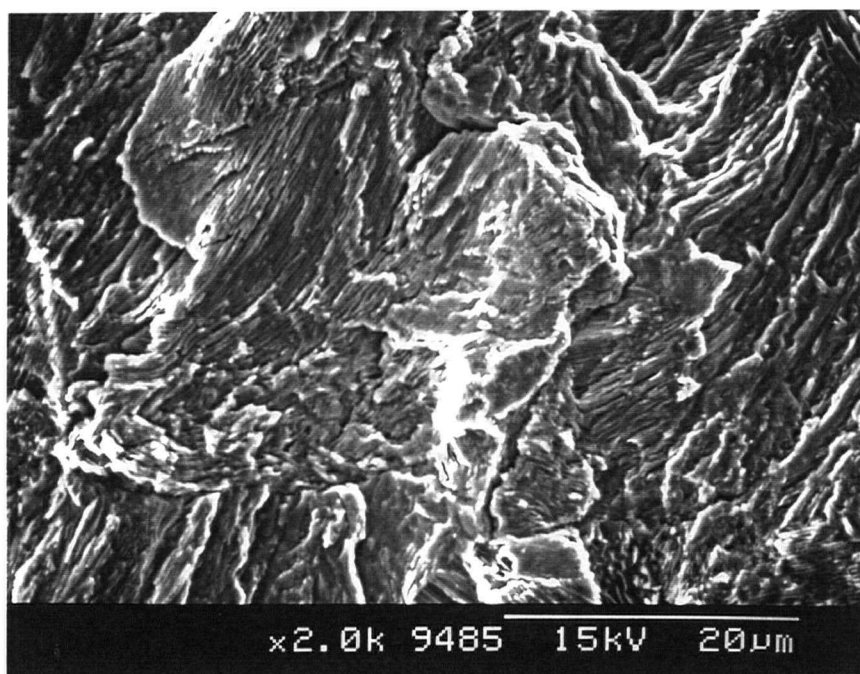


(b)

Figure 5.19 SEM fractograph showing fatigue cracking of pearlitic AISI 1070
(a) 3.5% NaCl, E_{corr} , stage-I, before cleaning, $\Delta K \cong 2.3 \text{ MPa}\cdot\text{m}^{1/2}$, $da/dN \cong 6.7 \times 10^{-8} \text{ mm/cycle}$
(b) 3.5% NaCl, E_{corr} , stage-I, after cleaning, $\Delta K \cong 2.3 \text{ MPa}\cdot\text{m}^{1/2}$, $da/dN \cong 6.7 \times 10^{-8} \text{ mm/cycle}$

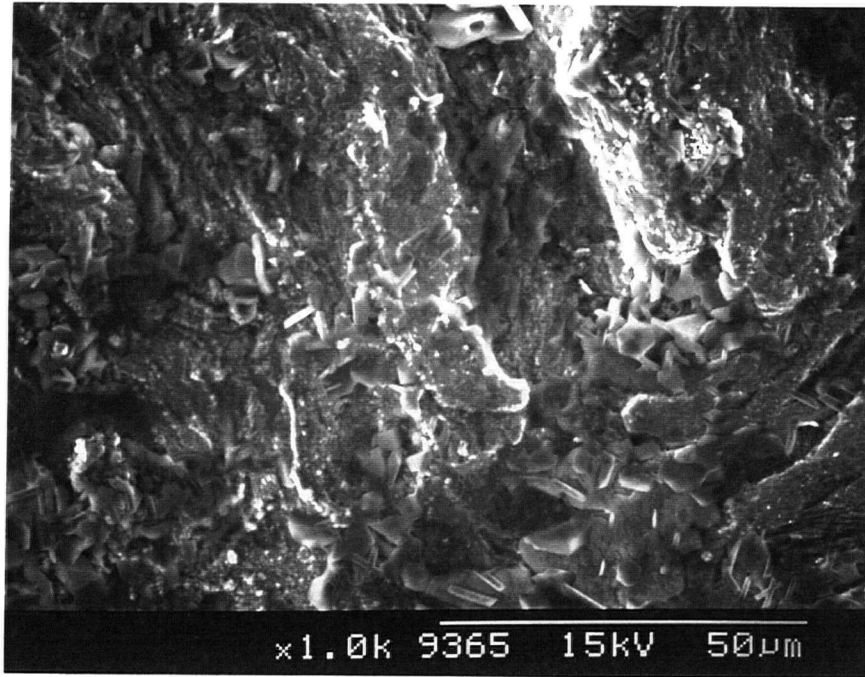


(a)

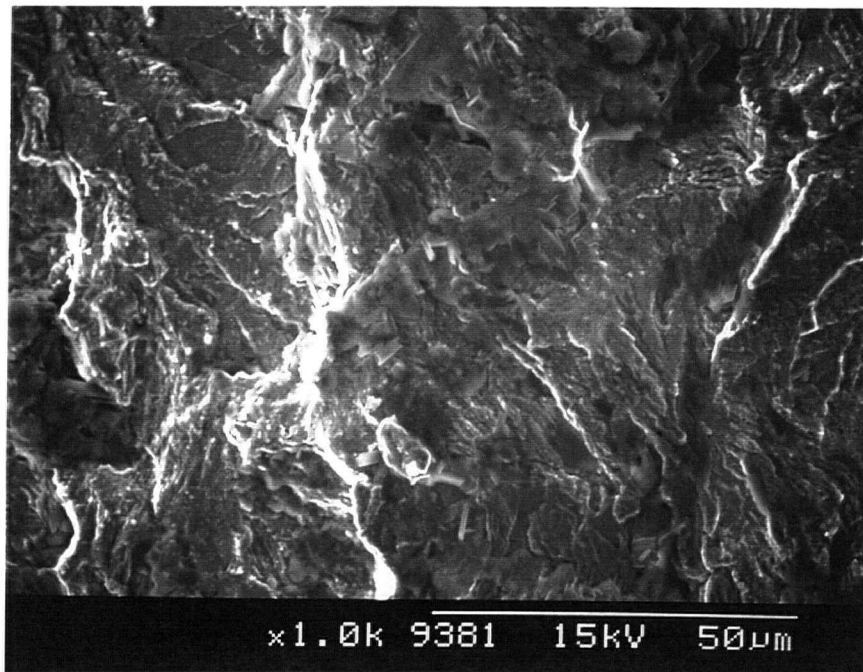


(b)

Figure 5.20 SEM fractograph showing fatigue cracking of pearlitic AISI 1070
(a) 3.5% NaCl, $E = -1.0 V_{SCE}$, before cleaning, $\Delta K \cong 8.1 \text{ MPa}\cdot\text{m}^{1/2}$, $da/dN \cong 2.9 \times 10^{-6} \text{ mm/cycle}$
(b) 3.5% NaCl, $E = -1.0 V_{SCE}$, after cleaning, $\Delta K \cong 8.1 \text{ MPa}\cdot\text{m}^{1/2}$, $da/dN \cong 2.9 \times 10^{-6} \text{ mm/cycle}$

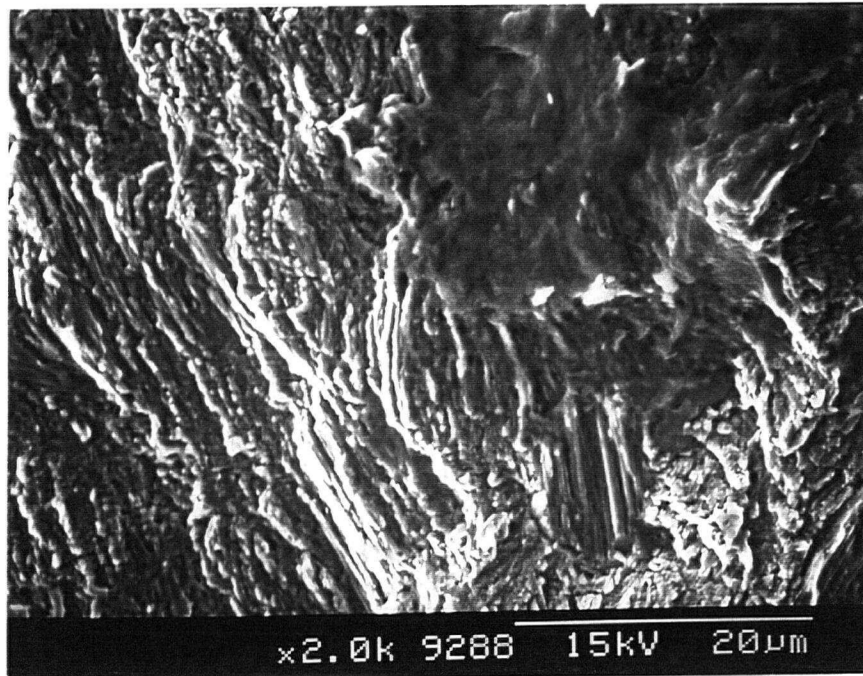


(a)

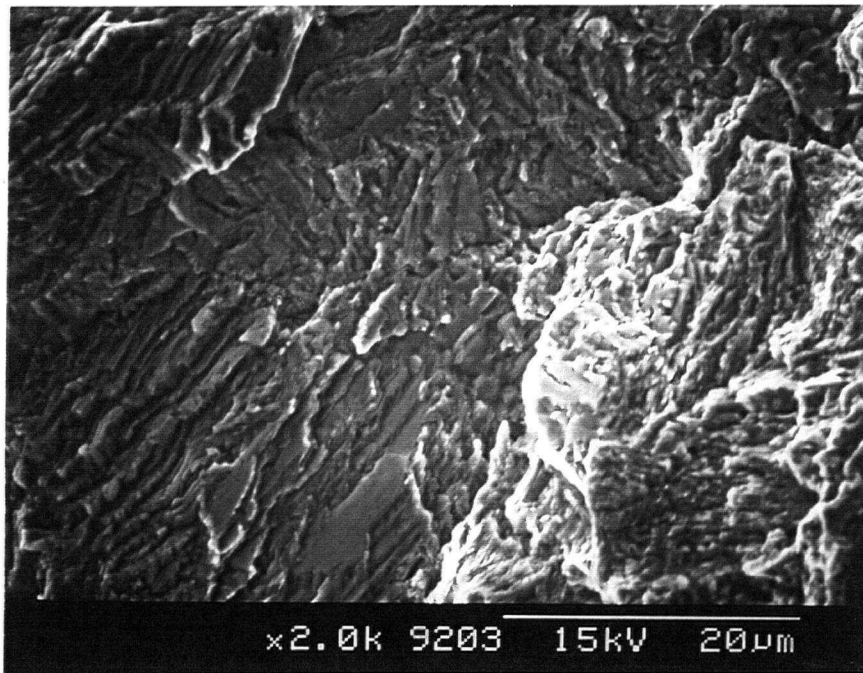


(b)

Figure 5.21 SEM fractographs showing fatigue cracking of pearlitic AISI 1070
(a) Buffered 3.5% NaCl, $E = -1.266 V_{SCE}$, before cleaning, $\Delta K \cong 4.6 \text{ MPa}\cdot\text{m}^{1/2}$
(b) Buffered 3.5% NaCl, $E = -1.266 V_{SCE}$, before cleaning, $\Delta K \cong 9.2 \text{ MPa}\cdot\text{m}^{1/2}$



(a)

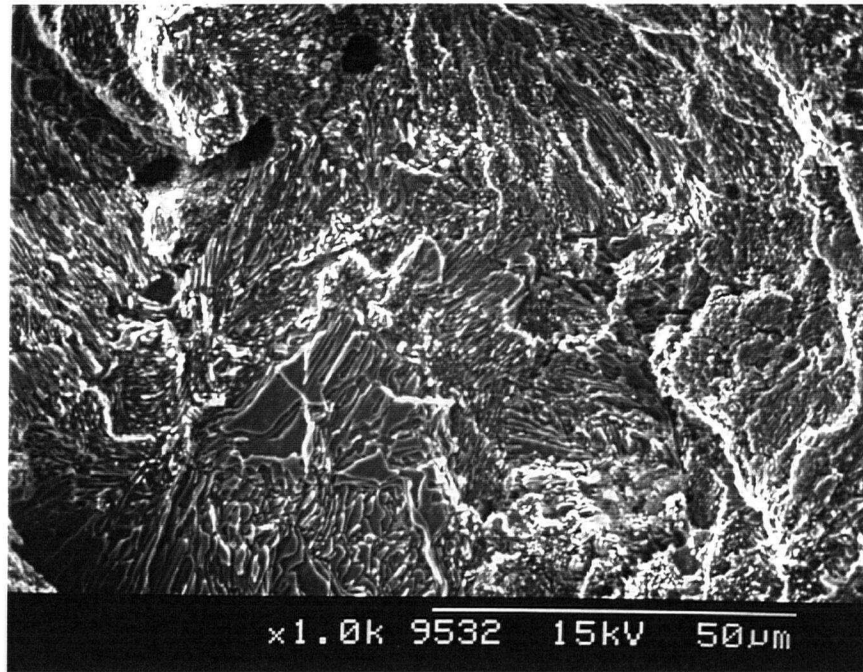


(b)

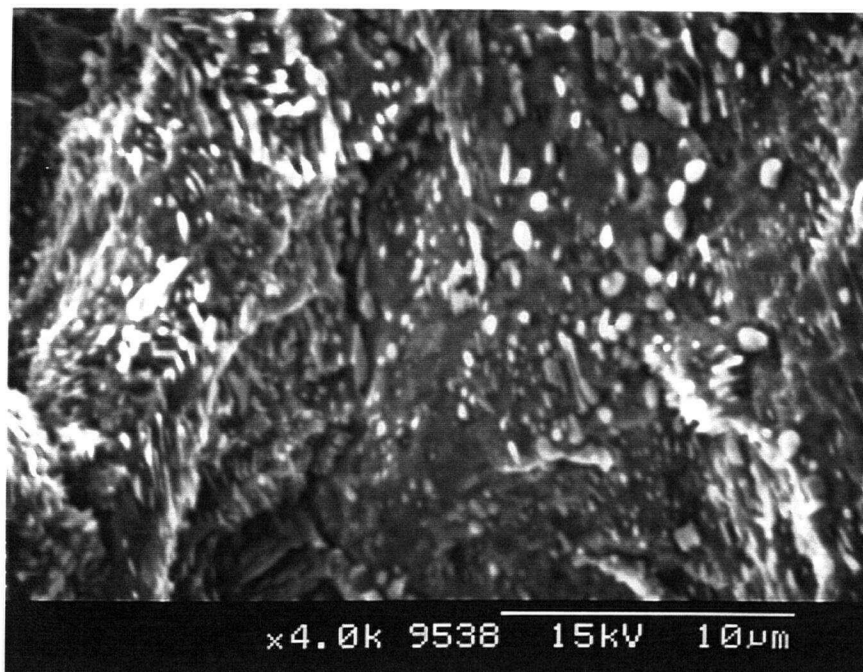
Figure 5.22 SEM fractographs showing fatigue cracking of spheroidized AISI 1070

(a) Desiccated air, stage-I, $\Delta K \cong 4.4 \text{ MPa}\cdot\text{m}^{1/2}$, $da/dN \cong 2.9 \times 10^{-7} \text{ mm/cycle}$

(b) Desiccated air, stage-II, $\Delta K \cong 9.0 \text{ MPa}\cdot\text{m}^{1/2}$, $da/dN \cong 4.6 \times 10^{-6} \text{ mm/cycle}$

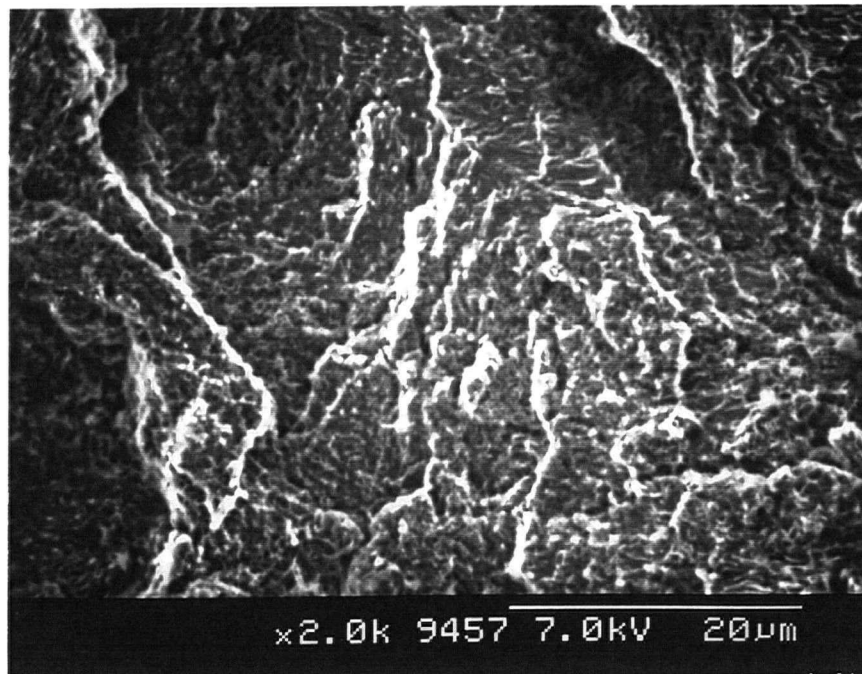


(a)

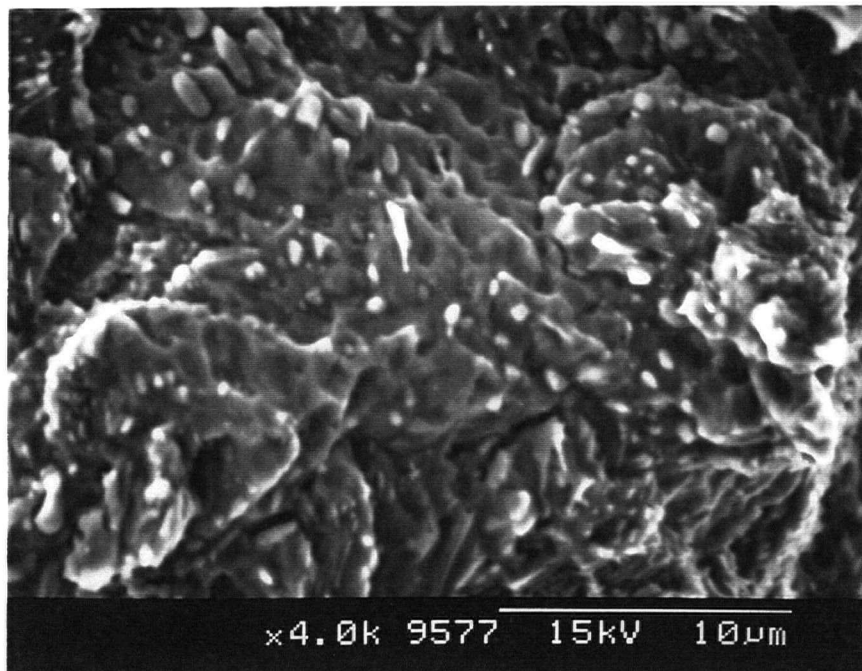


(b)

Figure 5.23 SEM fractographs showing fatigue cracking of spheroidized AISI 1070
(a) 3.5% NaCl, E_{corr} , after cleaning, $\Delta K \cong 8.0 \text{ MPa}\cdot\text{m}^{1/2}$, $da/dN \cong 2.9 \times 10^{-7} \text{ mm/cycle}$
(b) 3.5% NaCl, E_{corr} , after cleaning, $\Delta K \cong 14.1 \text{ MPa}\cdot\text{m}^{1/2}$, $da/dN \cong 4.6 \times 10^{-6} \text{ mm/cycle}$

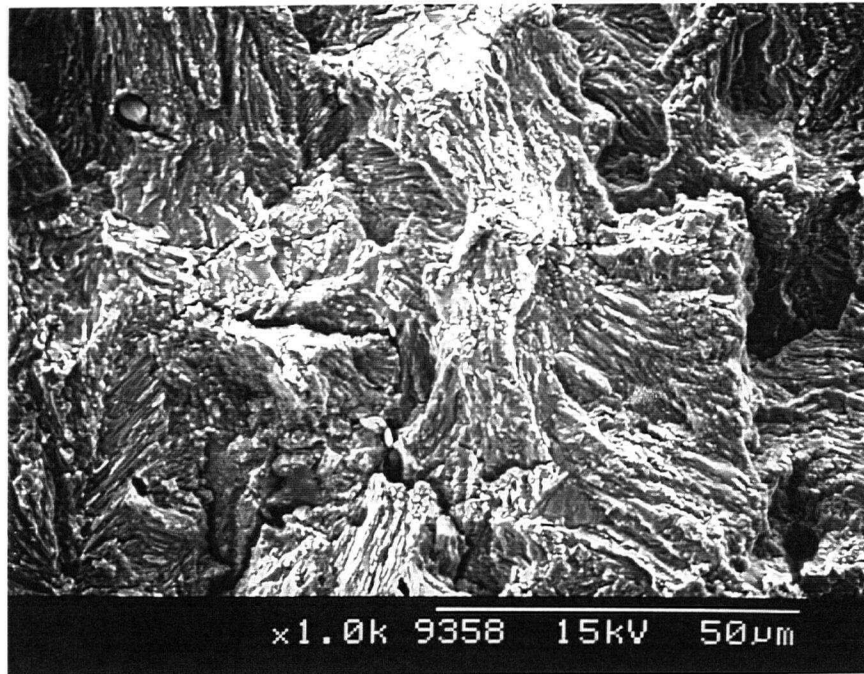


(a)

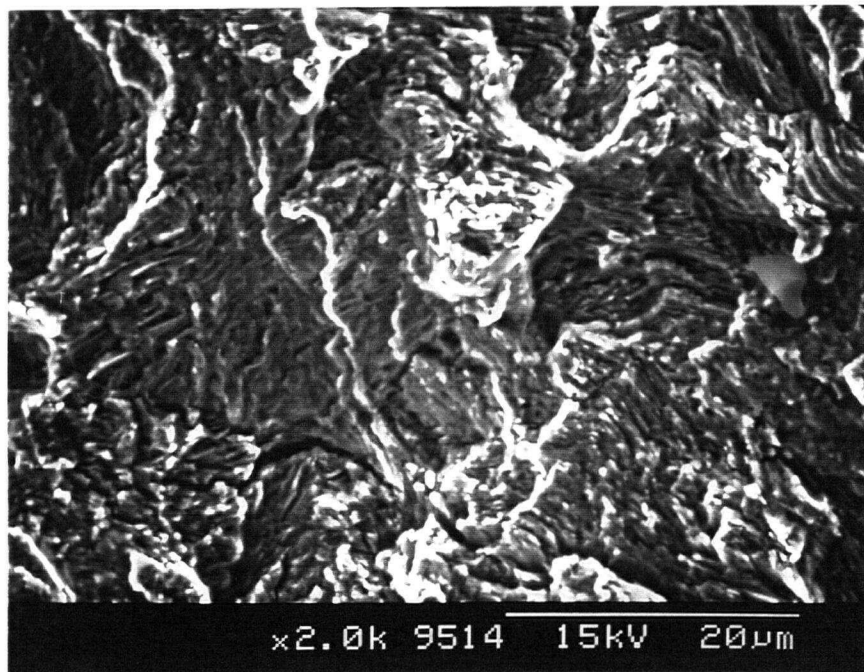


(b)

Figure 5.24 SEM fractographs showing fatigue cracking of spheroidized AISI 1070
(a) 3.5% NaCl, $E = -1.0 V_{SCE}$, before cleaning, $\Delta K \cong 15.4 \text{ MPa}\cdot\text{m}^{1/2}$, end of test
(b) 3.5% NaCl, $E = -1.0 V_{SCE}$, after cleaning, $\Delta K \cong 15.4 \text{ MPa}\cdot\text{m}^{1/2}$, end of test.

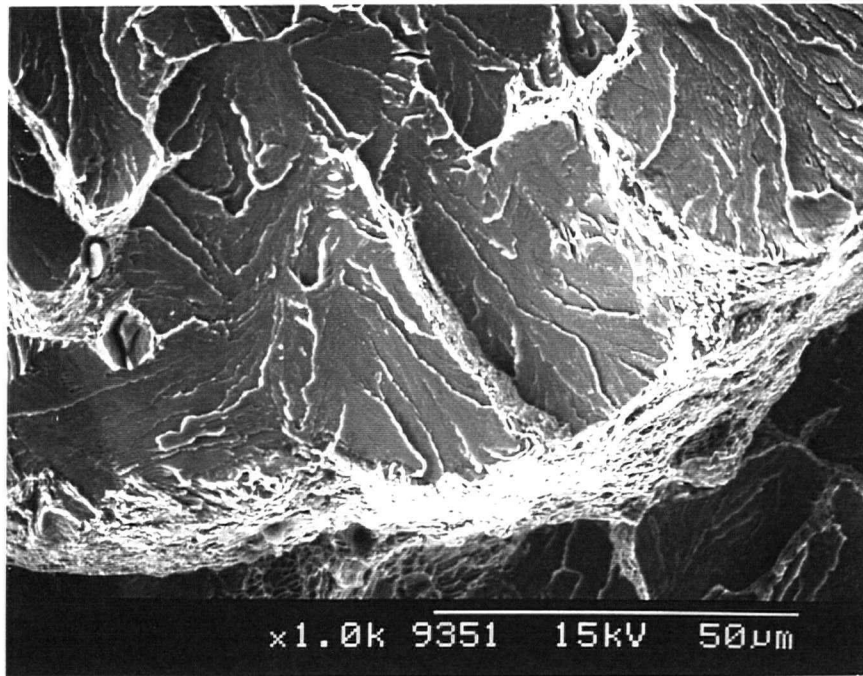


(a)

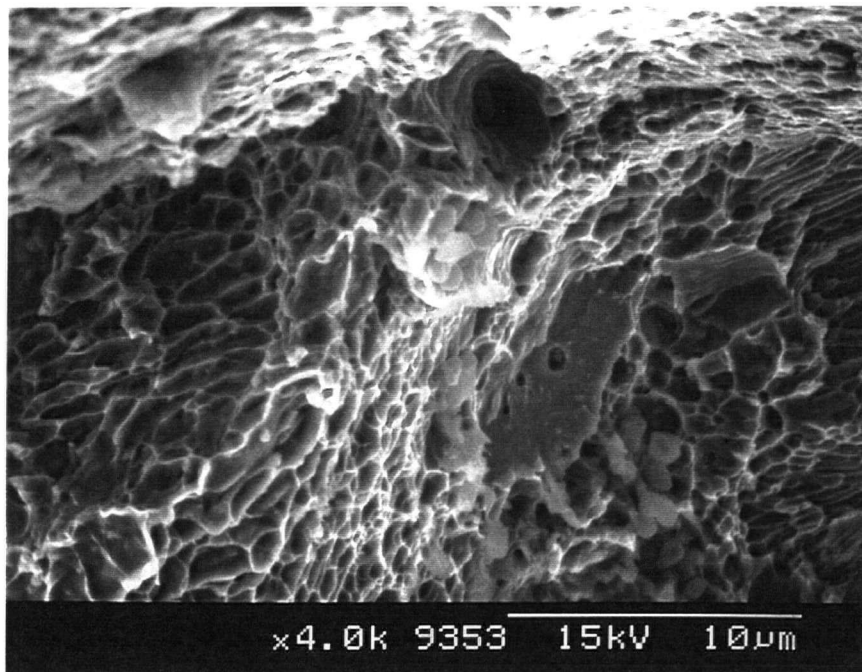


(b)

Figure 5.25 SEM fractographs showing fatigue cracking of spheroidized AISI 1070
(a) Buffered 3.5% NaCl, $E = -1.266 V_{SCE}$, before cleaning, $\Delta K \cong 11.5 \text{ MPa}\cdot\text{m}^{1/2}$, end of test
(b) Buffered 3.5% NaCl, $E = -1.266 V_{SCE}$, after cleaning, $\Delta K \cong 11.5 \text{ MPa}\cdot\text{m}^{1/2}$, end of test



(a)



(b)

Figure 5.26 SEM fractographs showing fatigue cracking of spheroidized AISI 1070
(a) Overload region, predominately cleavage fracture
(b) Overload region, microvoid coalescence regions.

6 Discussion

The susceptibility of eutectoid steel to cyclic environmental cracking was dependent upon the heat treatment. Stage-I crack propagation was transgranular and very sensitive to the microstructure. The presence of corrosion products inside the crack tends to decrease the crack propagation rate, particularly in the near-threshold region. This can only indicate that corrosion-product-induced closure was playing a dominant role in controlling the crack growth behavior of AISI 1070 steel in corrosive environments.

6.1 Stress state and plastic zone

The plane strain testing conditions at a crack tip are usually controlled by the thickness criterion [80] which is given by Equation (6.1):

$$t_B \geq 2.5 \left(\frac{K}{\sigma_y} \right)^2 \quad (6.1)$$

Where t_B is the specimen thickness above which plane strain conditions predominate and below which plane stress conditions become more dominant. Also, the value of K governing the minimum thickness criterion will be K_{max} under cyclic loading conditions. Using the relevant σ_y from Table 5.1; (541 MPa) for the pearlitic microstructure and (440 MPa) for the spheroidized microstructure, the testing conditions were analyzed for plane strain conditions under which $t_B =$ specimen thickness of the SEN specimens (12.7 mm). Using Equation (6.1) plane strain conditions were present in the AR condition when $K_{max} \leq 38.6 \text{ MPa.m}^{1/2}$, equivalent to $\Delta K \leq 19.3 \text{ MPa.m}^{1/2}$. This indicated that plane strain conditions prevailed when $\Delta K \leq 19.3 \text{ MPa.m}^{1/2}$, in the AR pearlitic condition. Therefore, all experimental data in the AR

condition, which were between ~ 2 and $\sim 17 \text{ MPa}\cdot\text{m}^{1/2}$, were sufficiently low that they may be considered to have been obtained under plane strain conditions. The edge of the crack front near the free surface will always tend to be under plane stress because of the inability of a free surface to sustain stresses normal to the surface. The stress state will determine the plastic zone size ahead of the crack tip [38-39]. Consequently, the plastic zone size gradually decreases from the plane stress size at the surface to the plane strain size in the interior, as shown in Figure 6.1.

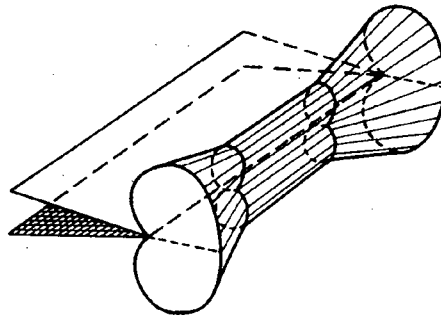


Figure 6.1 Three-dimensional plastic zone size [39].

The radius of the reversed plastic zone, Δr_y , under cyclic loading is given by the following Equation [138].

$$\Delta r_y = pC \left(\frac{\Delta K}{\sigma_y} \right)^2 \quad (6.2)$$

where p is equal to unity under plane stress conditions and has the value of 0.33 under plane strain conditions [139]. The product $pC = 0.05$ is used for plane strain conditions calculation. In the AR condition, for $\Delta K = 2.1, 4.0,$ and $10 \text{ MPa}\cdot\text{m}^{1/2}$, $\Delta r_y = 0.75, 2.7,$ and $17.1 \mu\text{m}$, respectively. This indicates that Δr_y values near-threshold are greater than the interlamellar

spacing by at least 4 times and always smaller than the austenite grain size ($\sim 55 \mu\text{m}$). At higher ΔK levels, Δr_y approached the pearlite colony size ($\sim 20 \mu\text{m}$).

A similar analysis for the spheroidized microstructure showed that plane strain predominated when $K_{\text{max}} \leq 31.4 \text{ MPa}\cdot\text{m}^{1/2}$, equivalent to $\Delta K \leq 15.6 \text{ MPa}\cdot\text{m}^{1/2}$. Therefore, most experimental data on HT specimens, which were between ~ 4 and $\sim 17 \text{ MPa}\cdot\text{m}^{1/2}$, were sufficiently low that they may be considered to have been obtained under plane strain conditions. Plane stress crack tip conditions became important at ΔK above $\sim 15.6 \text{ MPa}\cdot\text{m}^{1/2}$.

Plastic zone calculations from Equation (6.2) and $pC = 0.05$ for plane strain conditions showed that for $\Delta K = 4.0$ and $10 \text{ MPa}\cdot\text{m}^{1/2}$, $\Delta r_y = 4.1$ and $25.8 \mu\text{m}$, respectively. This indicates that at these ΔK values, the plastic zone size is greater than the cementite particle size ($0.5 \mu\text{m}$) and the interparticle spacing ($1.6 \mu\text{m}$).

6.2 General crack propagation characteristics

Fatigue crack propagation behavior in the AR and HT material in desiccated air, as illustrated in Figure 5.11, indicated that the spheroidized microstructure is more resistant to fatigue cracking than the lamellar microstructure. No crack retardation effects were evident in these curves, and it was possible to perform curve fitting analysis on the experimental data. The analysis indicated that both curves can be described by an empirical relationship of the form of Equation (2.5):

$$\frac{da}{dN} = C(\Delta K - \Delta K_{th}^*)^m \quad (6.3)$$

where C and m are experimental constants, and ΔK_{th}^* is a best fitting threshold stress intensity close to the experimentally observed ΔK_{th} . A satisfactory fit for AR & HT material was obtained and is given by Equations (6.4) and (6.5), respectively.

$$\left(\frac{da}{dN}\right)_{AR} = (7.9 \times 10^{-7})(\Delta K - 3.8)^{1.7}, \text{ mm/cycle} \quad (6.4)$$

$$\left(\frac{da}{dN}\right)_{HT} = (1.3 \times 10^{-7})(\Delta K - 3.8)^{2.2}, \text{ mm/cycle} \quad (6.5)$$

where ΔK has units of $\text{MPa}\cdot\text{m}^{1/2}$. The value of ΔK_{th}^* was found to be $\sim 3.8 \text{ MPa}\cdot\text{m}^{1/2}$ which is in agreement with the prediction of Equation (2.11) by Llorca *et al* [27] (i.e., $\Delta K_{th} = 5.54(1 - 0.62R)$). Equations of the same form as Equation (6.3) were found to give a good fit for the intergranular/transgranular fatigue cracking data of copper [138]. The above two Equations (6.4 and 6.5) along with the experimental data are presented in Figures 6.2 and 6.3, respectively.

6.3 Corrosion fatigue cracking model

The experiments show that a random distribution of carbides causes a noticeable decrease in the FCP rates. This behavior can be explained by the following arguments. Shear stresses in the ferrite matrix are not transferred effectively to the cementite in the spheroidized microstructure compared with the pearlitic microstructure. The cementite particles do not deform and act as obstacles to crack propagation, forcing the crack to move out of the microscopic crack plane to produce more ridges and a larger effective area of fracture surface per unit area of macroscopic crack plane. The increased area (implying a larger energy required for cracking), plus changing tensile component at the crack tip caused by crack

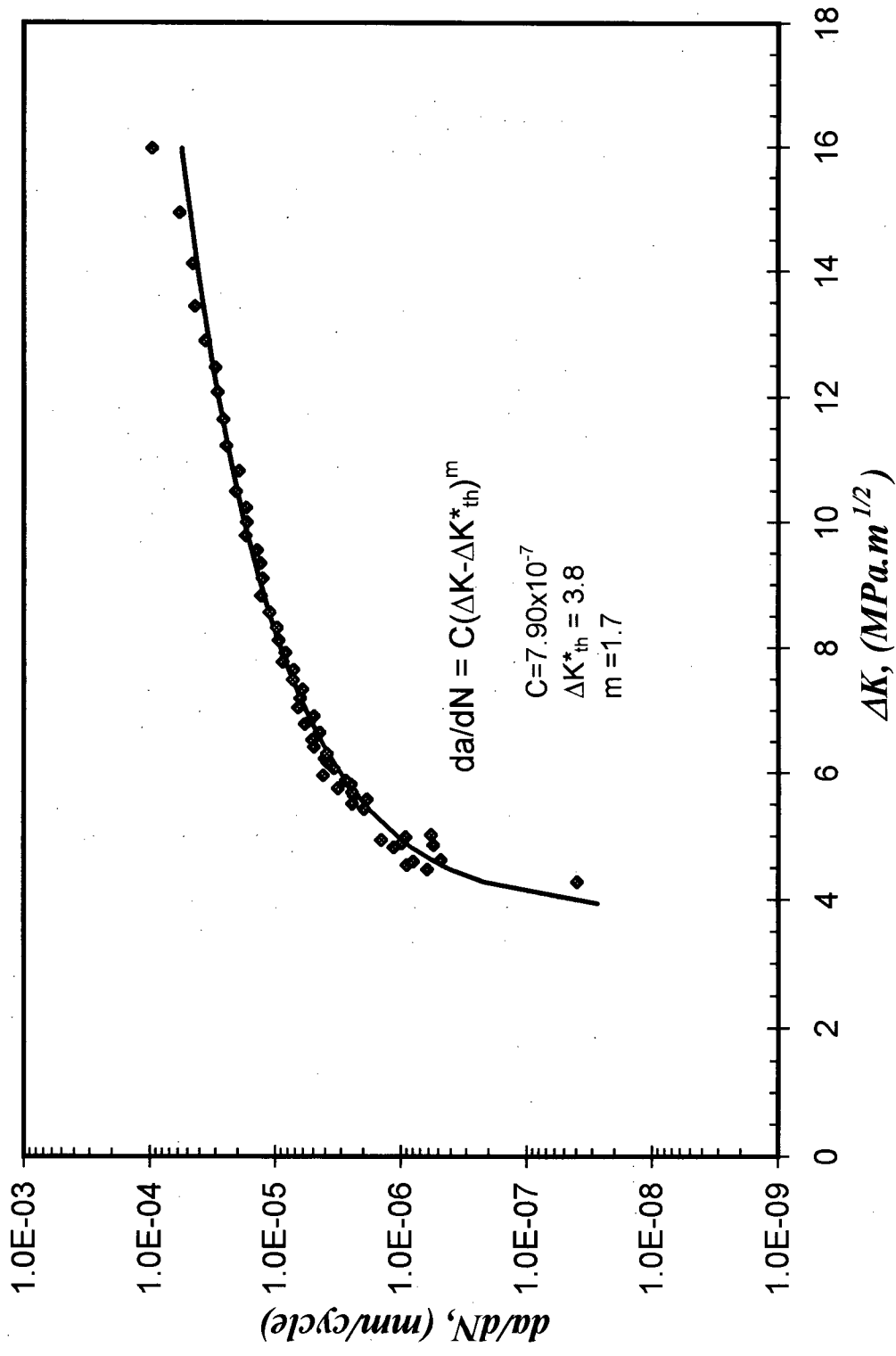


Figure 6.1 Curve fitting of experimental data in pearlitic AISI 1070 steel

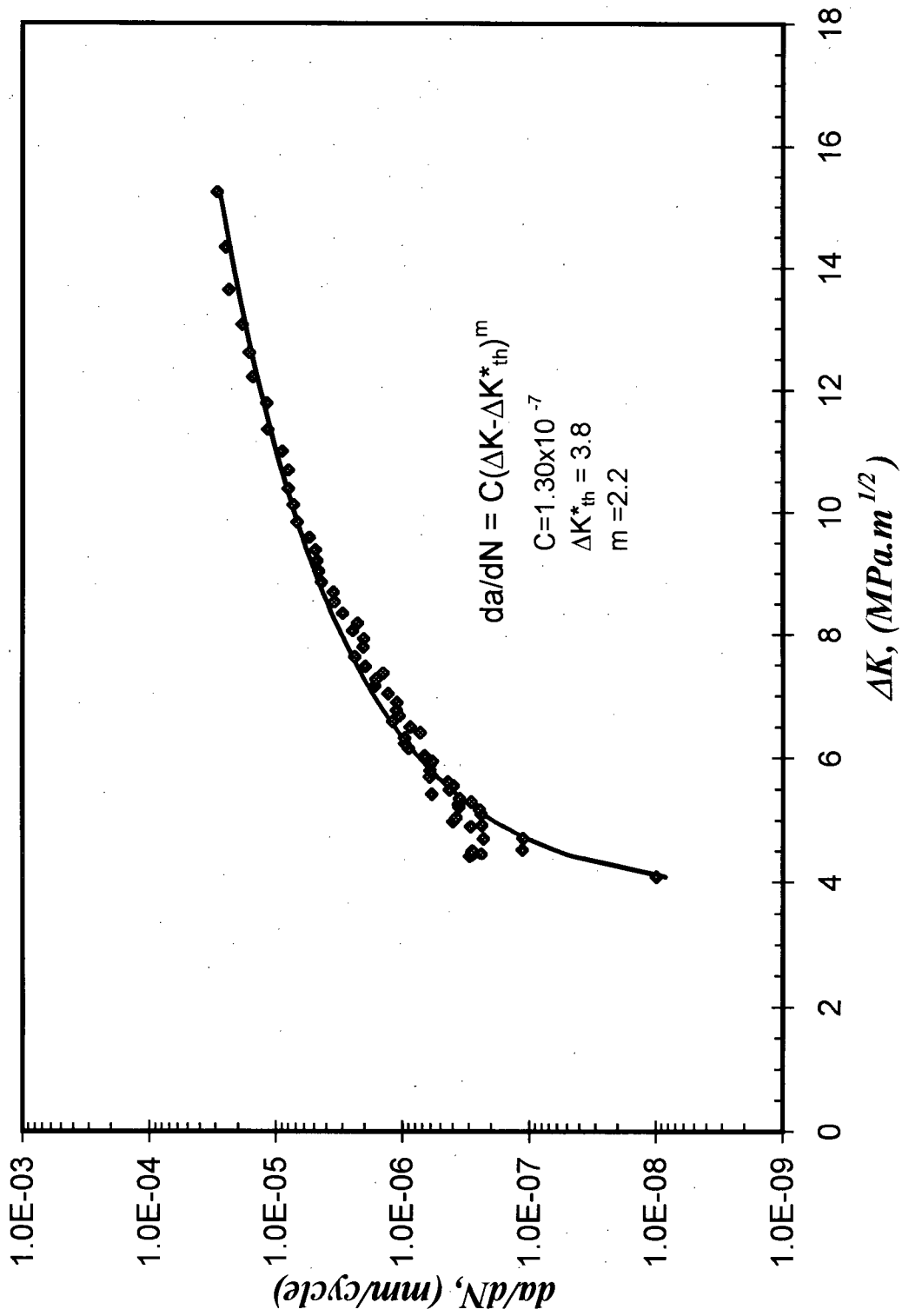


Figure 6.2 Curve fitting of experimental data in spheroidized AISI 1070 steel

deviations, promotes lower FCP rates. These configurations are pictorially demonstrated in Figure 6.4.

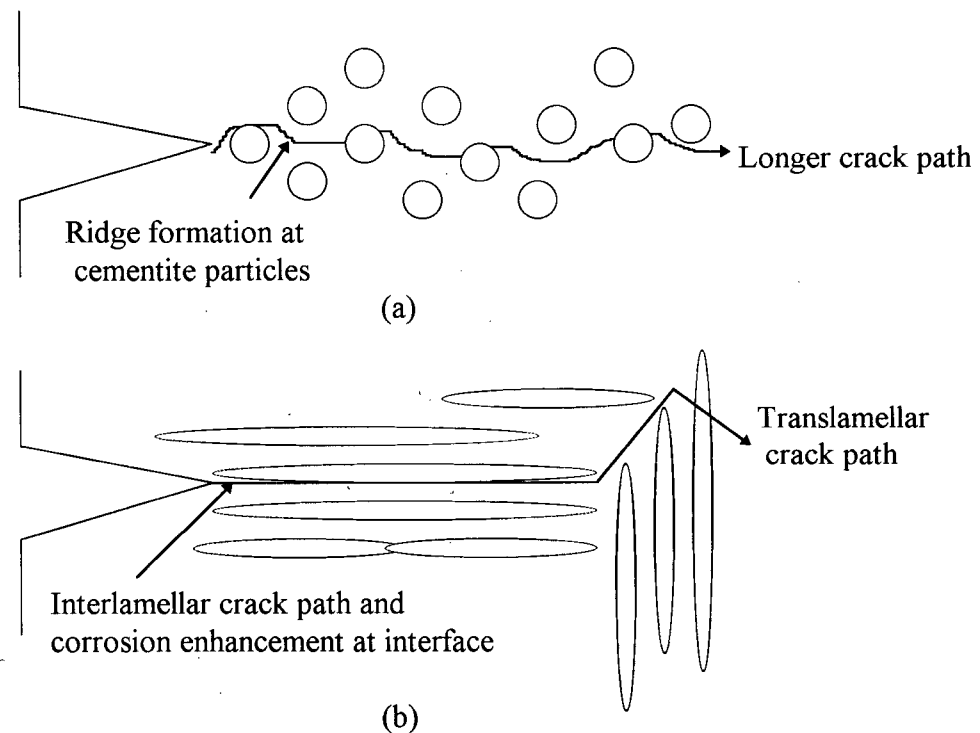


Figure 6.4 Schematic illustration showing a possible model for corrosion fatigue in eutectoid steel, (a) spheroidized microstructure, (b) pearlitic microstructure.

Padkin et al. [134] reported that deviations in the path of a crack would occur as it approaches a second phase particle of different modulus to the matrix. The analytical predictions showed that soft particles tend to attract cracks, while hard particles tend to deflect them. Using a ferrite matrix with either spheroidized cementite (hard) or spheroidal graphite (soft) as the second phase, these predictions have been largely verified experimentally [134]. However, the spheroidized carbides were unable to reinforce the ferrite matrix under pure tension as they did in pearlite. So, the same degree of work hardening for both microstructures was not observed in the tensile test.

The behavior in the pearlitic condition is perhaps more correctly described as a delamination process. Interlamellar as well as translamellar fracture through a colony may occur, depending on the orientation of the lamellae. Cementite lamellae can promote propagation by delamination in the case of a parallel orientation with the crack plane. On the other hand, they may be considered as an effective barrier to dislocation motion and thus, to crack propagation when they are perpendicular to the crack plane. For these reasons, the cracks may exhibit a “zigzag” type path, as was observed by Querales and Byrane [20] and also in the current study. The existence of ferrite rich regions at the prior austenite grain boundary act also as a preferential crack path. Cracking would tend to proceed along the direction of maximum shear stress imposed by the applied macrostress. Most investigators agree that a cleavage crack propagates along $\{100\}$ ferrite planes in pearlitic steels. The cementite in pearlite has also been observed to cleave. The cleavage planes of cementite have been recently determined to be $\{110\}$, $\{100\}$ or $\{210\}$ planes [109]. These prismatic planes have the common characteristics of low indices and low atomic density [126]. Similar mechanisms to the proposed model were reported by Garbarz and Pickering [118], Lesurer et al. [121], and Karlsson and Linden [123].

6.4 Corrosion fatigue crack propagation in the pearlitic microstructure

Fatigue striations are not readily visible in the pearlitic microstructure as shown in Figure 5.16. Such lack of consistent and homogeneously distributed visible fatigue striations in 1070 steel was also reported by Dougherty *et al.* [26]. The highest crack propagation rate measured

in the present study was $\sim 1 \times 10^{-4}$ mm/cycle which is around 1000 \AA . Assuming that striation spacing corresponds to crack advance per cycle, this increment length is still below the minimum resolution of the SEM fractographs obtained in this study, consistent with the observation by others [126].

A roughened texture was evident on the fracture surfaces, especially under the mirror stereoscope. Such topography, observed previously by Richards and Lindley [124] in a coarse pearlitic steel, was named as "*microcleavage*". It was also stated that fatigue cracking of pearlitic steels does not propagate by a ductile striation mechanism.

6.4.1 Effect of microstructure

Fatigue crack growth rates obtained in this study are nearly comparable to the results from a different specimen geometry test in air of AISI 1080 steel [19, 21, 23]. Figure 5.10 summarizes the experiments done on the AR material. One can construct qualitative rationales for these curves by appropriately considering such factors as the effect of rapid dissolution, potential, and microstructure on FCP rates. It should be pointed out that the fatigue crack is always propagating through a localized plastic zone and the microstructure in this zone is expected to influence the FCP rate. The interface between the Fe/Fe_3C lamellae is likely to provide an easier crack propagation path so that delamination processes may play a dominate role in FCP (see 6.3).

6.4.2 Role of environment

Generally, crack growth rates in the aqueous environments were lower than the rates in desiccated air at equivalent ΔK levels. It was observed that corrosion products and gas

bubbles were constantly pumped out of the crack during propagation, especially at freely corroding conditions in 3.5% *NaCl*. Fatigue crack retardation phenomena were very pronounced in the near-threshold regions in 3.5% *NaCl*, consistent with corrosion-product-induced retardation effects. In contrast, specimens fatigued in desiccated air showed very clean surfaces, consistent with the absence of corrosion products, and exhibited higher FCP rates consistent with no retardation effects.

Fatigue behavior of the AR material in freely corroding 3.5% *NaCl*, Figure 5.7, suggests that active corrosion and the subsequent corrosion-products-induced closure may be beneficial to crack propagation resistance but detrimental to crack initiation and ΔK_{th} . The corrosion-products-induced closure has been interpreted in terms of a reduction in the effective crack-driving force or ΔK_{eff} through the presence of corrosion products on the crack surfaces, which cause contact between opposing fracture surfaces before K_{min} is reached. Therefore, ΔK_{eff} value at the crack tip is less than the nominal ΔK calculated from Equations (4.1) to (4.4).

It is noteworthy that the effectiveness of cathodic protection was obvious from the increase in the ΔK_{th} value compared to the unprotected (freely corroding) condition. However, the presence of corrosion products on the central region of the fracture surface indicated incomplete cathodic protection due to non-uniform current distribution within the crack.

Comparing the active and passive systems, the buffered solution promoted passivation and an accompanying decrease in the dissolution rate. This should lead to a decreased crack propagation rate if anodic dissolution at the crack tip is contributing to cracking. However, it was noticeable that the cracking rates were higher in the passive environment, which indicate that the corrosion-product-induced closure effect in the freely corroding, unbuffered solution

exerted a more dominate effect. That is to say, the observed effects of environment (pH) on da/dN do not come from differences in anodic dissolution rates, but are due to differences in the amount of corrosion products (i.e., corrosion-product-induced closure effects) inside the crack.

The steel exhibited passivity in the buffered solution (pH=10.5). Under passive conditions, film rupture at the crack tip may play a critical element in the mechanism of corrosion fatigue cracking. A high local anodic current density could result from galvanic coupling between the bare surface at the crack tip and the surrounding film-covered passive surfaces [126]. The presence of the Cl^- ion species is critical, and retards repassivation for a sufficient time, causing a large degree of dissolution at the crack tip [126]. These effects may account for the higher FCP rates in the buffered solution relative to unbuffered $NaCl$ solution (pH=6.0).

6.4.3 Dissolution phenomena and cracking rates

The lowest ΔK_{th} , $2.1 \text{ MPa}\cdot\text{m}^{1/2}$, was obtained in the pearlitic microstructure under freely corroding test conditions in 3.5% $NaCl$. If it is assumed that the low threshold value is caused solely by dissolution-induced crack propagation, the required anodic current density at the crack tip (i_{ct}) will be related to the crack velocity (da/dt) via Faraday's law according to Equation (6.6)

$$\frac{da}{dt} = \frac{(i_{ct}W)}{F\rho} \quad (6.6)$$

where F is the Faraday (96500 C), ρ is the density of iron (7.86 gm/cm^3), and W is the equivalent weight of iron ($27.9 \text{ gm for Fe}^{2+}$).

At threshold, $da/dN \cong 10^{-8}$ mm/cycle, and the cyclic frequency (f) was ~ 100 Hz. Therefore, $da/dt \approx 10^{-7}$ cm/sec and Equation (6.6) then shows that the required i_{ct} becomes 2.72×10^{-3} A/cm² (27.2 A/m²). This current density will account for a crack propagation rate of 10^{-7} cm/sec. Comparison with the experimental polarization curve (see Figure 5.5) shows that the measured value of i at the monitored E_{corr} (~ 0.6 V_{SCE}) during fatigue testing (see Table 5.3) was ~ 0.0316 A/m². Hence, the required i_{ct} obtained from Equation (6.6) is extremely large ($\sim 10^3$ times) compared with the measured value, and is unlikely to be operative at the crack tip under normal circumstances. Consequently, the observed crack growth at the lower ΔK_{th} values in 3.5% NaCl solution could be due to a synergism between the cyclic load and dissolution processes that result in higher cracking rates.

A stressed crack undergoes a plastic stretching effect at the crack tip, known as a crack tip opening displacement, d , which may be calculated from Equation (6.7) [39],

$$d = \frac{4}{\pi} \frac{K^2}{E_m \sigma_y} \quad (6.7)$$

where E_m is the elastic modulus of the material.

Therefore, applying Equation (6.7) to the threshold conditions for the pearlitic (AR) steel fatigued under freely corroding conditions in 3.5% NaCl, $K = (K_{max})_{th} = 4.2$ MPa.m^{1/2}. After substituting for $\sigma_y = 541$ MPa, $E_m \cong 200 \times 10^3$ MPa, then $d = 2.1 \times 10^{-7}$ m. Consequently, the total plastically stretched area (A_{ct}) of the opened crack tip will be $A_{ct} = d \cdot B$, where B is the specimen thickness (12.7 mm). Thus, $A_{ct} = 2.63 \times 10^{-9}$ m². Similarly, the area of the precrack surface (A_{pc}) will be: $A_{pc} = 2 a B$, where a is the crack length ($a = 22.55$ mm in this case). Thus, $A_{pc} = 5.73 \times 10^{-4}$ m² and $A_{ct}/A_{pc} = 4.6 \times 10^{-6}$.

Assuming that the current density at the crack tip (i_{ct}) is 1000 times that at the precrack surface (i.e. $i_{ct}/i_{pc}=1000$) due to an increase in the number of active dissolution sites on the continuously forming slip steps at the cyclically deforming crack tip, then the I_{ct}/I_{pc} becomes,

$$\frac{I_{ct}}{I_{pc}} = \frac{i_{ct} \cdot A_{ct}}{i_{pc} \cdot A_{pc}} = \left(\frac{A_{ct}}{A_{pc}} \right) \times 10^3 \quad (6.8)$$

Therefore, $I_{pc}/I_{ct} = 2.2 \times 10^2$ (i.e. $I_{pc} \gg I_{ct}$) and the total anodic current after stressing will be:

$$I_{anodic} = I_{pc} + I_{ct} \approx I_{pc} \quad (6.9)$$

Figure 6.5 shows a schematic theoretical polarization diagram showing the possible corrosion process at the crack tip and the surrounding precrack surfaces. Consequently, because $I_{pc} \gg I_{ct}$, there will be no observed effect of stress (ΔK) on E_{corr} even though $i_{ct} \gg i_{pc}$.

Note that enhanced dissolution of the iron (ferrite) at the crack tip will tend to produce dissolution slots between Fe_3C lamellae in the pearlite. These slots may enhance crack propagation (lower ΔK_{th}) by initiating cracking along the planar ferrite/ Fe_3C interface. Such slotting and interfacial separation effect would be absent in the spheroidized microstructure and may explain why ΔK_{th} is higher for the HT material when tested in 3.5% NaCl solution.

I_{cp} = Corrosion current on precrack surface

E_{ox} = Reversible potential of oxidant

I_{ct} = Corrosion current on crack tip, before stressing.

E_{pc} = Reversible potential of precrack surface.

E_{ct} = Reversible potential of crack tip.

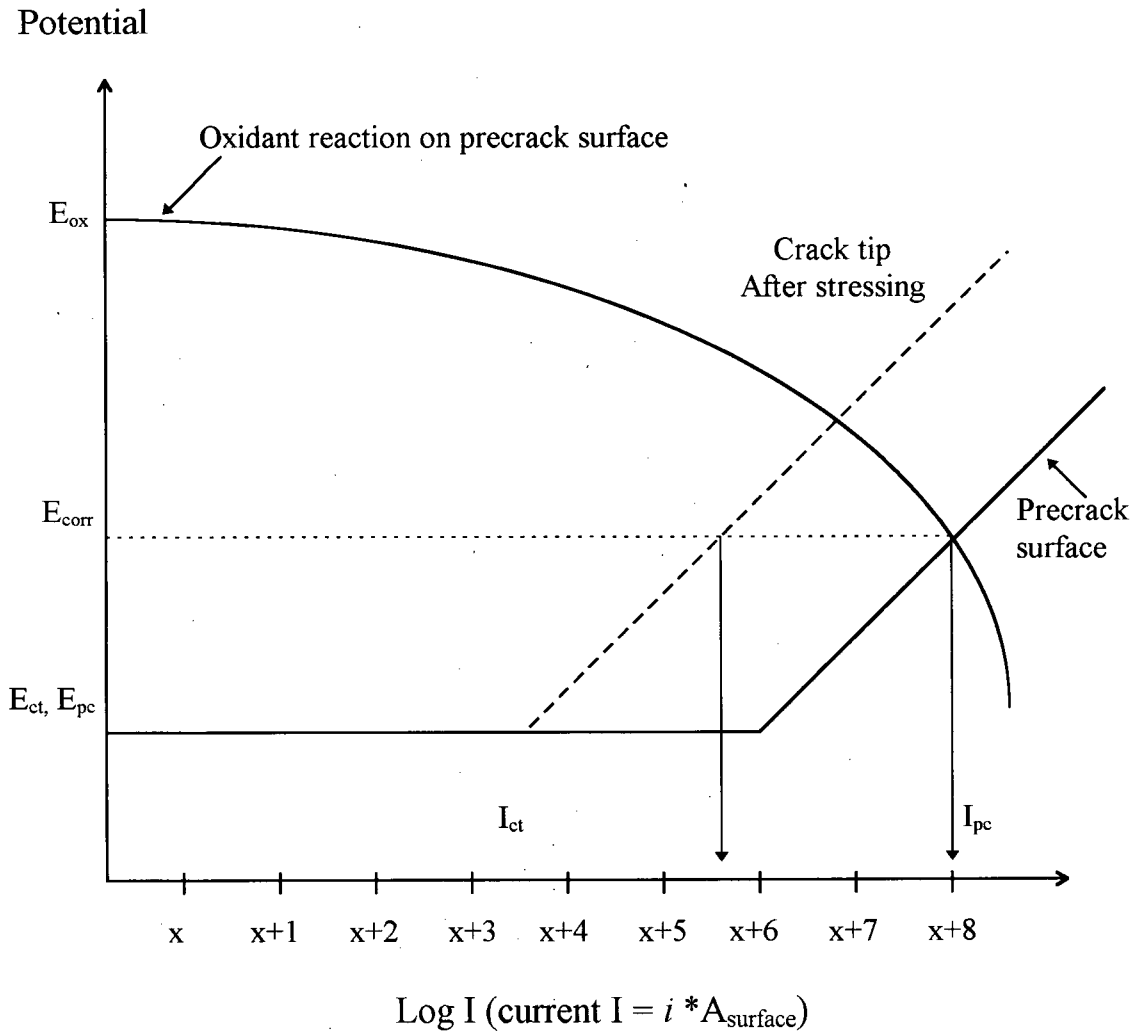


Figure 6.5 Schematic theoretical polarization diagram showing possible anodic processes at crack tip and precrack surfaces

6.5 Corrosion fatigue crack propagation in the spheroidized microstructure

6.5.1 Effect of microstructure

The major effect of microstructure is the absence of planar interfaces (preferred crack path) between the ferrite/cementite lamellae. These effects were discussed previously in section 6.3.

The fractography of specimens at the end of the fatigue test indicated that cracking was mainly in the ferrite matrix while cementite particles were unaffected. Wang and Lei [114] found that the cementite particles in the spheroidized steel were not easily deformed and only changed their position and orientation as the ferrite matrix was deformed.

6.5.2 Role of environment

The most pronounced crack arrest and retardation phenomena occurred in the HT microstructure when tested in the 3.5% *NaCl* solution polarized to $-1.0 V_{SCE}$ (Figure 5.13). In this test condition, the electrochemical dissolution of the metal was minimized by the applied cathodic protection and could not contribute in any significant manner to crack advancement.

HT crack propagation rates in the buffered 3.5% *NaCl* solution at a cathodic potential of $-1.266 V_{SCE}$ were higher than that in desiccated air at low ΔK levels (Figure 5.12). Then, as the ΔK increased, the two curves converged to similar rates of propagation. Hydrogen was produced at the steel surface during cathodic polarization and sodium tetraborate, which was used to buffer the solution, has been reported to activate hydrogen generation at the crack tip

under cyclic loading conditions [122] and to stimulate corrosion-mechanical fracture. Therefore, the availability of hydrogen for absorption at the crack tip is believed to be higher in this test condition. It is now proposed that the increased crack propagation rates under cathodic polarization condition in the buffered *NaCl* solution are due to a hydrogen embrittlement mechanism.

6.5.3 Effect of hydrogen

Under cathodic polarization conditions, H^+ ions are reduced to hydrogen which first forms as an adsorbed species, H_{ad} , on the metal surface. Most of the H_{ad} species combine to form molecular hydrogen ($2H_{ad} \rightarrow H_2$) and a smaller fraction becomes absorbed into the metal lattice as atomic hydrogen (H). If the lattice hydrogen produces a hydrogen embrittlement effect that contributes to fatigue crack propagation, then it is important to estimate the approximate distance, x , that hydrogen is able to diffuse into the metal lattice at the crack tip during one cycle. The distance (x) may then be compared with the average crack growth increment per cycle, da/dN .

Assuming that the absorbed atomic hydrogen concentration, C_s , is constant in the subsurface at the crack tip, then the concentration of hydrogen, C_x , at a distance x ahead of the crack tip after time (t) is given by Equation (6.7) [140]:

$$C_x = C_s \left[1 - \operatorname{erf} \left(\frac{x}{2\sqrt{Dt}} \right) \right] \quad (6.10)$$

where D is the diffusion constant for monatomic hydrogen in the metal lattice. Also, error function tables [140], show that $C_x \approx 0.5 C_s$ when:

$$x \approx (Dt)^{1/2} \quad (6.11)$$

Equation (6.11) gives a reasonable estimate of the distance at which a significant concentration of hydrogen is present in the metal lattice. Hirth [135] showed that the value of D in steel is temperature dependent according to the following expression:

$$D = 2.0 \times 10^{-7} \exp -(828/T) \quad , \quad m^2/s \quad (6.12)$$

where T is in K. At room temperature, $D \sim 1.2 \times 10^{-8} \text{ m}^2/\text{sec}$. When (t) is equal to the period of one cycle ($\sim 0.01 \text{ s}$ at $\sim 100 \text{ Hz}$), x is equal to $1.1 \times 10^{-5} \text{ m}$, which is greater than the cyclic plastic zone size at ΔK_{th} (see 6.1) and larger than any da/dN value obtained during the fatigue studies. The calculation suggests that the diffusion of hydrogen during each load cycle is sufficiently rapid to influence cracking within the crack tip plastic zone. However, it provides no information on the actual hydrogen concentration. In fact, considerable trapping of H is expected at Fe/Fe_3C interfaces which reduces the concentration of H in the lattice [135].

From Figure 5.12, the crack growth rate during hydrogen charging was higher than that in air from $\Delta K \sim 5$ to $\sim 9 \text{ MPa}\cdot\text{m}^{1/2}$, corresponding to da/dN of $\sim 3.7 \times 10^{-7}$, and $\sim 4.6 \times 10^{-6} \text{ mm/cycle}$, respectively. It is now clear, that the increase in crack growth rate may be attributed to hydrogen-related embrittlement effects.

The absence of pronounced hydrogen effects in the pearlitic microstructure is attributed to the weakness of the planar Fe/Fe_3C interface in the pearlite, which dominates over hydrogen effects and, perhaps, to the larger interfacial area available for trapping of hydrogen (which reduces the concentration of hydrogen in the metal lattice) [135].

6.6 Industrial applications of the reported data

The results in this study revealed that spheroidizing of eutectoid steel could alleviate the corrosion fatigue problem. It was noticeable that the spheroidized microstructure had a higher ΔK_{th} values in all aqueous environments. It may be possible to state that such a result is very significant for practical applications. However, some limitations exist. For example, Table (5.1) shows that the spheroidized microstructure has a lower tensile strength than the pearlitic condition. In the case where tensile properties are the controlling design parameter, pearlitic steels would be more preferable than the spheroidized material. Another limitation for the spheroidized microstructure is its susceptibility to hydrogen embrittlement relative to the pearlitic condition. Clearly, much more needs to be done in this area before any definitive recommendation can be drawn.

7 Summary and Conclusions

Studies of the corrosion and corrosion fatigue behavior of AISI 1070 steel in controlled environments of: desiccated air, distilled water, 3.5% *NaCl* (pH=6.0) and buffered 3.5% *NaCl* (pH=10.5), are consistent with the following conclusions:

1. Eutectoid steel does not passivate in 3.5% *NaCl* solution and exhibits passivity at pH = 10.5.
2. The minimum and maximum ΔK_{th} values in the pearlitic condition were 2.1 and 4.3 MPa.m^{1/2}, while in the spheroidized condition they were 3.9 and 4.1 MPa.m^{1/2}, respectively. ΔK_{th} varied with test environment as following:

$$\Delta K_{th (3.5\% NaCl)} < \Delta K_{th (Buffered 3.5\% NaCl)} < \Delta K_{th (distilled water)} < \Delta K_{th (desiccated air)}$$

3. Both pearlitic and the spheroidized microstructures exhibited Paris power law behavior in stage-II, where $da/dN = A (\Delta K)^n$. In desiccated air, stage I and II behavior could be described by a relationship of the form $da/dN = C (\Delta K - \Delta K_{th}^*)^m$.
4. Fatigue crack retardation phenomena were observed in the aqueous environments in most of the fatigue tests. The cause of this retardation was attributed mainly to corrosion product-induced crack closure effects, which reduced the effective crack tip cyclic stress intensity ΔK_{eff} .

5. The spheroidized microstructure is more resistant to fatigue cracking than lamellar (pearlitic) microstructures. It also showed better resistance to crack initiation, and higher ΔK_{th} value in the saline environment.

6. Cathodic protection appeared to be beneficial, to some extent, only in 3.5% *NaCl* solution (pH = 6.0) for both microstructures. It was effective in achieving a higher ΔK_{th} value compared with the unprotected condition.

8 References

1. Metals Handbook, Volume 13, Ninth Edition, *Corrosion*, ASM International, 1987.
2. McEvily, A.J., Jr., *Atlas of Stress-Corrosion and Corrosion Fatigue Curves*, ASM International, 1990, pp. 29-254.
3. Crooker, T.W. and B. N. Leis, Eds., *Corrosion Fatigue: Mechanics, Metallurgy, Electrochemistry & Engineering*, ASTM STP 801, American Society for Testing and Materials, 1983.
4. Devereux, O., A. J. McEvily, and R. W. Staehle, Eds., *Corrosion Fatigue: Chemistry, Mechanics and Microstructure*, NACE 2, 1972.
5. Lisagor, W. B., T. W. Crooker, and B. N. Leis, Eds., *Environmentally Assisted Cracking: Science and Engineering*, ASTM STP 1049, American Society for Testing and Materials, 1990.
6. Carpinteri, A., Ed., *Handbook of Fatigue Crack Propagation in Metallic Structures*, Vol. I and II, Elsevier Science B. V., 1994.
7. Scott, P. and R. A. Cottis, *Environment Assisted Fatigue*, EGF Publication 7, The Institution of Mechanical Engineers, 1990.
8. Miller, K. J. and E.R. de los Rios, *Short Fatigue Cracks*, ESIS Publication 13, European Structural Integrity Society, 1992.
9. Jaske, C. E., J. H. Payer, and V. S. Balint, *Corrosion Fatigue of Metals in Marine Environments*, MCIC Report, Battelle's Columbus Laboratories, 1981.
10. Goel, V. S., Ed., *Fatigue Life Analysis and Prediction*, Proc. of Intl. Conf. And Exposition on Fatigue, Corrosion Cracking , Fracture Mechanics and Failure Analysis, Salt Lake City, Utah, 1985, ASM, 1986.
11. Parkins, R. N., and Ya. M. Kolotyrkin, *Corrosion Fatigue*, Proc. Of 1st. USSR-UK Seminar on Corrosion Fatigue of Metals, Lvov, USSR, May 1980, The Metals Society 1983.
12. Ritchie, R. O., and J. Lankford, Eds., *Small Fatigue Cracks*, Proc. Of 2nd Engineering Foundation Intl. Conference, Santa Barbara, California, Jan. 1986, AIME, The Metallurgical Society, Inc., 1986.

13. Kreutzer, R. and B. Zwirn, *The Attributes and Markets of High-Carbon Steel Wire*, Wire Technology, vol. 9, No. 6, pp. 60-61, Nov. 1981
14. Elices, M., J. Llorca, and M.A. Astiz, "Fatigue of steels for concrete reinforcement and cables," see ref. 6, pp. 191-220.
15. Lewandowski, J.J., and A.W. Thompson, "Microstructural Effects on the Cleavage Fracture Stress of Fully Pearlitic Eutectoid Steel," *Metall. Trans. A*, vol. 17A, No. 10, 1986, pp. 1769-1786.
16. MacKenzie, B.A., *The Attributes of High-Carbon Steel Wire*, Mod. Mach. Shop, vol. 54, no. 9, pp. 94-101, Feb. 1982
17. Bae, C. M., W. J. Nam, and Chong S. Lee, "Effect of Interlamellar Spacing on the Delamination of Pearlitic Steel Wires," *Scripta Materialia*, Vol. 35, No. 5, 1996, pp. 641-646.
18. Alexander, D.J., and I.M. Bernstein, "Cleavage Fracture in Pearlitic Eutectoid Steel," *Metall. Trans. A*, vol. 20A, no. 11, 1989, pp. 2321-2335.
19. Lewandowski, J.J., and A. W. Thompson, "Effects of the Prior Austenite Grain Size on the Ductility of Fully Pearlitic Eutectoid Steel," *Metall. Trans. A*, vol. 17A, No. 3, 1986, pp. 461-472.
20. Querales, A. and J. G. Byrne, "Effects of Thermomechanical Treatments on the Mechanical Behavior of Eutectoid Steel," *Metall. Trans. A*, vol. 11A, No. 2, 1980, pp. 255-266.
21. Daeubler, M. A., and A. W. Thompson, "Microstructural Effects on Short Fatigue Cracks in Eutectoid Steels," see ref. 12, pp. 157-164.
22. Kao, P.W., and J.G. Byrne, "Fatigue Initiation Study of TMT Eutectoid Steel," *Metall. Trans. A*, vol. 13A, no. 5, 1982, pp. 855-864.
23. Daeubler, M. A., A. W. Thompson, and I. M. Bernstein, "Influence of Microstructure on Fatigue Behaviour and Surface Fatigue Crack Growth of Fully Pearlitic Steels," *Metall. Trans. A*, Vol. 21A, No. 4, 1990, pp. 925-933.
24. Martin, A., V. Sanchez-Galvez, and J. Llorca, "Corrosion Fatigue of Cold Drawn Eutectoid Steel Wires in Artificial Seawater," see ref. 7, pp. 435-447.
25. Gilcharist, J. D., and R. Narayan, "Environmental Cracking of Eutectoid Steel," *Corrosion Science*, Vol. 11, 1971, pp. 281-296.

26. Dougherty, J. D., T. S. Srivatsan and J. Padovan, "Cyclic Stress Response, Strain Resistance and Fracture Behavior of Modified 1070 Steel," *Engineering Fracture Mechanics*, Vol. 53, No. 6, 1996, pp. 829-847
27. Llorca, J., and V. Sanchez-Galvez, "Fatigue Threshold Determination in High Strength Cold Drawn Eutectoid Steel Wires," *Engineering Fracture Mechanics*, Vol. 26, No. 6, 1987, pp. 869-882.
28. Cabral, A., A. W. Thompson, I. M. Bernstein and D. H. Stone, "The Thermal Fatigue Behavior of Near-eutectoid Steel," *Materials Science and Engineering*, Vol. 93, 1987, pp. 73-82.
29. Sunwoo, H., M. E. Fine, M. Meshii, and D. H. Stone, "Cyclic Deformation of Pearlitic Eutectoid Rail Steel," *Metall. Trans A*, vol. 13A, no. 11, 1982, pp. 2035-2047.
30. Prakash, A., D. K. Kim, and R. M. Shemanski, "Fatigue Behavior of Wire and Cable," see ref. 10, pp. 405-408.
31. Husain, Z., and R. A. Cottis, "The Influence of Seawater Corrosion on the Fatigue Strength of Steel Wire Rope," in *Fatigue of Engineering Materials and Structures*, Vol. II, Proc. Of the Institution of Mechanical Engineers, University of Sheffield, 1986.
32. Gray, G. T. III, J. C. Williams, and, A. W. Thompson, "Roughness-Induced Crack Closure: An Explanation for Microstructurally Sensitive Fatigue Crack Growth," *Metall. Trans. A*, Vol. 14A, 1983, pp. 421-433.
33. Gray, G. T. III, A. W. Thompson, and J. C. Williams, "The Effect of Microstructure on Fatigue Crack Path and Crack Propagation Rate" in *Fatigue Crack Growth Threshold Concepts*, David Davidson and Subra Suresh, Eds., The Metallurgical Society of AIME, 1984, pp. 131-143.
34. Hertzberg, R.W., *Deformation and Fracture Mechanics of Engineering Materials*, 2nd edition, John Wiley & Sons, 1983, pp. 233-627.
35. Jones, Denny A., *Principles and Prevention of Corrosion*, Macmillan Publishing Company, 1992.
36. Bamford, W. H., "Implementing Corrosion-Fatigue Crack Growth Rate Data for Engineering Applications," see ref. 3, pp. 405-422.
37. Bannantine, J. A., J. J. Comer and J. L. Handrock, *Fundamentals of Metal Fatigue analysis*, Prentice Hall, 1990
38. Broek, D., *The Practical Use of Fracture Mechanics*, Kluwer Academic Publishers, 1989.

39. Broek, D., *Elementary Engineering Fracture Mechanics*, Martinus Nijhoff Publishers, The Hague, 1982.
40. Wei, R. P., And Shim, G., "Fracture Mechanics and Corrosion Fatigue," see ref 3, pp. 5-25.
41. McEvily, A. J., and R. P. Wei, "Fracture Mechanics and Corrosion Fatigue," see ref. 4, pp. 381-395.
42. Suresh, S., *Fatigue of Materials*, Cambridge University Press, 1991.
43. Throop, J. F., and H. S. Reemsnyder, *Residual Stress effects in Fatigue*, ASTM Symposium, Phoenix, Ariz, May 1981, ASTM STP 776, 1982.
44. Scott, P. M., "Chemistry Effects in Corrosion Fatigue," see ref. 3, pp. 319-350.
45. Kerr, J., R. Holmes and G.M. Brown, " Corrosion Fatigue of Large Welded Tubular Joints," see ref. 7, pp. 3-15.
46. Ouchi, H., I. Soya, R. Ebara and Y. Yamada, "Effects of Temperature and Dissolved Oxygen in Seawater on the Fatigue Strength of Welded Steel Joints," see ref. 7, pp. 17-30.
47. Brown, B. Floyd, "Effects of Cathodic Protection on Corrosion Fatigue," see ref. 3, pp. 508-515.
48. Monahan, C. C., and R. M. Hopkins, " The Relative Severity of Natural and Synthetic Seawaters on the Fatigue Behavior of Cathodically Protected Steel," see ref. 7, pp. 97-122.
49. Mayaki, M. C., and J. E. King, "Corrosion Fatigue Crack Propagation in a Duplex Stainless Steel," see ref. 7, pp. 155-171.
50. Bignonnet, A., J. Petit, and A. Zegloul, "The Influence of Environment on Fatigue Crack Growth Mechanisms," see ref. 7, pp. 205-222.
51. Austen, I.M., "Quantitative Understanding of The Effects of Mechanical and Environmental Variables on Corrosion Fatigue Crack Growth Behavior," in *The Influence of Environment on Fatigue*, Conference: The Institution of Mechanical Engineers, London, 1977
52. Bernard, P.J., T.C. Lindley and C.E. Richards, "Mechanisms of Overload Retardation During Fatigue Crack Propagation" , in *Fracture Crack Growth Under Spectrum Loads*, ASTM STP 595.

53. Paris, P. C., and F. Erdogan, "A Critical Analysis of Crack Propagation Laws," *Trans. ASME, J. Basic Eng.*, Vol D85, 1963, pp. 528-534.
54. Krauss, George, "Physical Metallurgy and the Heat Treatment of Steel," in *Metals Handbook, Desk Edition*, Howard E. Boyer and Timothy L. Gall, Eds., American Society for Metals, 1985, pp. 28.1-10.
55. Shinglederker, Ross B., "Heat Treating of Steel," in *Metals Handbook, Desk Edition*, Howard E. Boyer and Timothy L. Gall, Eds., American Society for Metals, 1985, pp. 28.11-21.
56. Ritchie, R. O., "Near-threshold Fatigue-crack Propagation in Steels," *Intl. Metals Reviews*, No. 5&6, 1979, pp. 205-230.
57. Wei, R. P., and M. O. Speidel, "Phenomenological Aspects of Corrosion Fatigue, Critical Introduction," see ref. 4, pp. 379-380.
58. Fong, C., *High Frequency Near-Threshold Corrosion Fatigue of AISI 316L Stainless Steel*, M.A. Sc. Thesis, The University of British Columbia, 1985.
59. Fong, C., and D. Tromans, "High Frequency stage I Corrosion Fatigue of Austenitic Stainless Steel (316L)," *Metall. Trans. A*, Vol. 19A, 1988, pp. 2753-2773.
60. Chen, Xiande, *Fatigue Crack Propagation in Al-Li Alloy 8090 - Environmental Effects*, Ph. D Thesis, The University of British Columbia, 1994.
61. Chen, Xiande, and D. Tromans, "Fatigue Crack Propagation in 8090 Al-Li Alloy - Environmental Effects," *Mater. Sci. & Eng.*, Vol. A189, 1994, pp. 45-59.
62. Elber, W., "Fatigue Crack Closure Under Cyclic Tension," *Eng. Fract. Mech.*, Vol. 2, 1970, pp. 37-45.
63. Suresh, S., and R. O. Ritchie, "Near-Threshold Fatigue Crack Propagation: A Perspective on the Role of Crack Closure," in *Fatigue Crack Growth Threshold Concepts*, David Davidson and Subra Suresh, Eds., The Metallurgical Society of AIME, 1984, pp. 227-261.
64. Taylor, D., *Fatigue Thresholds*, Butterworth & Co. Ltd., 1989.
65. Wang, Z. F., J. Li, J. Q. Wang and W. KE, "The Influence of Loading Waveform on Corrosion Fatigue Crack Propagation," *Corrosion Sci.*, Vol. 37, No. 10, 1995, pp. 1551-1565.

66. Tanaka, Masazumi, "The Influence of Aqueous Environments on Low ΔK and High ΔK Fatigue Crack Propagation Behavior in Low Carbon Structural Steel," *Metall. Trans. A*, Vol. 27A, 1996, pp. 2678-2685.
67. Sprowls, D. O., "Evaluation of Corrosion Fatigue," see ref. 1, pp. 291-302.
68. Sequeira, C. A. C., and A. K. Tiller, Eds., *Microbial Corrosion -1*, Elsevier Science Publishers Ltd., 1988.
69. Tada, H., P. C. Paris and G. R. Irwin, *The Stress Analysis of Cracks Handbook*, Del Research Corp., Hellertown, PA, 1973, pp. 2.10-2.11.
70. Hawbolt, E. B., B. Chau, and J. K. Brimacombe, "Kinetics of Austenite-Pearlite Transformation in Eutectoid Carbon Steel," *Metall. Trans. A*, Vol. 14A, 1983, pp. 1803-1815.
71. Agarwal, P. K., and J. K. Brimacombe, "Mathematical Model of heat Flow and Austenite-Pearlite Transformation in Eutectoid Carbon Steel Rods for Wire," *Metall. Trans. B*, Vol. 12B, 1981, pp. 121-133.
72. Riehm, D. J., *Kinetics of The Pearlite to Austenite Reversion Transformation*, M.A.Sc. Thesis, The University of British Columbia, 1990.
73. Pajagopalan, I. J., *Mathematical Modeling of Phase Transformation in a Plain Carbon Eutectoid Steel*, M.A.Sc. Thesis, The University of British Columbia, 1983.
74. Kuban, M. B., *Kinetics of Nucleation and Growth in a Eutectoid Plain Carbon Steel*, M.A.Sc. Thesis, The University of British Columbia, 1983.
75. ASTM A416-93, "Steel Strand, Uncoated Seven-Wire for Prestressed Concrete," *Annual Book of ASTM Standards*, Vol. 01.04, 1994, pp. 218-221.
76. ASTM A421-91, "Uncoated Stress-Relieved Steel Wire for Prestressed Concrete," *Annual Book of ASTM Standards*, Vol. 01.04, 1994, pp. 222-224.
77. AltaSteel Ltd., Edmonton, Alberta, Canada, Private Communications.
78. Mitchell, C., Ed., "Carbon and Alloy Steel," in *Metals Handbook, Desk Edition*, Howard E. Boyer and Timothy L. Gall, Eds., American Society for Metals, 1985, pp. 4.1-94.
79. ASTM E 8M-94a, "Tension Testing of Metallic Materials [Metric]," *Annual Book of ASTM Standards*, Vol. 03.01, 1994, pp. 81-100.
80. ASTM E 399-90, "Plane Strain Fracture Toughness Testing of Metallic Materials," *Annual Book of ASTM Standards*, Vol. 03.01, 1994, pp. 407-437.

81. ASTM G5-78, "Standard Reference Method for Making Potentiostatic and Potentiodynamic Anodic Polarization Measurements," *Annual Book of ASTM Standards*, Part 10, 1980, pp. 816-826.
82. ASTM E 647-93, "Measurement of Fatigue Crack Growth Rates," *Annual Book of ASTM Standards*, Vol. 03.01, 1994, pp. 569-596.
83. ASTM E 140-88, "Standard Hardness Conversion Tables for Metals," *Annual Book of ASTM Standards*, Vol. 03.01, 1994, pp. 267-282.
84. ASTM E 3-80, "Preparation of Metallographic Specimens," *Annual Book of ASTM Standards*, Vol. 03.01, 1994, pp. 11-15.
85. ASTM E 92-82, "Vickers Hardness of Metallic Materials," *Annual Book of ASTM Standards*, Vol. 03.01, 1994, pp. 207-215.
86. ASTM E 384-89, "Microhardness of Materials," *Annual Book of ASTM Standards*, Vol. 03.01, 1994, pp. 385-403.
87. ASTM A 682M-91, "Steel, Strip, High-Carbon, Cold-Rolled, Spring Quality, General Requirements for [Metric]," *Annual Book of ASTM Standards*, Vol. 01.03, 1994, pp. 293-207.
88. ASTM A 684/A 684M-86, "Steel, Strip, High-Carbon, Cold-Rolled," *Annual Book of ASTM Standards*, Vol. 01.03, 1994, pp. 298-301.
89. ASTM A 510M-93, "General Requirements for Wire Rods and Coarse Round Wire, Carbon Steel [Metric]," *Annual Book of ASTM Standards*, Vol. 01.03, 1994, pp. 211-216.
90. Tromans, D., "On Surface Energy and the Hydrogen Embattlement of Iron and Steels," *Acta Metall. Mater.*, Vol. 42, No. 6, 1994, pp. 2043-2049.
91. Elyea, C. S., *A Review of the Literature on Corrosion in Prestressed Concrete*, M. Eng. Report, The University of British Columbia, 1996.
92. Smith, I. F. C., and R. A. Smith, "Fatigue Crack Growth in a Fillet welded Joint," *Eng. Fract. Mech.*, Vol. 18, No. 4, 1983, pp. 861-869.
93. Hartman, A., and J. Schijve, "The Effects of Environment and Load Frequency on the Propagation Law for Macro Fatigue Crack Growth in Aluminum Alloys," *Eng. Fract. Mech.*, Vol. 1, 1970, pp. 615-631.
94. Gan, D., and J. Weertman, "Crack Closure and Crack Propagation Rates in 7050 Aluminum," *Eng. Fract. Mech.*, Vol. 15, No. 1-2, 1981, pp. 87-106.

95. Gan, D., and J. Weertman, "Fatigue Crack Closure After Overloads," *Eng. Fract. Mech.*, Vol. 18, No. 1, 1983, pp. 155-160.
96. Chand, S., and S. B. L. Garg, "Crack Closure Studies Under Constant Amplitude Loading," *Eng. Fract. Mech.*, Vol. 18, No. 2, 1983, pp. 333-347.
97. Forman, R. G., V. E. Kearney and R. M. Engle, "Numerical Analysis of Crack Propagation in Cyclic Loaded Structures," *Trans. ASME, J. Basic Eng.*, Vol D89, No. 3, 1967, pp. 459-464.
98. Zheng, X.-L., "Mechanical Model for Fatigue Crack Propagation in Metals," see ref. 6, pp. 363-395.
99. Zheng, XiuLin, and M. A. Hirt, "Fatigue Crack Propagation in Steels," *Eng. Fract. Mech.*, Vol. 18, No. 5, 1983, pp. 965-973.
100. Zheng, X.-L., "Overload Effects on Fatigue Behavior and Life Prediction of Low Carbon Steels," *Int. J. Fatigue*, Vol. 17, No. 5, 1995, pp. 331-337.
101. Narayan, R., A. Kumar, and K. P. Singh, "The Anodic Polarization and Stress Corrosion Cracking of Eutectoid Steel," *Corr. Sci.*, Vol. 25, No. 6, 1985, pp. 449-460.
102. Cron, C. J., J. H. Payer, and R. W. Staehle, "Dissolution Behavior of Fe-Fe₃C Structures as a Function of pH, Potential, and Anion - An Electron Microscopic Study," *Corrosion J.*, NACE, Vol. 27, No. 1, 1971, 1-25.
103. Pourbiax, M., *Lectures on Electrochemical Corrosion*, 3rd Ed., NACE Int., 1995.
104. Uhlig, H. H., and R. W. Revie, *Corrosion and Corrosion Control, An Introduction to Corrosion Science and Engineering*, 3rd Ed., John Wiley & Sons, 1985.
105. Fontana, M. G., *Corrosion Engineering*, 3rd Ed., McGraw-Hill Inc., 1986.
106. Pourbiax, M., *Atlas of Electrochemical Equilibria*, Pergamon Press, New York, 1966.
107. Tian, Y. L., and W. Kraft, "Kinetics of Pearlite spheroidization," *Metall. Trans. A*, Vol. 18A, No. 8, 1987, pp. 1359-1369.
108. Hahn, G.T., V. Bhargava, and Q. Chen, "The Cyclic Stress-Strain Properties, Hysteresis Loop Shape, and Kinematic Hardening of Two High-Strength Bearing Steels," *Metall. Trans. A*, Vol. 21A, No. 3, 1990, pp. 653-665.

109. Park, Y.J., and I.M. Bernstein, "The Process of Crack Initiation and Effective Grain Size for Cleavage Fracture in Pearlitic Eutectoid Steel," *Metall. Trans. A*, Vol. 10A, No. 11, 1979, pp. 1653-1664.
110. ASTM E 112-88, "Determining Average Grain Size," *Annual Book of ASTM Standards*, Vol. 03.01, 1994, pp. 227-252.
111. Argon, A. S., "Effects of Surfaces on Fatigue Crack Initiation," see ref. 4, pp. 176-182.
112. Shen, D., "Friction and Wear of Eutectoid and Hypoeutectoid Steels," in *Wear of Materials 1985, Intl. Conf. On Wear of Materials, Vancouver, BC, Canada*, K. C. Ludema, Ed., ASME 1985, pp. 194-204.
113. Kakousek, J., D. M. Fegredo, and E. E. Lanfer, "The Wear Resistance and Worn Metallography of Pearlite, Bainite and Tempered Martensite Rail Steel Microstructures of High Hardness," in *Wear of Materials 1985, Intl. Conf. On Wear of Materials, Vancouver, BC, Canada*, K. C. Ludema, Ed., ASME 1985, pp. 212-231.
114. Wang, Y., and T. Lei, "Wear Behavior of Steel 1080 with Different Microstructures During Dry Sliding," *Wear*, Vol. 194, 1996, pp. 44-53.
115. Tyfour, W. R., J. H. Beynon, and A. Kapoor, "The Steady State Wear Behavior of Pearlitic Rail Steel Under Dry Rolling-Sliding Contact Conditions," *Wear*, Vol. 180, 1995, pp. 79-89.
116. McColl, I. R., R. B. Waterhouse, S. J. Harris and M. Tsujikawa, "Lubricated Fretting Wear of a High-Strength Eutectoid Steel Rope Wire," *Wear*, Vol. 185, 1995, pp. 203-212.
117. Cree, A. M., R. G. Faulkner and A. T. Lyne, "Cementite Particle Coarsening During Spheroidization of Bearing Steel SAE 52100," *Mater. Sci & Tech.*, Vol. 11, No. 6, 1995, pp. 566-571.
118. Garbarz, B., and F. B. Pickering, "Effect of Pearlite Morphology on Impact Toughness of Eutectoid Steel Containing Vanadium," *Mater. Sci. & Tech.*, Vol. 4, No. 4, 1988, pp. 328-334.
119. Han, K., T. D. Mottishaw, G. D. W. Smith, D. V. Edmonds and A. G. Stacey, "Effects of Vanadium Additions on Microstructure and Hardness of Hypereutectoid Pearlitic Steels," *Mater. Sci & Eng. A*, Vol. 190, 1995, pp. 207-214.
120. Beynon, J. H., J. E. Garnham and K. J. Sawley, "Rolling Contact Fatigue of Three Pearlitic Rail Steels," *Wear*, Vol. 192, 1996, pp. 94-111.

121. Lesuer, D. R., C. K. Syn and O. D. Sherby, "Fracture Behavior of Spheroidized Hypereutectoid Steels," *Acta Metall. & Mater.*, Vol. 43, No. 10, 1995, pp. 3827-3835.
122. Panasyuk, V. V., and L. V. Ratych, "The Methodology of Estimating Inhibitor Effectiveness in Corrosion Fatigue Crack Propagation," *Corrosion Sci.*, Vol. 37, No. 3, 1995, pp. 391-412.
123. Karlsson, B., and G. Linden. "Plastic Deformation of Eutectoid Steel with Different Cementite Morphologies," *Mater. Sci. & Eng.*, Vol. 17, 1975, pp. 153-164.
124. Richards, C. F., and T. C. Lindley, "The Influence of Stress Intensity and Microstructure on Fatigue Crack Propagation in Ferritic Materials," *Eng. Fract. Mech.*, Vol. 4, 1972, pp. 951-978.
125. Raymond, L., "Evaluation of Hydrogen Embrittlement," see ref. 1, pp. 283-290.
126. Jones, D. A., "A Unified Mechanism of Stress Corrosion and Corrosion Fatigue Cracking," *Metall. Trans. A*, Vol. 16A, No. 6, 1995, pp. 1133-1141.
127. Griffiths, A. J., R. B. Hutchings and A. Turnbull, "Validation of the Role of Bulk Charging of Hydrogen in Corrosion Fatigue Cracking of a Low Alloy Steel," in *Progress in Understanding and Prevention of Corrosion*, J. M. Costa, and A. D. Mercer, Eds., European Corrosion Congress, Vol. 2, Spain, 1993, The Institute of Materials, 1993, pp. 1627-1632.
128. Maier, H. J., W. Popp, and H. Kaesche, "Effects of Hydrogen on Ductile Fracture of a Spheroidized Low Alloy Steel," *Mater. Sci. & Eng. A*, Vol. 191, 1995, pp. 17-26.
129. Rajan, V. B., and J. P. Hirth, "Effects of Hydrogen on Four-Point Bend Test of U-Notched AISI 1090 Steel," *Metall. Trans. A*, Vol. 18, No.2, 1987, pp. 335-340.
130. Shoesmith, D. W., "Effects of Metallurgical Variables on Aqueous Corrosion," see ref. 1, pp. 45-49.
131. Corrosion Status Report (1993), Engineering Dept., Waha Oil Company, Tripoli, Libya, Private communication.
132. Oriani, R. A., "The Diffusion and Trapping of Hydrogen in Steel," *Acta Metall.*, Vol. 18, No. 1, 1970, pp. 147-157.
133. Oriani, R. A., and P. H. Josephic, "Equilibrium Aspects of Hydrogen-Induced-Cracking of Steels," *Acta Metall.*, Vol. 22, No. 9, 1974, pp. 1065-1074.
134. Padkin, A. J., M. F. Brereton, and W. J. Plumbridge, "Fatigue Crack Growth in Two-Phase Alloy," *Metar. Sci. & Tech.*, Vol. 3, No. 3, 1987, pp. 217-223.

135. Hirth, J. P., "Effects of Hydrogen on the Properties of Iron and Steel," *Metall. Trans. A*, Vol. 11A, No. 6, 1980, pp. 861-890.
136. John Wagner, *Cathodic Protection Design I*, Educational Course Manual, NACE International, 1994.
137. Gabriel, B. L., *SEM: A User's Manual for Materials Science*, ASM, 1985.
138. Tromans, D., and R. H. Sun, "Intergranular/Transgranular Fatigue of Copper: Influence of Environment on crack Path and Propagation Rates," *Mater Sci. & Eng.*, In print.
139. McClintock, F. A., and G.R. Irwin, *Fracture Toughness Testing and its Applications*, ASTM STP 381, American Society for testing and Materials, Philadelphia, PA, 1964, pp. 84-113.
140. Shewmon, P. G., *Diffusion in Solids*, McGraw-Hill, New York, 1963, pp. 13-14.